DROPLET MANIPULATION WITH FEEDBACK CONTROL

A THESIS SUBMITTED TO THE GRADUATE DIVISION OF THE UNIVERSITY OF HAWAIʻI AT MĀNOA IN PARTIAL FULFILLMENT OF THE REQUIREMENTS FOR THE DEGREE OF

MASTER OF SCIENCE
IN
MECHANICAL ENGINEERING

DECEMBER 2017

Kyle Yu

Thesis Committee:
Yi Zuo, PhD
John S. Allen, PhD
Weilin Qu, PhD

Acknowledgements

I thank the University of Hawaii, where I conducted research, practiced engineering, and fostered relationships.

I thank Dr. Yi Zuo for participation, assistance, and advice in content presented in this thesis.

I thank Dr. John S. Allen, Dr. Weilin Qu, and Dr. Yi Zuo for participation and evaluation in the thesis committee.

I thank Jerry Yang and Dayne Sasaki for cooperation and assistance, on a professional and personal basis.

I thank friends and family for support during my time at the University of Hawaii.

I acknowledge financial support from NSF under the grant number CBET-1254795.

I am grateful to you all.

Abstract

Droplet manipulation has an important role in a wide range of scientific and industrial applications, such as thin film, soft matter, microfluidics, biophysical simulations, interfacial reactions, and interfacial rheology. We developed a feedback-controlled closed-loop axisymmetric drop shape analysis (CL-ADSA) to manipulate millimeter-sized droplets, based on the experimental methodology constrained drop surfactometer (CDS). With CL-ADSA, we extended the CDS from a surface tension measurement tool to a sophisticated droplet manipulation instrument. We demonstrated the usefulness of this methodology in three practical applications, control of droplet volume by automatically compensating natural evaporation, precise control of surface area variations for high-fidelity biophysical simulations of natural pulmonary surfactant, and steady control of surface pressure for *in situ* Langmuir-Blodgett transfer from droplets. Furthermore, we developed an arbitrary waveform generator for controlled oscillation of a droplet/bubble. We demonstrated this methodology in three ways. First, we demonstrated arbitrary waveform generation by controlling the volume and surface area of a water droplet to sine, triangle, square, and sawtooth waveforms. Second, we evaluated the accuracy of the arbitrary waveform generation through a coefficient of determination analysis. Third, we apply arbitrary waveform generation to study the interfacial dilational rheology of adsorbed surfactant films. Our studies suggest the feedback control system developed in this thesis hold great promise for advancing droplet manipulation in a variety of material and surface science applications, such as thin-film fabrication, self-assembly, and biophysical study of pulmonary surfactants.

Table of Contents

List of Figures

List of Tables

List of Abbreviations

V	Volume
A	Surface Area
γ	Surface Tension
π	Surface Pressure
θ	Contact Angle
κ	Compressibility
ADSA	Axisymmetric Drop Shape Analysis
AFM	Atomic Force Microscopy
CDS	Constrained Drop Surfactometer
PD	Pendant Drop
SD	Sessile Drop
PB	Pendant Bubble
SB	Sessile Bubble
G	Gravitational Acceleration
E_0	Limiting Elasticity
Er	Elastic Modulus
Ei	Viscous Modulus
$\|E\|$	Total Modulus
FPS	Frames Per Second
SD	Standard Deviation
FEM	Finite Element Method
RAM	Random-Access Memory
.DAT	Data File Format
PI	Proportional Integral
PD	Proportional Derivative
PID	Proportional Integral Derivative
C_{12}DMPO	Dodecyldimethylphosphine Oxide
DPPC	Dipalmitoyl Phosphatidylcholine
DOPC	1,2-Dioleoyl-Sn-Glycero-3-Phosphocholine
PL	Phospholipids

Chapter 1. Introduction

1.1 Introduction

Surface science is the study of physical and chemical properties between interfacial interfaces, for example, air and water, oil and water, or metal and water. Surface science is an interdisciplinary study and has many scientific and industrial applications, namely adhesives, coatings, pharmaceuticals, sprays, and semiconductors. A fluid surface can be broadly described by its surface tension, a cohesive phenomenon of the surface of fluids defined as the force per unit length. This phenomenon is observed in a liquid's ability to maintain droplets; a droplet with a higher surface tension will maintain a more spherical profile and vice versa.

Surface tension and other characterizing properties can be measured using a computational technique known as Axisymmetric Drop Shape Analysis (ADSA). In equilibrium, a fluid droplet is shaped by gravity and its own surface tension.[1] By inversely solving the Laplacian equation which the drop shape can be modeled upon, it is possible to calculate a surface tension from an image.[1] ADSA, developed by Del Rio et al, computerizes this process to seconds on a modern computer.[1] The experimental apparatus for ADSA based experiments are surface tensiometers. For the purpose of this thesis, the tensiometer is known as the Constrained Drop Surfactometer (CDS).[2] Through ADSA and the CDS, the Laboratory of Biocolloids and Biointerfaces at the University of Hawaii study a number of surface phenomena, namely interactions involving self-assembled monolayers, pulmonary surfactants, and toxicology of nanomaterials.

1.2 Surfaces and Surface Tension

A critical concept in the study surface science is surface tension, a cohesive phenomenon of the surface of fluids. In general, there are five types of interfaces, liquid-gas, liquid-liquid, liquid-solid, solid-gas, and solid-solid.

Distance between liquid molecules is significantly less than distance in gas molecules, henceforth, gas molecules produce significantly less attraction. At a liquid-gas interface, a molecule is more attracted more by liquid than gas. Thus, the interface will minimize its surface area, resulting in a phenomenon known as surface tension. For liquid-gas interfaces, this phenomenon is commonly observed in a liquid's ability to maintain droplets; a droplet with a high surface tension will maintain a more spherical profile, vice versa, a droplet with a low surface tension a less spherical profile. Surface tension, represented by the Greek symbol Gamma "γ", is defined as force per unit length, often as mN/m.

Surface tension can be altered by surfactants. The term surfactant is an abbreviation for surface active agent. Surfactants are amphipathic molecules containing both hydrophilic and hydrophobic components. At water-air interfaces, the hydrophilic head sits in water, while the hydrophobic tails points into air. This amphipathic structure gives surfactant molecules a relocation preference for the interface. Surfactants form a single layer of molecules at the interface, called a monolayer, which is shortened for "monomolecular film".[3] Intermolecular forces between surfactant molecules and liquid molecules are weaker than intermolecular forces between liquid molecules alike. Thus, surfactant molecules at water-air interfaces decreases surface tension.

There are many types of surfactants, namely laundry detergents, foaming agents, and lung surfactant. In mammalian lungs, a part of required work is from expanding the alveoli against surface tension; and lung surfactant reduces this work by reducing the surface tension around the alveoli. Lung surfactant, by weight, is approximately 90% lipids and 10% proteins. The lipids consist of phospholipids (PLs, 90–95 wt.%) with a small amount of neutral lipids (5–10 wt.%).

Surface tension can be measured using a number of techniques known as drop shape analysis. In equilibrium, a fluid droplet or bubble is shaped by gravity and its own surface tension; moreover, this phenomenon can be modeled by the Laplace equation of capillarity[1]. As such, by inversely solving the Laplace equation, it is possible to calculate the surface tension from an image of a drop or bubble.[1]

1.3 Constrained Drop Surfactometer

The Constrained Drop Surfactometer (CDS) is a surface tensiometer developed by the Laboratory of Biocolloids and Biointerfaces at the University of Hawaii. The CDS consists of an image acquisition component, an environmental control component, and a liquid flow component. **Figure 1.1** demonstrates a schematic of the CDS. **Figure 1.2** demonstrates a photo of the CDS.

The image acquisition component consists of a camera (Model PLB-771U, PixeLink), a droplet, a light source (Model NT62-817, Edmund Optics). When these three are aligned, a high contrast silhouette of the droplet reaches the camera sensor. The camera acquires images

between 0 to 30 frames per second (FPS). The backlight and diffusing lens provides parallel backlight for illumination.

The liquid flow component manipulates fluid flow to the droplet for formation and deformation. This component consists of a motor driver (1002C, Gastight, Hamilton), a servomotor (Model LTA-HS, Newport), a syringe (1002C, Gastight, Hamilton), and a droplet, which form a motor-piston-syringe. Motor displacement manipulates the liquid flow, and hence the droplet volume.

The environmental control component maintains temperature and humidity for the droplet. This component consists of a thermoelectric plate (Model CP-61, TE Technology) and a machined environmental chamber. The thermoelectric plate provides heating or cooling to the environmental chamber. The environmental chamber has glass windows to pass light. Upon simulating physiological conditions, air in the environmental chamber is maintained at 37 ºC and is saturated with water vapor.

Over the course of an experiment, the environmental conditions are maintained, the volume of a droplet is manipulated by the liquid flow component; in parallel, a series of droplet images may be captured. After an experiment, droplet images are sent to the computer for ADSA calculations.

1.4 Axisymmetric Drop Shape Analysis

Drop shape analysis can determine surface tensions between liquid-gas or liquid-liquid interfaces of sessile drops (SD), sessile bubbles (SB), pendant drops (PD), and pendant bubbles (PB). The shape of droplet is determined by gravitational forces, which deforms the droplet (i.e.,

elongating PD and PB and flattening SD and SB), and surface tension forces, which rounds droplet. The force between gravity and surface tension can be modeled by the Laplace equation of capillarity:[1]

$$\gamma\left(\frac{1}{R_1}+\frac{1}{R_2}\right)=\Delta\rho g z+\frac{2\gamma}{R_0} \qquad \text{(Eq. 1.1)}$$

where R_1 and R_2 are the two principal radii of curvature, $\Delta\rho$ is the density difference between the interface, z is the height of the droplet normal from the reference plane, R_0 is the radii at the apex of the droplet. Therefore, given γ and other parameters above, the shape of droplet may be determined, vice versa, it is possible to determine the surface tension from a given drop shape profile.

It is timely to solve the surface tension from the droplet profile analytically. Among numerical solutions, Axisymmetric Drop Shape Analysis-Profile (ADSA-P), developed by Neumann et al, is amongst the most powerful due to its efficiency, accuracy, and flexibility.[1, 4] ADSA-P computerizes the numerical solution and reduces timely manual calculation to seconds on a modern computer.

Axisymmetric Drop Shape Analysis (ADSA) performs calculations on imported droplet images. Firstly, the image is processed through an edge detection routine. This generates a number of pixels, typically around 1000, along the shape of the droplet, to produce a 2D array of the edge pixel coordinates, known as the experimental profile. Moreover, the unit of the experimental profile are pixel coordinates and these coordinates needs to be distance coordinates. This scale factor is constant for every experimental setup. Given physical constraints such as density and gravity, a series of ideal Laplacian curve profiles, known as theoretical profiles, are

generated through the Bashforth-Adams equation (Eq. 1.1), where axisymmetric interfaces can be expressed as a function of the arc length *s*:

$$\frac{d\theta}{ds} = \frac{2}{R_0} + \frac{\Delta\rho g}{\gamma} z - \frac{\sin\theta}{x} \quad \text{(Eq. 1.2)}$$

$$\frac{dx}{ds} = \cos\theta \quad \text{(Eq. 1.3)}$$

$$\frac{dz}{ds} = \sin\theta \quad \text{(Eq. 1.4)}$$

$$\frac{dV}{ds} = \pi x^2 \sin\theta \quad \text{(Eq. 1.5)}$$

$$\frac{dA}{ds} = 2\pi x \quad \text{(Eq. 1.6)}$$

$$x(0) = 0, z(0) = 0, \theta(0) = 0, V(0) = 0, A(0) = 0 \quad \text{(Eq. 1.7)}$$

where θ is the tangential angle, *x* is the radius, and *z* is the height, R_0 is the curvature at the origin, $\Delta\rho g / \gamma$ is the capillary constant, A is surface area, and V is droplet volume[1]. Third, a numerical fitting scheme fits and selects the theoretical drop profiles to the experimental profile, thereby outputting corresponding properties of the drop/bubble, such as droplet volume, surface area, and surface tension. The theoretical profile that best fits the experimental profile is selected. The theoretical profile is exported along with its droplet volume, surface area, surface tension, and contact angle.

The Graphical User Interface (GUI) of ADSA was developed with Microsoft Visual Studios as a Multiple Document Interface program, allowing for multiple child windows to reside under one main window. A powerful function of ADSA GUI is the analysis of a run of images, which are droplet images with identical physical constraints. This allowed the automatic calculation of an entire set of images from an experiment. However, this function is confined to the precondition that the images must be prepared prior to analysis.

1.4.1 Edge Detection

Image files of the droplet/bubble are acquired through a machine vision camera (Model PLB-771U, PixeLink). A parallel backlight illuminates the droplet/bubble. Image files are stored as 8-bit grayscale uncompressed .tiff files, with a max resolution of 1280×1024. Generally, Canny edge detection is used for edge detection in droplet/bubble.[5] First, a Gaussian blur is applied to reduce noise. Second, differentiation in x and y directions produce gradient vectors. Third, non-maximum suppression suppresses a gradient upon a larger gradient neighbor, in x and y directions, removing a number of pixels. Fourth, hysteresis thresholding selects gradient vectors above a high threshold as an edge pixel, and removes gradient vectors below a low threshold. Remaining gradients are selected upon the condition of neighboring a previously selected pixel.

1.4.2 Numerical Fitting

The numerical scheme, introduced by Rotenberge et al.[4], is used to find the theoretical curve that best fit the experimental profile. The strategy is to minimize an objective function E, the sum of weighted squared normal distances, e_i, between all coordinates of experimental profile and theoretical profiles:

$$e_i = \frac{1}{2} d_i^2 = \frac{1}{2}[(x_i - X_i)^2 + (z_i - Z_i)^2] \quad \text{(Eq. 1.8)}$$

$$\min E(a) = \sum_{i=1}^{N} w_i e_i\,(a) \quad \text{(Eq. 1.9)}$$

where w_i is the weighting factor of the i^{th} point, (X_i, Z_i) are experimental coordinates and (x_i, z_i) are the corresponding Laplacian coordinates closest to (X_i, Z_i), a is a set of optimizing parameters $a = [x_0 \;\; z_0 \;\; b \;\; c]$, where (x_0, z_0) is the coordinate of the apex, and b is the curvature of the apex, and c is the capillary constant $\Delta\rho g / \gamma$. This becomes a multidimensional nonlinear

least-square problem, which requires an iterative Newton-Raphson or Levenberg-Marquardt optimization procedure.[1] Once the minimum is found, the optimization parameters determine the theoretical profile that best fit the experimental profile, and surface tension and other properties are computed.

1.5 Control Systems Overview

Control systems commands and regulates systems through control loops. In continuous control, feedback loops can automatically control a process or operation. Feedback control systems compares the controlled variable's value or status with the desired value, and thereby apply a control signal to change the controlled variable's value or status to the same value as the desired value.

Traditionally, ADSA and CDS based experiments are limited to the measurement of droplet, while control of droplet remains mostly a manual procedure. Automatic control of droplet volume, surface area, and surface tension reduces significant manual work and can open up new areas of study entirely. A controller system is to be integrated on the existing system. Here, the plant, which is the process and the actuator, is the constrained Drop Surfactometer (CDS). The measurement, which is the required feedback, is the Axisymmetric Drop Shape Analysis (ADSA). Upon the completion of feedback control, arbitrary waveform generation is to be explored.

Prerequisites for feedback control, control design specifications, are control model are prepared prior to the implementation of feedback control. Common control algorithms are Bang–bang control, Proportional control, Proportional Integral (PI) control, Proportional Derivative

(PD) control, and Proportional Integral Derivative (PID) control, and fuzzy control. The implementation is compared and discussed. Adaptive control, which adapts to the control system, will also be discussed. Feedback control applications including but not limited to evaporation compensation, physiological simulations, and surface rheology will be explored and discussed.

1.6 Thesis Outline

This thesis communicates the development process of feedback control for droplet manipulation. The feedback control will be based on the existing plant, the constrained Drop Surfactometer (CDS), and the existing measurement, Axisymmetric Drop Shape Analysis (ADSA). The development of feedback control system is through software and hardware interfacing, with C based computer languages.

This thesis is suitable for readers with a basic understanding of physics, chemistry, engineering, and information technology. Other technical content will be explained where applicable. This thesis states the background of drop shape analysis, image processing, physiological simulations, and surface thermodynamics, but does not elaborate upon these. This thesis demonstrates feedback control for four drop/bubble configurations: sessile drop, sessile bubble, pendant drop, and pendant bubble, but will focus on the sessile drop. This thesis discusses the conception and validation of the implemented control system, but does not discuss the details of C and C++ implementation. The computer interfaces with experimental hardware through serial and parallel communication. There exist device drivers for various experimental hardware, however, significant infrastructure was developed to readily communicate with the

aforementioned hardware, and this thesis does not discuss the structure, algorithm, and parallelization of the implemented infrastructure.

Chapter 2 discusses feedback control. This includes a prerequisite for feedback control which is real-time measurement, control limitations, control equations and models, and applications and discussion. Chapter 3 discusses the extension of feedback control, arbitrary waveform generation. This includes control limitations, generated waveforms, and applications and discussion. Chapter 4 summarizes this thesis work and contributions thereof.

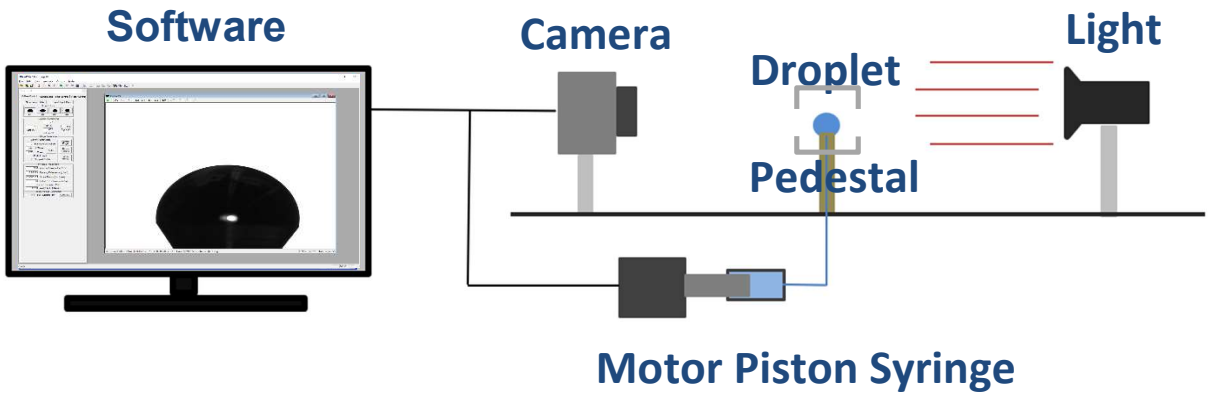

Figure 1.1 The Constrained Drop Surfactometer (CDS). A droplet is formed on a pedestal. The pedestal is connected to the motor-piston-syringe, pushing/pulling fluid, thereby resulting in formation and deformation. The light source on the left projects images of the droplet into the camera on the right. Images are then sent to ADSA for analysis. These three components are controlled independently by a computer.

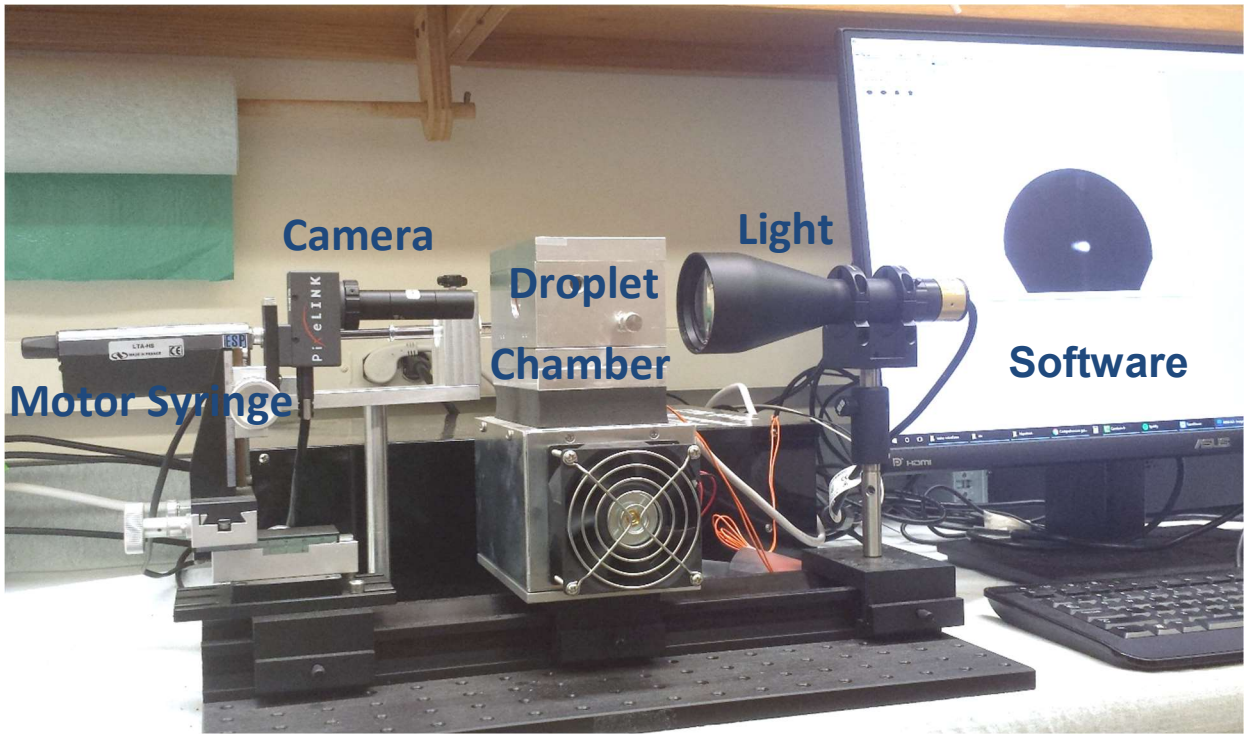

Figure 1.2 Photo of the experimental setup CDS. A droplet is formed on a pedestal. The CDS is composed of three parts, the camera and light for visualization, the motor-piston-syringe and pedestal for actuation, software for analysis. The droplet and pedestal is placed in an environmental chamber above a thermoelectric plate.

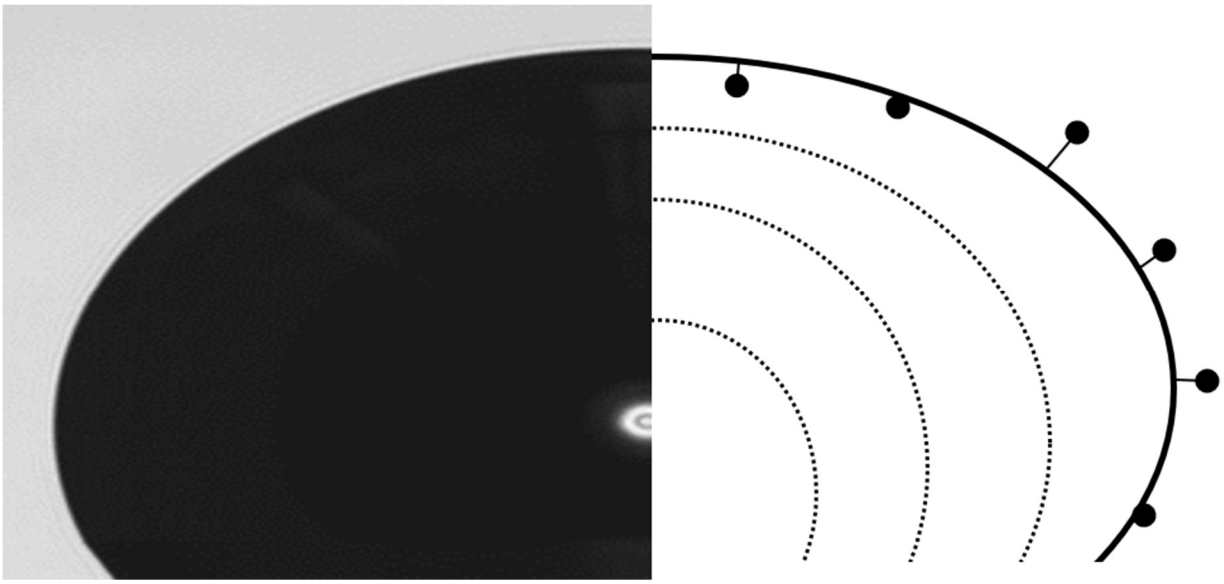

Figure 1.3 Procedure of ADSA on a sessile drop. First, ADSA opens an image file, this is shown on the left half of the image. Second, through edge detection, the edge or profile coordinates is extracted (large black dots). Third, a series of theoretical profiles (dashed black lines) are generated to match the detected profile (solid black line). Through the matched profile, surface properties, such as drop(s)/bubble volume, surface area, surface tension are obtained.

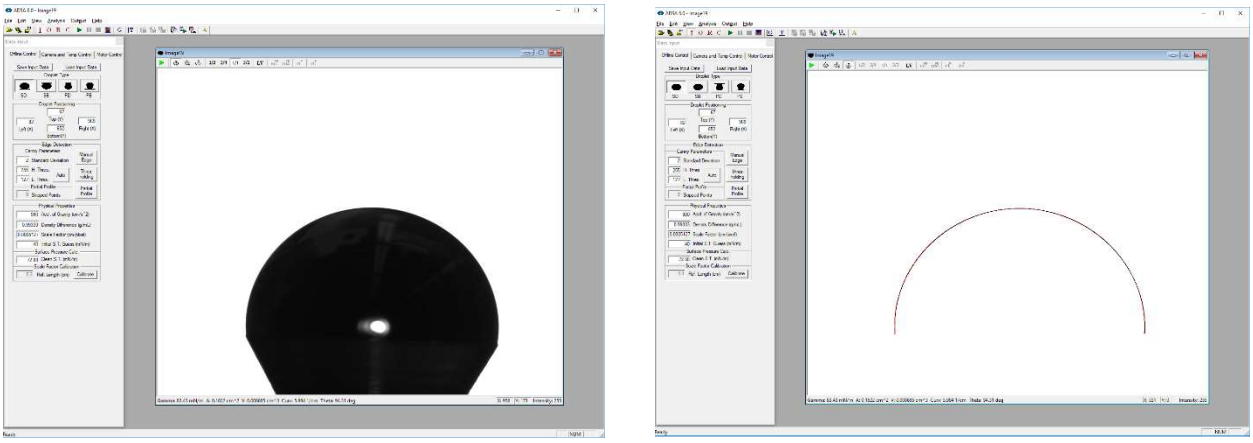

Figure 1.4 Sample screenshots of the ADSA GUI interface. The left screenshot shows the ADSA GUI with an original raw experimental image of a sessile bubble while the right screenshot shows the ADSA GUI with a processed edge profile of a sessile droplets.

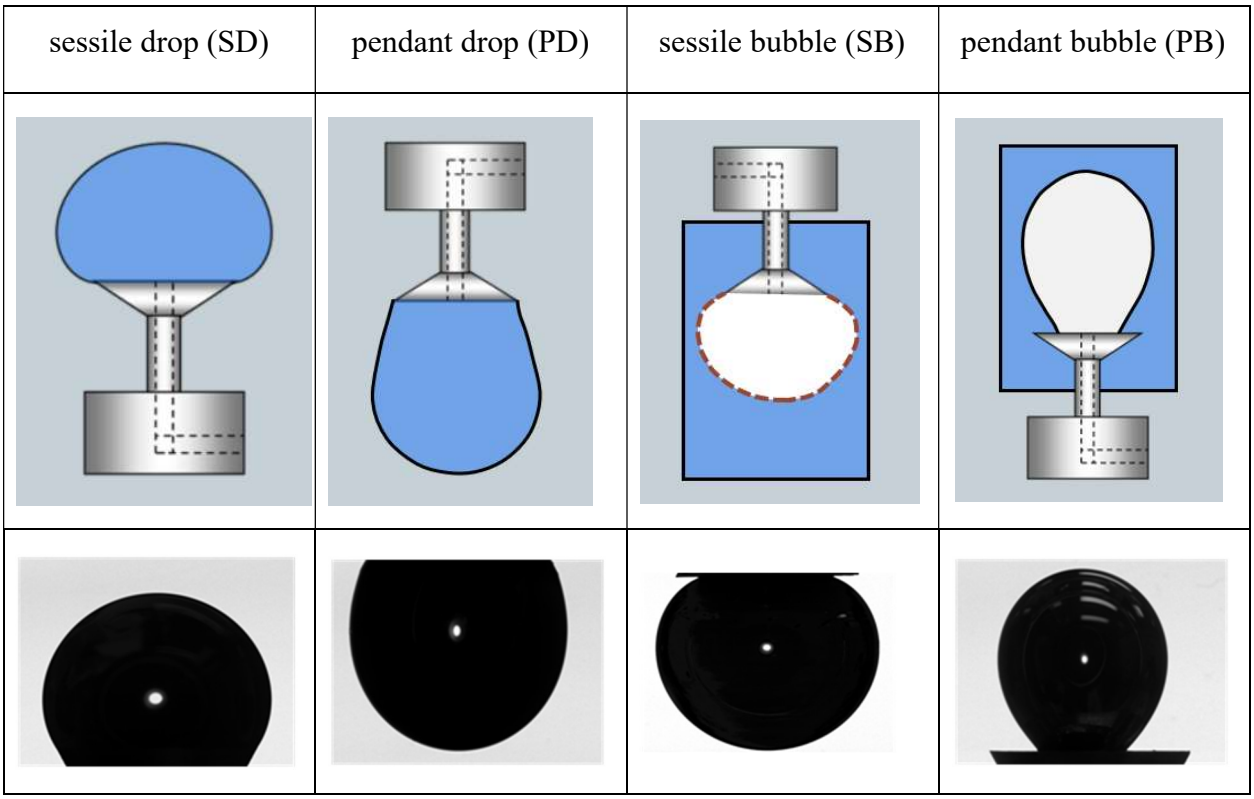

Figure 1.5 Four studied axisymmetric droplet/bubble configurations. These are the sessile drop (SD), pendant drop (PD), sessile bubble (SB), and pendant bubble (PB). The diagram is placed on top and the actual experimental images of formamide droplet/bubble are placed on the bottom. The coordinate system is defined through the polarities of the density difference ($\Delta\rho$) and the height of a point along the drop profile (z). $\Delta\rho$ is the density difference between the fluid inside the discrete droplet and the fluid outside the droplet. $\Delta\rho$ of PD and SD is positive and $\Delta\rho$ of SB and PB is negative. z coordinate is defined as positive for SD and PB and negative for SB and PD.

Chapter 2. Feedback Control Development

2.1 Introduction

Effective manipulation of liquid droplets plays an important role in a wide range of scientific and industrial applications, such as synthesis of thin-film materials,[6] control of interfacial reactions,[7] study of surface rheology,[8] and operation of digital microfluidics.[9] In these applications, droplets serve as a miniaturized platform that provides a number of unique advantages over traditional interfacial models such as the classical Langmuir trough.[10] First, the small volume of droplets facilitates study of scarce or expensive samples, such as biological or clinical fluids. Second, compared to bulk systems, droplets possess a much larger surface-area-to-volume ratio that makes droplets an ideal soft platform for studying surface reaction and interfacial assembly. Third, due to system miniaturization, it is feasible to ensure a rigorous environmental control, such as temperature and experimental atmosphere, with the droplet system, thus allowing for environmental studies across the droplet surfaces.[11]

Compared to the control of a flat surface as in the classical Langmuir trough, effective control and manipulation of a single droplet is not a trivial task. In general, the profile of a free-standing droplet is determined by the balance of gravitational and surface tension forces as predicted by the Bond number, $Bo = \frac{\Delta\rho g R^2}{\gamma}$, where $\Delta\rho$ is the density difference across the drop surface, g is the gravitational acceleration, R is the characteristic radius of the droplet, and γ is the surface tension. Droplets with very small Bond numbers, such as micron-sized droplets, are generally considered as spherical beads.[12] The key parameter for manipulating such droplets is their volume; while the surface area can be calculated by a spherical approximation and the

surface tension is routinely assumed to be a constant.[13] A number of techniques have been developed to manipulate the volume of micron-sized droplets.[12-14]

However, when the Bond number is sufficiently large, *e.g.,* for millimeter-sized droplets and/or at the presence of surfactants, the drop profile can be significantly deformed by gravity to assume a Laplacian shape.[10, 15] In these cases, the surface area of the droplet cannot be correlated with its volume using a simple spherical approximation. Meanwhile, the surface tension usually varies with the surface area at the presence of surfactants. Hence, all droplet properties, including its volume, surface area, and surface tension, need to be individually controlled for effective droplet manipulation. Nevertheless, in most applications, one can only control the drop volume using a high-precision syringe pump. Neither surface area nor surface tension of the droplet can be directly controlled with current techniques. Cabrerizo-Vilchez and coworkers have developed a fuzzy-logic algorithm to control the surface pressure or surface area of a pendant drop.[15] In spite of a suitable control method, the fuzzy-logic algorithm requires the definition of input and output fuzzy sets for every control process, which is not a trivial task.

In this chapter, we developed a novel feedback control method for manipulating millimeter-sized droplet based on axisymmetric drop shape analysis (ADSA). ADSA is a computer-based surface tension measurement methodology first developed by Neumann and coworkers.[1, 4] ADSA determines surface tension, surface area, and volume of a droplet by numerically fitting the experimental drop profile to theoretical profiles integrated with the numerical Laplace equation of capillarity. We have developed a high-speed ADSA algorithm capable of real-time analysis of droplet properties, including its volume, surface area, and surface tension. By coupling real-time ADSA with a proportional-integral-derivative (PID) controlled

motorized syringe, we have developed the first closed-loop ADSA that is capable of precisely controlling the volume, surface area, and surface tension of a millimeter-sized droplet.

2.2 Real-Time Analysis Development

ADSA is designed for analysis on existing droplet image files such that the images must be prepared in advance. This results in a timely and inefficient procedure to study surface phenomena and an obstacle for feedback control.

This procedure requires usage of multiple software. During an experiment, the operator first must prepare the droplet on the CDS for study. The droplet formation and deformation is through liquid flow from a motor-piston-syringe assembly. The motor in controlled by a **Newport SMC100 Motor Driver Software**. The operator next must capture images of the droplet. The camera is controlled by a **PixeLink camera driver**. After the experiment, the images are loaded into the **ADSA software** for analysis and output. After analysis, the resulting data file (.DAT) is plotted and visualized **OriginLab Origin Software.** This procedure is necessary for even the most basic experiments, and requires repetition for every successive experiment, leading to a timely process. **Figure 2.1** demonstrates this procedure.

Real time ADSA analysis can automate much of this procedure, and is a necessity for feedback control. There are several key operations to real time analysis. Firstly, ADSA must communicate with the camera firmware to retrieve images directly from the camera. Second, ADSA shall automatically perform analysis on retrieved images. Third, in parallel with the first two operations, ADSA must plot the analysis data for the operator to visualize. All of this shall

be automated and shall be performed simultaneously with the experiment. **Figure 2.2** demonstrates this procedure.

This automation increases efficiency significantly. For example, during dynamic cycling experiments, experiments involving cycles of rapid droplet size increase and decrease, several hours can be saved over the course of a day.

2.2.1 Camera Integration

There are two objectives for the camera communication. Upon selection, ADSA shall generates a live preview video from the camera. Upon additional selection, ADSA shall repeatedly retrieve image frames for analysis.

ADSA must first be able to communicate with the camera firmware. PixeLink provides C and C++ header files for additional software development. The ADSA visual studios project must integrate the camera class and function calls. An additional execution thread is necessary such that the preview video, analysis, and GUI all execute independently. In a multithreaded program, multiple sequence of programmed instructions executes concurrently, in this case, preventing video lag and freezing of the GUI. Also, another child frame class, a window residing in the main window of the ADSA program, was added and integrate in the visual studios project.

For real time analysis, ADSA retrieves an image frame as a 2D unsigned integer byte array (`uint8_t`), and dynamically allocates this structure to the random-access memory (RAM). The image array is then called directly by the ADSA class initiating image processing and analysis. In addition, an option to write the retrieved frame onto the hard disk was developed. This procedure increases speed by one frame write; testing showed this increased computational

time by roughly 150ms. An option to write the image file as TIFF or compressed to JPG was developed.

2.2.2 Plotting Integration

The plotting and visualization interface shall encompass basic plotting functions of Originlab origin. ADSA shall feed analyzed results into a plot window and shall plot the droplet's frame number, time, volume, surface area, surface tension, and contact angle.

In addition to camera development, an additional execution thread and an additional child frame class is necessary. The plot class shall receive results data from the analysis class, and shall manipulate data dynamically, with an option to export as a .DAT file.

The plot window involved existing plotting libraries or development anew. After elementary research and analysis on popular plotting libraries, it was concluded that libraries that mustered the most potential was MathGL, GNU Plot, PLplot, Microsoft Chart Control, and MiniPlot. These libraries share a same purpose, but are mutually exclusive in implementation. It is highly ineffective to implement multiple options, given time resources.

It is ideal to select a single implementation. Two decision matrices were employed, allowing for weighted and systematic identification and analysis of the local design criteria. Two decision matrices are constructed, one for benefit and one for time cost. The option with the highest ratio of benefit vs time shall be selected. The design factor's relative significance was based on its alignment to plotting specification and needs. **Table 1** and **Table 2** demonstrates this.

The implementation with the highest benefit vs cost ratio was to build anew. Building anew takes longer to start as foundation classes are missing, but no further integration and maintenance was required. Also, gaining experience with a math library is timely. Other libraries, notably MathGL and PLplot are more mathematical in design, which is not needed for this scope. Another factor that made building anew the most promising alternative was that it offered greater flexibility; the interface can later be adjusted with great ease. Moreover, **Figure 2.3** demonstrates a screenshot of the completed real-time analysis.

2.3 Closed-loop Feedback Control System

Six control algorithms of Bang–bang control, Proportional control, Proportional Integral (PI) control, Proportional Derivative (PD) control, and Proportional Integral Derivative (PID) control, and fuzzy control shall be implemented and integrated over real time analysis ADSA and the CDS. These six algorithms have strength and limitations with respect to each other, and each have suitable applications.

Open loop control is a control which does not feedback from ADSA. A predetermined command displacement is sent to the motor. Droplet control with the Newport SMC100 Motor Driver Software is open loop control. However, this type of control is processes no feedback control and is highly susceptible to system disturbances.

Bang–bang control sets the motor to two states of on and off. This controller actuates the motor when the droplet is outside a predefined command range, and switches the motor off when the droplet reaches within the command range. This is a continuous control process requiring

feedback control. Bang–bang control is straightforward and requires minimal processing. However, the motor speed is predefined thereby resulting in longer transient times.

Proportional control actuates the motor continuously to a value proportional to the error, which is the difference between the command state of the droplet and the measured state. This controller requires sampling from feedback control, and able to improve the transient time. However, proportional control may be prone to steady state errors, which occur when the current state of the droplet is close to the command state, and the proportional motor actuation is unable to propagate the droplet further to the command state.

Proportional-integral (PI) control extends proportional control by incorporating an integral component, which is a value proportional to the time integral of previous errors. In general, integral control is able to reach the command state faster and is able to eliminate steady state errors. However, due to the cumulative nature of integral control, it amplifies transient state errors such as overshoot, and requires marginally greater processing power.

Proportional-derivative (PD) control extends proportional control by incorporating a derivative component, which is a value proportional to the rate of change of the error. In general, derivative control stabilizes the error from oscillation by attenuating transient state errors such as overshoot. Furthermore, derivative control is very sensitive to erroneous samples from ADSA, which may occur from analysis on a bad image. Derivative control requires marginally greater processing power.

Proportional-integral-derivative (PID) control encompasses all three components of proportional integral and derivative control. It possesses the strengths of limitations of all three. It is noted that gains, the constant multiplier for each of P, I, and D control, needs to be

administrated. Inappropriately large gains may result in an oscillatory or unstable system. Such a system will not result in permanent equipment damage as the hardware is designed with limiters. However, an unstable system will require the manual reset of the entire CDS system if left unattended due to contamination and disconnection.

Fuzzy control is based on fuzzy logic. To simplify, bang-bang control is a control of discrete 0 and 1, and fuzzy control is a control continuous 0 and 1. For instance, when the error is large, the motor turns fast; when the error is small, the motor is slow; when the error is negligent, the motor stops; this is 3 states. In this case, the input is a fuzzy set and the output is a fuzzy set. The inputs can be the proportional error, the integral error, and the derivative error. The output can be the volume injected. In this case, the error fuzzy sets can translate (or fuzzifies) the actual error to a level. This volume fuzzy set can translate (or fuzzifies) the current volume to a level. Then the controller uses a "rule set" to find the output, the volume injected, fuzzy level. Lastly, the volume injected fuzzy set translates (or defuzzifies) this level to an actual volume to inject.

2.3.1 Closed Loop Control Limitations

Upon the completion of real time analysis, a control diagram for the proposed Single-Input-Single-Output (SISO) system is shown in **Figure 2.4**. There are several limitations in the controller design. Firstly, the ADSA's analysis or sampling rate greatly limits the controller. Secondly, there exists system disturbances in the plant; in an ideal system, the injected volume is proportional to the motor displacement. Lastly, there are transient state constraints such that the controller is to be applied to experiments involving Dipalmitoyl phosphatidylcholine (DPPC) monolayers and lung surfactants.

2.3.1.1 Sampling Time

In general, lower sampling rates requires less processing power, resulting in longer transient times or lower accuracy. Higher sampling rates requires more processing power, resulting in shorter transient times or better accuracy.[16] Due to the ADSA's numerical computations, its sampling rate is orders of magnitude slower than simpler measuring systems, such as displacement controllers or temperature controllers. Optimized by Yu et al, ADSA can sample at a max rate of 10 Hz.[17] Also, device latency shall be considered. After ADSA measures and reports the surface area of a droplet, the droplet may have propagated to another state. There is a latency of approximately 200ms.

2.3.1.2 System Disturbances

The CDS uses a motor-piston-syringe for droplet formation and deformation, shown in **Figure 1.1**. Motor displacement pushes the piston into the syringe, thereby injecting fluid into the droplet and vice versa. In an ideal system, motor voltage and on-time is proportional to motor displacement, which in turn is proportional to the volume of fluid injected. However, this was observed not to be the case. There are system disturbances arising from the physical system of the motor-piston-syringe which cannot be modeled due to its spontaneous action. For example, the static friction between the walls of the piston and the syringe, or fluid pressure disparities between push action and pull action in droplet expansion and compression, respectively.

2.3.1.3 Transient State Constraints

ADSA measures droplet in experiments involving biological fluids, namely lung surfactants. Lung surfactant facilitates the surface tension of alveolar cells. During pulmonary respiration simulation, the droplet is compressed and expanded at a physiologically relevant frequency of 15-20 periods per minute.[2] The transient state, of alveolar cells in pulmonary

respiration, is a near linear rise or fall. The controller shall not produce significant sharp rises or overshoots, and shall produce oscillation of 15-20 periods per minute at relevant amplitudes.

2.3.2 Open-Loop Plant (or Process) Model

The plant model, consisting of the high precision servomotor and the piston-syringe, can be approximated as a first order system. The input to this model can be modeled as a unit step. In the Laplace domain, the input can be modeled as:

$$\mathrm{f}(\mathrm{t}) = \begin{cases} 0, \mathrm{t} < 0 \\ \mathrm{k}, \mathrm{t} \geq 0 \end{cases} \rightarrow F(\mathrm{s}) = \frac{\mathrm{k}}{\mathrm{s}}, s \geq 0 \qquad \text{(Eq. 2.1)}$$

where k is the input value. The high precision servomotor contains a feedback loop such that its displacement response is nearly linear. The servomotor contains threaded shaft which acts as a helix gear to push a syringe piston. In the open-loop system where the inner servomotor control loop is closed, displacing below the rated velocity of 5 mm/s, there is a nearly linear transience and the absence of overshoot. The displacement error is in the order of micrometers. Hence, the relationship between the servomotor input and the piston displacement can be modeled as an integrator. In the Laplace domain, this first order system can be modeled as:

$$\mathrm{f}(\mathrm{t}) = \mathrm{k_m} * \mathrm{t} \rightarrow F(\mathrm{s}) = \frac{\mathrm{k_m}}{\mathrm{s}} \qquad \text{(Eq. 2.2)}$$

where $\mathrm{k_m}$ is the speed of the motor. There exist un-modeled nonlinearities observed to be non-dominant and are negligible. It was observed that this open loop model closely simulates the open-loop droplet control.

2.3.3 Closed Loop Model

Given the continuous-time feedback configuration can be represented in the figure below, the closed-loop transfer function in the Laplace domain may be simplified as:

$$\frac{\mathrm{y}}{\mathrm{r}} = \frac{\mathrm{C(s)*P(s)}}{\mathrm{C(s)*P(s)+1}} \quad \text{(Eq. 2.3)}$$

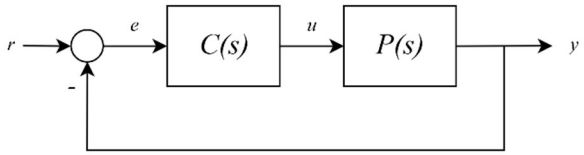

where C(s) is the controller, P(s) is the plant, r is the reference input, e is the error, u is the system input, and y is the output.

For closed-loop control, it is determined the system is controllable and observable. To achieve versatility, simplicity, and robustness, a PID controller was selected. During the transient state of the control, the digital controller of ADSA calculates the "error", i.e., the difference between the command state and the actual state, and thereafter actuates the motor and droplet to a value that is proportional to the current, the time integral, and the rate of change of the error. The continuous-time and discrete domain transfer function for PID control is:

$$u(t) = k_p * e(t) + \int_0^t k_i * e(\tau)\, d\tau + k_d \frac{de(t)}{dt} \rightarrow \quad \text{(Eq. 2.4)}$$

$$\mathrm{U(s)} = k_p * \mathrm{E(s)} + \left(\frac{k_i}{s}\right) * \mathrm{E(s)} + k_d * s * \mathrm{E(s)} \rightarrow \quad \text{(Eq. 2.5)}$$

$$\mathrm{U(z)} = k_p * \mathrm{E(z)} + \left(\frac{k_i}{1-\frac{1}{z}}\right) * \mathrm{E(z)} + k_d * (1 - \tfrac{1}{z}) * \mathrm{E(z)} \quad \text{(Eq. 2.6)}$$

where k_p is the proportional gain, k_i is the integral gain, k_d is the derivative gain, e is the value of the error, and u is the value of the command signal. Given the equation above for the transfer function for a closed-loop feedback system, the transfer function for the control system can henceforth be simplified as:

$$\frac{y}{r} = \left(\frac{k_m * k_s * (k_d * s^2 + k_p * s + k_i)}{(k_m * k_s * k_d + 1) * s^2 + k_m * k_s * k_p * s + k_m * k_s * k_i}\right) \quad \text{(Eq. 2.7)}$$

where k_m is the motor speed constant, k_s is the piston-syringe constant, r is the reference input and y is the output. To design for the k_p, k_i, and k_d parameters, and the constant k_m, the closed-loop zeros and poles are placed to meet the design specifications arrived based on the experimental setup. This is followed by appropriate tunings and simulations.

2.3.4 Discrete Time Model

In the digital feedback system, sensors, actuators, and ADSA incurs a latency in the system. The sensors, actuators, and ADSA, upon optimizations, can measure droplet properties at a rate of 10 Hz. Hence, controller must use data from the past, which incurs a sampling delay. Furthermore, this sampling delay may induce oscillations and instability. In the Laplace domain, a continuous delay can be modeled as,

$$f(t - \tau) \rightarrow e^{(-s*\tau)} * F(s) \quad \text{(Eq. 2.8)}$$

where τ is the continuous-time delay. For a digital controller, the delay can be modeled in the discretized z-domain. Through emulation, the controller can be designed for continuous-time domain specifications, and subsequently discretized to the z-domain, followed by appropriate tunings and simulations. A representation is shown in the figure below. Through bilinear transformation, the discrete-time controller can be approximately modeled as,

$$C(s)|\ s = \frac{2}{T}\frac{z-1}{z+1} \rightarrow D[z] \qquad \text{(Eq. 2.9)}$$

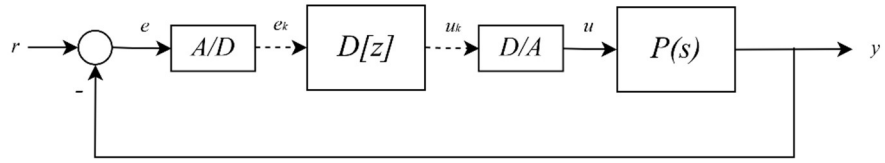

where T is the sampling time, C(s) is the continuous-time controller, and D[z] is the emulated discrete-time controller. P(s) is the continuous time plant, r is the reference input, e is the error, e_k is the discrete error, u_k is the discrete system input, u is the system input, and y is the output. A/D is an analog to digital converter and D/A is a digital to analog converter. The dashed lines represent discrete signals.

In addition, the continuous-time model of the system P(s) can be approximated and discretized to a model in the discrete-time domain. Subsequently, the discrete digital controller may be directly designed to meet continuous-time domain specifications. A representation is shown in the figure below. The closed-loop poles and zeros, based on continuous-time specifications, are selected in the s-domain and mapped to the z-domain, followed by appropriate tunings and simulations. The closed-loop transfer function of the model may be simplified as:

$$\frac{y_k}{r_k} = \frac{D[z]*G[z]}{D[z]*G[z]+1} \qquad \text{(Eq. 2.10)}$$

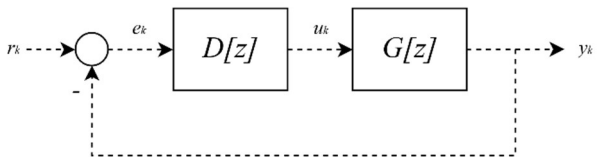

where D[z] is the digital discrete controller, G[z] is the discretized plant, r_k is the discrete reference input, e_k is the discrete error, u_k is the discrete system input, and y_k is the discrete output. The dashed lines represent discrete signals.

2.3.5 Model Simulations

The transient state of the droplet can be controlled by administering different controller gains. The integral component may be useful in overcoming small steady-state errors and increase the robustness of the controller. The derivative component may be useful in attenuating the transient state oscillations. Parallel with simulations, a series of loop tuning experiments were conducted to optimize the settling time, overshoot, and transient response. The settling time, the time where steady state is achieved, is observed to be 2-4 seconds. The overshoot, where the actual output exceeds the desired output prior to steady state, is largely non-existent. Furthermore, the transient response is largely that of linear one. The symmetry of PID control is susceptible to the differences between the dynamics of droplet formation and compression. However, observed through experiment, these phenomena are non-dominant.

To design for the sampling delay via emulation, the controller gain parameters are first determined in continuous-time specifications. Once the controller gains are determined, the controller may be discretized with Eq. 2.9, followed by appropriate loop tuning and simulation. To design for the sampling delay via direct design, the system model is discretized into the z-domain. For example, an integrator can be discretized as:

$$y[(k+1)T] = y(k+1) + T * u(k*T) \quad \text{(Eq. 2.11)}$$

$$y(s) = \frac{1}{s}u(s) \Rightarrow Y[z] = \frac{T}{z-1}U[z] \quad \text{(Eq. 2.12)}$$

Where T is the sample delay in seconds.

The closed loop poles, based on continuous-time specifications, are selected in the s-domain and mapped to the z-domain. Arriving at the desired transfer function, follow by appropriate loop tuning and simulation. To guarantee stability, in the s-domain, the closed loop pole exists in left right-hand plane, in the z-domain, the closed loop pole exists in open unit disk.

The resulting simplified model is modelled and simulated in MATLAB Simulink. **Figure 2.5** demonstrates this. Determined experimentally, the stiction of the interface between the piston and the glass of the syringe was inserted. Furthermore, to examine the robustness of the system, addictive and multiplicative noise was inserted. Moreover, the noise from the sensor of the industrial camera and the noise from the computational analysis of ADSA, are not significant, and are modeled as a Gaussian noise with a low variance in MATLAB Simulink.

2.4 Materials and Methods

2.4.1 Materials

The water used in this study was Milli-Q ultrapure water (Millipore, Billerica, MA). It has a resistivity greater than 18 MΩ·cm at room temperature. The pulmonary surfactant used in this study was Infasurf (Calfactant), which was a gift from ONY Inc. (Amherst, MA). Infasurf was purified from whole-lung bronchopulmonary lavage of newborn calves. Through an extraction process, Infasurf retained all of the hydrophobic components of bovine endogenous surfactant including phospholipids, cholesterol, and most hydrophobic surfactant proteins (SP-B and SP-C).[18-19] Infasurf has a total phospholipid concentration of 35 mg/mL and is stored frozen

in sterilized vials. On the day of experiments, it was thawed and diluted to a phospholipid concentration of 5 mg/mL with a saline buffer of 0.9% NaCl, 1.5 mM $CaCl_2$, and 2.5 mM HEPES, adjusted to pH 7.0. Dipalmitoyl phosphatidylcholine (DPPC) was purchased from Avanti Polar Lipids (Alabaster, AL) and used without further purification. DPPC was dissolved in chloroform to form a 1 mg/mL stock solution.

For biophysical simulations of pulmonary surfactant, detailed experimental protocols can be found elsewhere.[11, 20] Briefly, a droplet (~ 10 μL) of 5 mg/mL Infasurf was dispensed onto the CDS drop pedestal, maintained within an environmental chamber that controls the physiologically relevant conditions, *i.e.*, 37 °C and 100% relative humidity. After drop formation, the surface tension quickly decreased to an equilibrium value of approximately 22-25 mN/m,[21] indicating formation of an adsorbed surfactant film at the air-water interface. Once the equilibrium was established, the adsorbed surfactant film was compressed and expanded at a rate of 5 seconds per cycle by withdrawing and injecting water into the droplet using the motorized syringe. The compression ratio was controlled to be less than 20% of the initial surface area to simulate normal tidal breathing. A minimum of five continuous compression−expansion cycles were studied for each droplet. It was observed that the cycles became repeatable after the first cycle.

For the study of self-assembled phospholipid monolayers at room temperature, a tiny amount of 1 mg/mL DPPC stock solution was spread using a microsyringe onto a droplet of pure water of which the surface tension was recorded as γ_0.[22] The droplet was then slowly expanded to increase surface tension (γ) until the corresponding surface pressure ($\pi = \gamma_0 - \gamma$) was reduced to ~1 mN/m. The droplet was left undisturbed for an additional 1 min to allow evaporation of the solvent. The spread DPPC monolayer was subsequently compressed at a quasi-equilibrium rate

of 0.06 cm^2/min, corresponding to 0.17% initial surface area per second. Langmuir-Blodgett (LB) transfer from the droplet was implemented by lifting a small piece of freshly peeled mica sheet at a speed of 1 mm/min, under controlled surface pressure. Topographical images were obtained using an Innova AFM (Bruker, Santa Barbara, CA). Samples were scanned in air in contact mode with a silicon nitride cantilever of a spring constant of 0.12 N/m and a tip radius of 2 nm. Lateral structures were analyzed using Nanoscope Analysis (version 1.5).

2.4.2 Methods

Since its development, ADSA has been routinely used as an open-loop system for determining properties of drop/bubble (*i.e.*, surface tension, surface area, and volume) by analyzing its images.[1, 4] Here, we further developed ADSA into a closed-loop system in which droplet properties determined in real-time are used as feedback control parameters to actuate the droplet towards desired targets. A diagram of the feedback control loop is illustrated in **Figure 3.1**. A digital PID controller was directly integrated into ADSA. In the closed-loop feedback control system, ADSA continuously calculates the error, *i.e.*, the difference between the target values and the current values, and thereafter automatically actuates the droplet towards the target values using a motorized syringe (consisting of a high-precision servomotor and a piston-syringe system) with PID control. The transient state of the droplet can be controlled by administering proper PID gains. The feedback control system was modeled in the time domain, the Laplace domain (in which the time domain representation is transformed into a frequency domain representation), and the Z-domain (in which the digital discrete time representation is transformed into another frequency domain representation).[23]

There are several advantages and novelties of the closed-loop ADSA in comparison with previous droplet manipulation methods. 1. To the best of our knowledge, the closed-loop ADSA is the first method capable of controlling the volume, surface area, or surface tension of millimeter-sized single droplets. Previous methods can only control drop volume. However, knowledge about the surface area and surface tension of the droplet can be only obtained by post-experimental analysis of drop images acquired during the experiments. Hence, control parameters such as area compression ratios and targeting surface tension values cannot be set *a priori*. In comparison, the closed-loop ADSA analyzes the deformed drop shape in real time and hence eliminates the need of image acquisition for post-analysis. Consequently, the closed-loop ADSA allows live manipulation of a droplet. 2. Since the closed-loop ADSA manipulates the droplet by directly controlling properties of the target droplet, it is independent of the physical methods of fluid actuation, regardless of the fluid is driven by a motorized syringe or by a piezoelectric transducer. 3. Being a free-standing method, although the closed-loop ADSA is demonstrated here with a sessile drop setup, it can be readily applied to manipulate other drop or bubble shapes, such as pendant drop or captive bubble, provided that ADSA is applicable.

2.5 Results and Discussion

2.5.1 Control of Volume

In this study, we demonstrate direct control of drop volume with the closed-loop ADSA. **Figure 2.7** shows the manipulation of a 60 μL water droplet on the CDS platform at room temperature. The volume of the droplet (panel c) was decreased and increased stepwise with a step of every 10 μL, followed by steps of every 20 μL and 40 μL, respectively. Images of this

droplet at different volumes are shown as inserts in panel a. It is clear that the volume change was controlled to be largely linear with respect to time and without significant overshoot once reaching the target values within a 1% tolerance. Response to the control was fast. Regardless of the magnitude of volume change, the target values were reached within 1 second. It can be also seen that during the manipulation of drop volume, the surface tension (panel a) of pure water fluctuates at 71±2 mN/m, in agreement with the literature value.[22] The deviation mostly takes place upon reducing the drop volume. This is most likely due to traces of impurities (that cause surface tension decrease) and/or intrinsic artifacts of drop shape analysis at small volumes (that cause surface tension increase).[24-25]

We further demonstrate the usefulness of the ADSA-based volume control by solving a real-world problem, *i.e.*, droplet evaporation. Evaporation is an inevitable problem of any droplet-based apparatus in which the drop volume decreases with time due to evaporation at a rate affected by the surface area of the droplet, diffusivity of the liquid, and the environmental conditions.[25] For instance, protein adsorption may take several hours to complete, during which evaporation may cause significant artifact by contracting the air-water interface of the droplet.[26-27] Another example in which the compensation of droplet evaporation is essential is the study of gas adsorption at the air-water interface.[28] Volume loss is especially problematic for small droplets as the highly curved drop surface increases the chemical potential of evaporation.[29]

The rate of evaporation of the droplet has been investigated extensively. Birdi and Winter concluded evaporation rate remains constant when the contact line is pinned.[30] Shanahan and Bourges concluded there are several distinct stages of evaporation.[31] Hu and Larson employ an analytical theory and a computational method using the finite element method (FEM).[32] It can be

said that the evaporation rate of a sessile droplet is constant in time, given smaller contact angles. Hu and Larson present a simple approximate expression:

$$y(s) = \pi \, R \, D \, (1 - H) c_v (0.27\theta^2 + 1.30) \qquad \text{(Eq. 2.13)}$$

where R is the contact-line radius, D is the diffusivity, c_v saturated water vapor concentration, H is the relative humidity, and θ is the contact angle. Moreover, given the presence surfactants, the rate of evaporation lessens significantly.

Here, we demonstrate that the ADSA-based volume control maintains a constant drop volume over a prolonged time period by automatically compensating the effect of evaporation. As shown in **Figure 2.8**, without control, the volume of a 60 μL water droplet shrinks by 30% over 30

due to natural evaporation. In comparison, with the ADSA-based control, the drop volume was maintained at constant over the same time period with volume variations less than 0.5%.

It should be noted that it is also possible to control the volume of a droplet using a high-precision syringe pump, if only the linear displacement of the syringe pump is properly calibrated and converted to variations in the drop volume. However, our ADSA-based method represents a novel feedback control system that drives the motor to directly control the drop volume with the value determined in real-time by ADSA. Hence our method is more accurate, faster, and does not require calibration. The entire process is automatic without the need of any human intervention.

2.5.2 Control of Surface Area

Compared to the control of drop volume, the control of surface area and surface tension of the droplet is exceedingly complicated due to the nonlinearity of these two properties. To demonstrate the nonlinearity of surface area and surface tension with respect to the drop volume, we have conducted a comparative experiment of shrinking three droplets of the same initial volume. These are a pure water droplet, a DPPC-covered water droplet, and an Infasurf droplet. **Figure 2.9** shows the surface area (panel a) and surface tension (panel b) of these three droplets as a function of the reducing volume. It is clear that only the surface area of the pure water droplet is nearly linearly correlated with the drop volume. Nonlinearity in surface area exists for both DPPC-covered and Infasurf droplets, due to drop deformation upon reducing volume. Surface tensions of all three droplets are nonlinearly correlated with the drop volume, in which the surface tension of pure water remains unchanged while reducing volume, and the surface tensions of DPPC-covered and Infasurf droplets decrease quickly to near-zero value upon reducing volume (*i.e.*, the compression of lipid monolayer at the air-water interface).

Nonlinearity of the surface area and surface tension renders the control of these two droplet properties using a regular syringe pump impossible. However, being a feedback control system, our closed-loop ADSA can readily control the surface area or surface tension of the droplet without additional difficulties compared to the control of drop volume. In this study, we demonstrate the direct control of droplet surface area with closed-loop ADSA. We first demonstrate the ADSA-based area control with a similar experiment using water droplets as shown in **Figure 2.10**.

We further demonstrate the usefulness of the ADSA-based area control for solving a research problem, *i.e.*, *in vitro* biophysical simulations of pulmonary surfactant (PS). PS is a phospholipid-protein mixture that is synthesized by alveolar type II epithelial cells. The primary biophysical function of pulmonary surfactant is to reduce the alveolar surface tension, thus contributing to the elastic recoil of the lungs and increasing the pulmonary compliance.[18] A key requirement of *in vitro* biophysical simulations of PS is to mimic the intra-alveolar environment of the lungs. This requires not only rigorous control of experimental conditions to physiological relevance, such as the core body temperature of 37 ºC and 100% relative humidity, but also high-fidelity simulation of respiratory cycles during normal tidal breathing, such as the respiratory rate (*e.g.*, 5 seconds per cycle) and the control of surface area variations to be less than 20% per cycle.[33] Numerous studies have demonstrated that variations in alveolar surface area during respiration are small.[33-35] Surface area of the lungs does not change more than 30% during a deep breath between 40 and 100% total lung capacity (TLC). During normal tidal breathing between 40 and 50% TLC, the area variation is less than 10%.[33-35] All this physiological evidence suggests that natural PS films must have a very low compressibility contributing to lung recoil.[36] However, direct control of surface area during droplet oscillation was not possible in previous *in vitro* simulations.

Figure 2.11 demonstrates the advantages of closed-loop ADSA in biophysical simulations of a natural PS, Infasurf, under physiologically relevant conditions. It can be seen that with surface area control, the adsorbed surfactant film was compressed precisely by 15% area reduction (mimicking exhalation), and subsequently expanded back to its original area (mimicking inhalation). A minimum surface tension of ~2 mN/m was reached with the 15% compression, indicating a low film compressibility of approximately 0.5 $(mN/m)^{-1}$. The

compression and expansion curves coincide closely with each other without showing a significant hysteresis, which represents an ideal biophysical simulation of the respiratory cycle of natural PS.

In contrast, without surface area control, the actual compression ratio of surfactant films cannot be set *prior to* the dynamic cycling experiments. Consequently, the surfactant films are commonly overcompressed or undercompressed, thus failing to mimic the physiological conditions of respiration. As the example shown in Figure 2.11, the surfactant film without area control was compressed by 22% area reduction. It is found that as soon as the area was reduced beyond 15%, the surface tension did not decrease anymore. Rather, the compression curve leveled off at the minimum surface tension, indicating extensive film collapse. Collapse of the alveolar surfactant film is uncommon in mammalian lungs under normal conditions.[37] Hence, this extra area compression is considered to be "overcompression" that is an artifact introduced by the *in vitro* biophysical simulation.[38] Because of this overcompression, the compression-expansion cycle shows a significant hysteresis loop. The area enclosed in the hysteresis loop indicates the amount of mechanical energy loss per respiratory cycle, which is again an artifact for *in vitro* biophysical simulation of natural PS.[39]

2.5.3 Control of Surface Tension and Surface Pressure

To demonstrate the control of surface tension/pressure, we used the CDS as a miniaturized Langmuir balance to study the compression isotherm of a self-assembled DPPC monolayer at room temperature. **Figure 2.12** shows the surface pressure of the DPPC monolayer as functions of the relative surface area (π-A curve) and the compression time (π-t curve), respectively. It can be seen that the π-A curve is consistent with well-characterized DPPC

compression isotherms reported in literature.[18, 40-41] At large surface area and low surface pressure, the DPPC monolayer is in a fluid-like liquid-expended (LE) phase, while the surface pressure only increases slowly with area reduction. After passing a phase transition plateau at about 8.5 mN/m, the DPPC monolayer is transformed into a solid-like tilted-condensed (TC) phase at which the surface pressure increases rapidly with compression, indicating a very low film compressibility for the TC phase DPPC monolayer.[42]

As demonstrated by the π-t curve shown in Figure 2.12, with the ADSA-based surface tension/pressure control, we were able to compress the DPPC monolayer to a target surface pressure (*i.e.*, 8.5, 20, 30, 40, 50, and 60 mN/m) and maintain it over a 100 s period. It can be seen that when the controlled pressure reaches 30 mN/m, a small overshoot appears due to hysteresis incurred by stiction of the piston-syringe system. However, the controller is able to correct the overshoot and bring the steady-state surface pressure to the target value. The steady-state error of this control is <1.5%.

The precise control of surface tension/pressure over time allows extended investigation of self-assembled monolayers and thin-films fabricated at the droplet surface. One such application is *in situ* Langmuir-Blodgett (LB) transfer from the droplet surface. To date, LB transfer of films from the air-water interface to a solid substrate under controlled surface pressure is primarily implemented with a Langmuir trough.[42] After LB transfer, the film can be studied in detail by various microscopic and spectroscopic techniques for characterizing its lateral structure and molecular organization.[18, 39, 43] Here, taking advantage of the ADSA-based surface tension/pressure control, we have implemented the first *in situ* LB transfer of DPPC monolayer from the droplet surface. During the LB transfer, ADSA analysis was restricted to partial drop profiles that were not disturbed by the substrate passing the air-water interface. The insert in

Figure 2.12 shows an AFM topographic image of the DPPC monolayer transferred within the phase transition plateau region, *i.e.*, 8.5 mN/m. The AFM image shows clearly coexistence of the LE phase and the signature kidney-shaped TC domains well-documented in literature.[18, 44]

2.6 Conclusion

To demonstrate the feasibility and advantages of this droplet manipulation method, we have engaged it in three applications of importance in various surface science studies. In the first application, we maintained the volume of a water droplet over a prolonged time period by automatically compensating natural evaporation. In the second application, we demonstrated the feasibility of controlling the surface area of an oscillating droplet for *in vitro* biophysical simulations of natural pulmonary surfactant. By precisely controlling surface area variations during dynamic droplet oscillation, our method allows high-fidelity *in vitro* biophysical simulations of respiratory mechanics. In the third application, we demonstrated the effective control of surface pressure during compression of a self-assembled phospholipid monolayer. By controlling surface pressure over time, we implemented the first *in situ* Langmuir-Blodgett (LB) transfer from a monolayer-covered droplet. All these applications have demonstrated that closed-loop ADSA is highly practical in automating droplet manipulation in a variety of material and surface science applications, such as thin-film fabrication, self-assembly, and biophysical study of pulmonary surfactant.

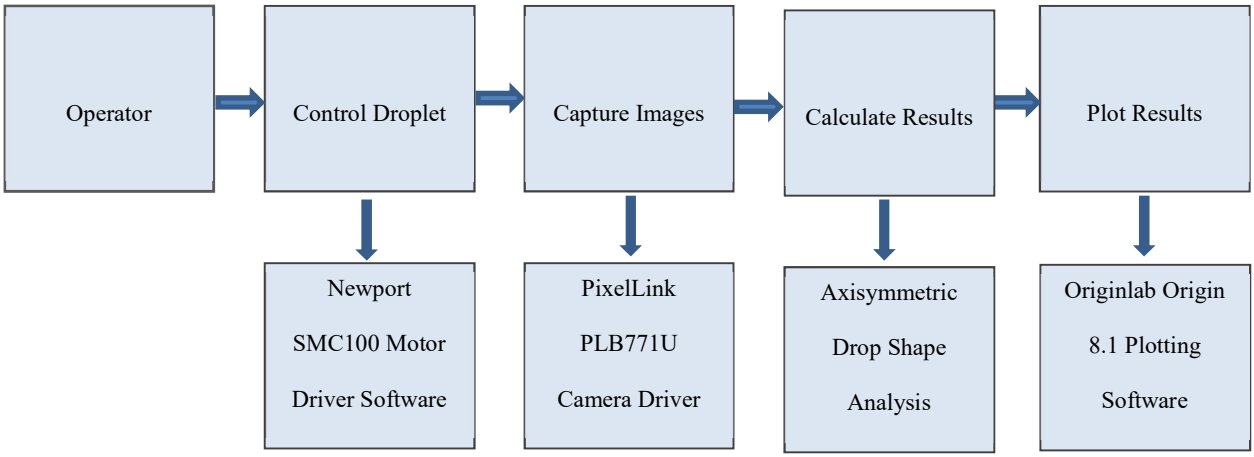

Figure 2.1 Original methodology of the experimental apparatus known as the CDS. First, the experiment takes place which revolves the manual control of the droplet; second, manual image acquisition takes place; third, images are manually fed into the Axisymmetric Drop Shape Analysis GUI for analysis and results; fourth, results are visualized through a plotting software. These steps are on top and the corresponding software are placed below.

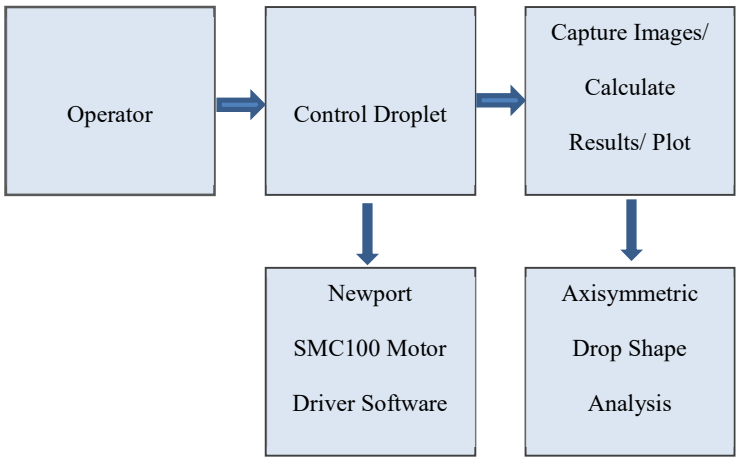

Figure 2.2 Methodology of the CDS, after real-time analysis integration. Real-time ADSA integrates the analysis process. First, the experiment takes place which revolves the manual control of the droplet; second, the Axisymmetric Drop Shape Analysis GUI captures, analyzes, and visualizes and results.

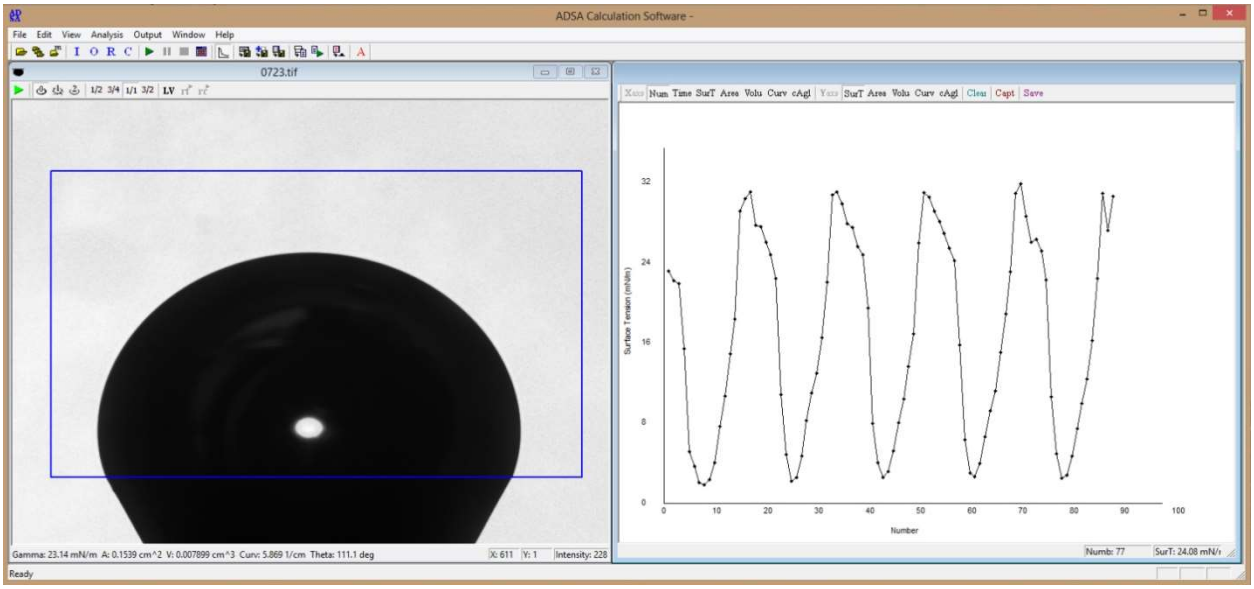

Figure 2.3 Sample screenshot of the ADSA GUI interface after real-time analysis integration. Note the left child class shows the real-time camera preview, and the right child shows the scatter-line plot for surface tension during an experiment involving droplet oscillation. There are several execution threads operating in parallel to facilitate this.

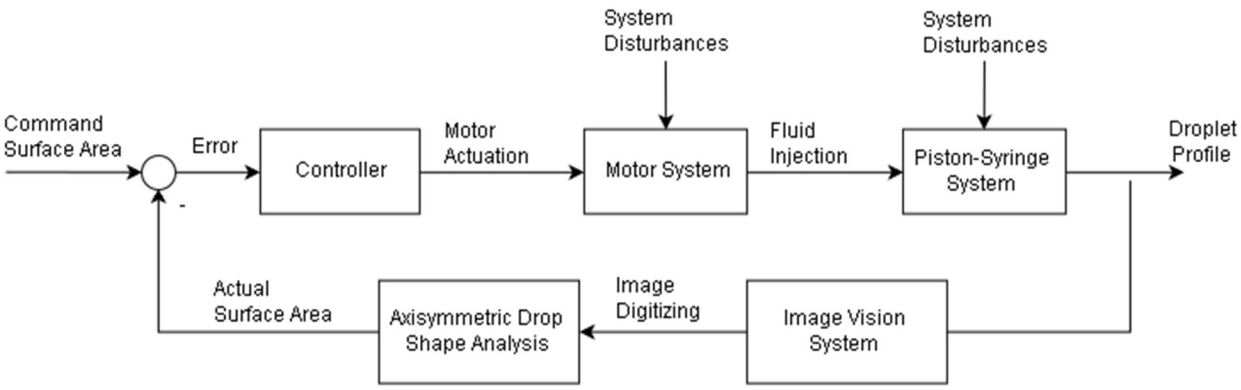

Figure 2.4 Proposed control system for ADSA and CDS based experiments. A command is set to the controller which actuates the motor to inject fluid for droplet based experiments. The droplet is captured by an image vision system which is sent to ADSA for analysis. Note the system disturbances incurring from the motor system and piston syringe system. Note the feedback component of this control diagram.

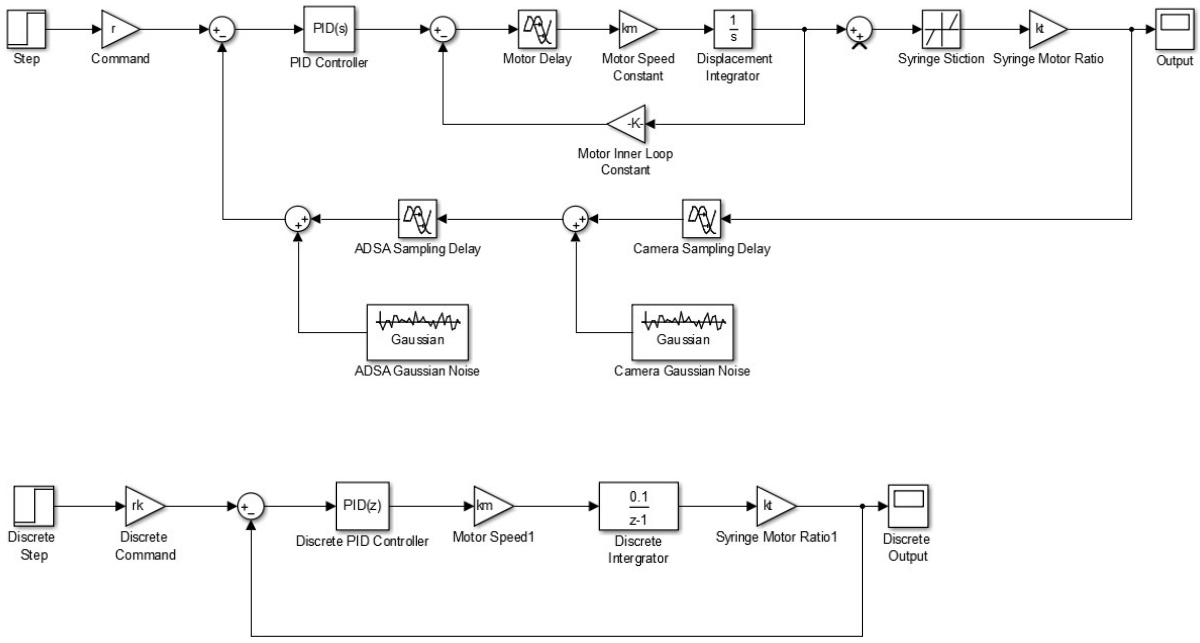

Figure 2.5 Simulation of feedback control system through MATLAB Simulink. Determined experimentally, the stiction of the interface between the piston and the glass of the syringe was inserted. Furthermore, to examine the robustness of the system, addictive and multiplicative noise was inserted. Moreover, the noise from the sensor of the industrial camera and the noise from the computational analysis of ADSA, are not significant, and are modeled as a Gaussian noise with a low variance. Some discrete domain simulation is included at the bottom.

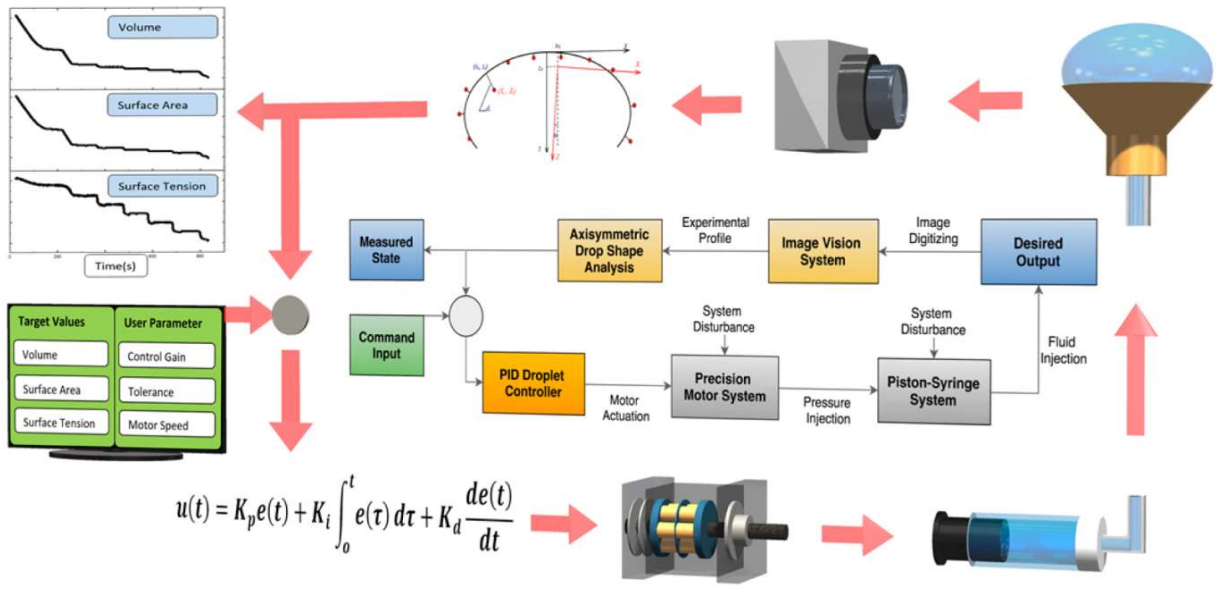

Figure 2.6 The axisymmetric drop shape analysis (ADSA) feedback control system, integrated into the constrained drop surfactometer (CDS). In the CDS, a liquid droplet is "constrained" on a 3-5 mm carefully machined pedestal with a knife-sharp edge. The droplet is continuously monitored by ADSA in real-time. Properties of the droplet, including its volume, surface area, and surface tension, are controlled with the closed-loop ADSA. An integrated PID controller continuously calculates the error, *i.e.*, the difference between the target values and the current values, and converts the error into a command signal with proper PID gains. The PID controller is modeled by $u(t) = k_p e(t) + \int_0^t k_i e(\tau) d\tau + k_d \frac{de(t)}{dt}$, where k_p is the proportional gain, k_i is the integral gain, k_d is the derivative gain, $e(t)$ is the value of the error, and $u(t)$ is the value of the command signal. The resultant command signal controls a motorized syringe, consisting of a high-precision servomotor and a piston-syringe system, to actuate the droplet towards the target values.

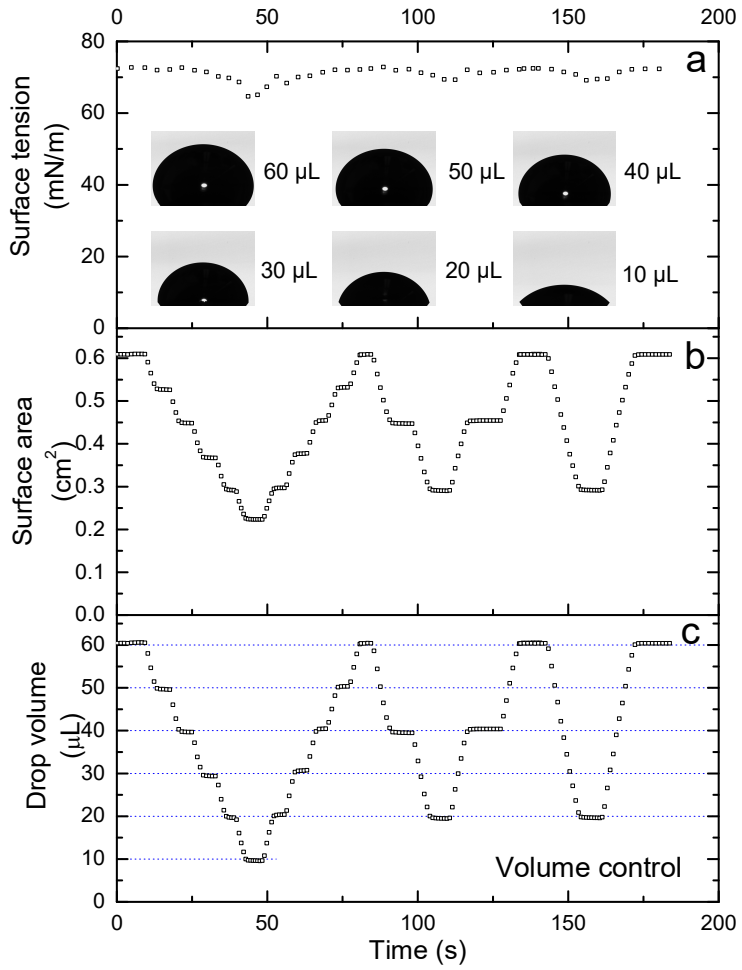

Figure 2.7 Demonstration of the closed-loop ADSA for controlling drop volume. The volume of a 60 μL water droplet (panel c) was decreased and increased stepwise with a step of every 10 μL, followed by steps of every 20 μL and 40 μL, respectively. Images of this droplet at different volumes are shown as inserts in panel a. It is clear that the change of volume was controlled to be largely linear without significant overshoot once reaching the target values within a 1% tolerance. During manipulation of drop volume, the surface tension (panel a) of pure water is largely unchanged, and the surface area (panel b) of the water droplet also varies largely linearly with respect to time.

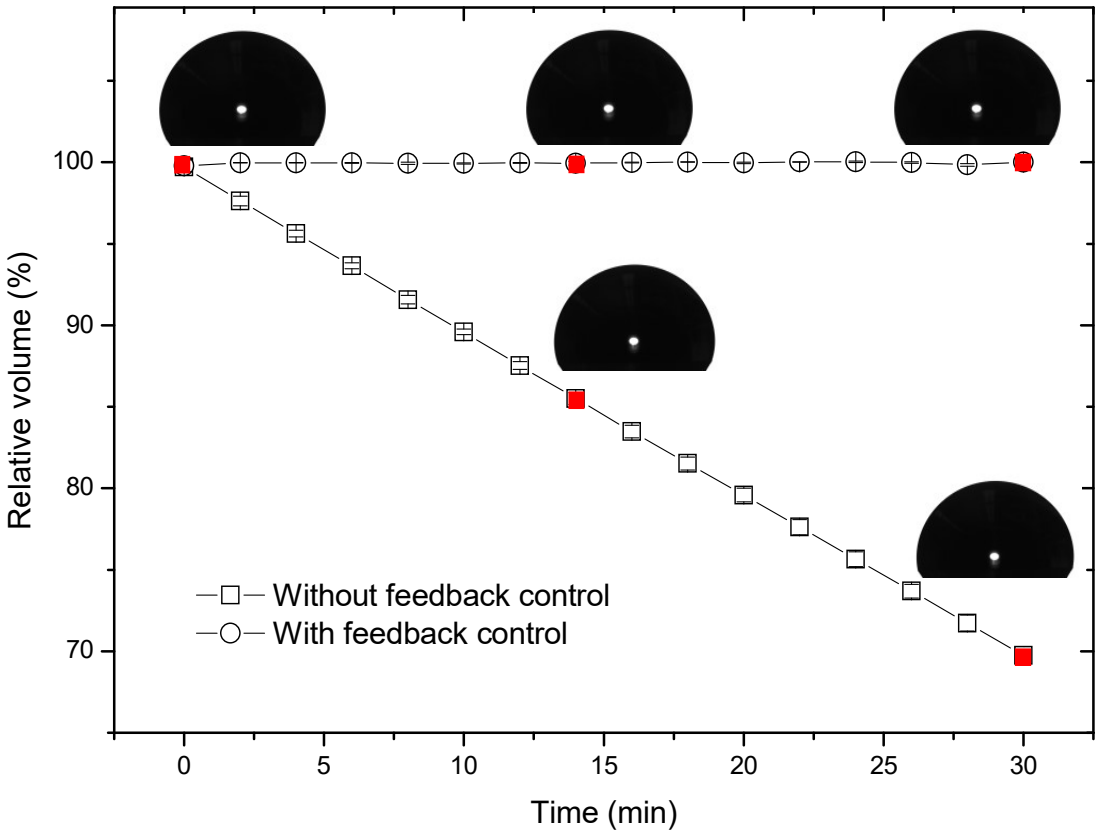

Figure 2.8 Demonstration of the closed-loop ADSA for maintaining constant drop volume by automatically compensating evaporation. Without the control, the volume of a 60 μL water droplet shrinks by 30% over 30 min due to natural evaporation. With the control, the drop volume was maintained at constant over the same time period with volume variations less than 0.5%. Results are shown as mean ± SD averaged from three repetitions. Inserts are drop images at different time points indicated by red solid symbols on the curves, showing changes in drop volume.

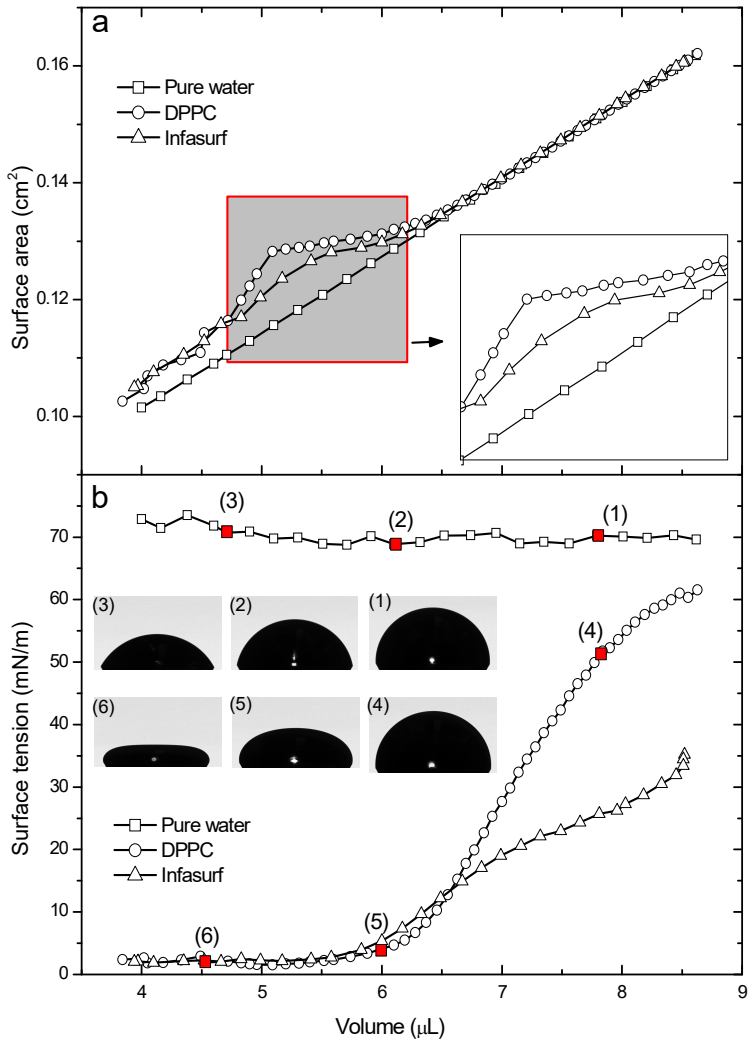

Figure 2.9 Nonlinearity of surface area and surface tension with respect to the drop volume. Three droplets, *i.e.*, a pure water droplet, a DPPC-covered droplet, and an Infasurf droplet, were shrunk linearly in volume. It is clear that only the surface area of the pure water droplet is nearly linearly correlated with the drop volume. Nonlinearity in surface area exists for both DPPC-covered and Infasurf droplets, due to drop deformation upon reducing volume. Surface tensions of all three droplets are nonlinearly correlated with the drop volume, in which the surface tension of pure water remains unchanged while reducing volume, and the surface tensions of DPPC-covered and Infasurf droplets decrease quickly to near-zero value upon reducing volume. Inserts are drop images at different volumes of the three droplets indicated by red solid symbols on the curves.

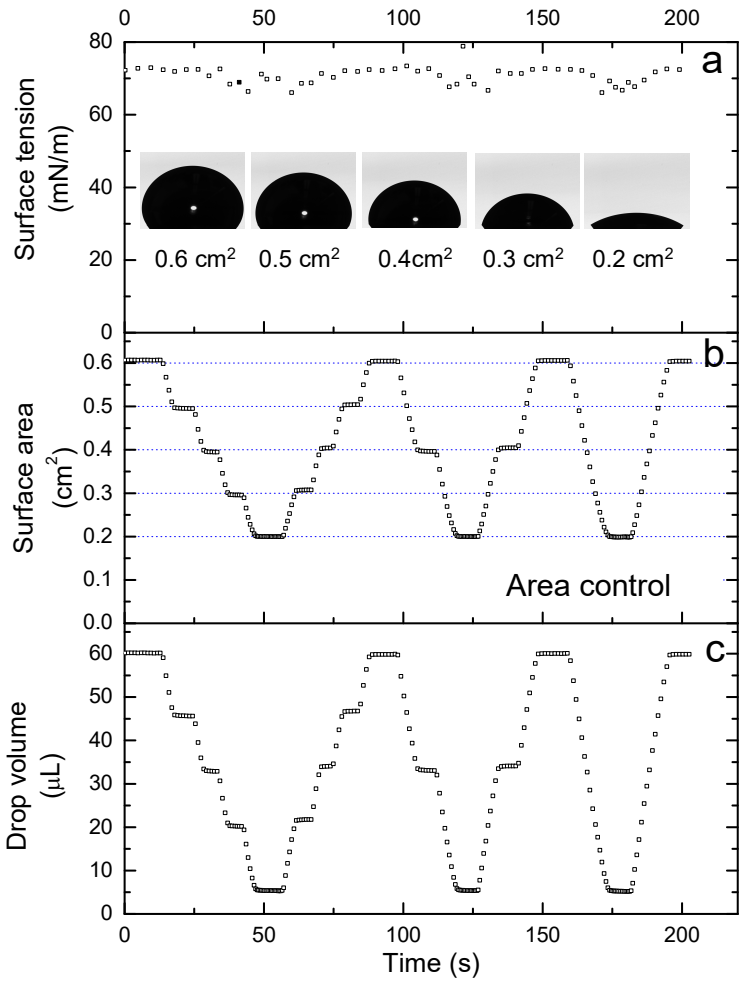

Figure 2.10 Demonstration of the closed-loop ADSA for controlling surface area. The surface area of a 0.6 cm^2 water droplet (panel b) was decreased and increased stepwise with a step of every 0.1 cm^2, followed by steps of every 0.2 cm^2 and 0.4 cm^2, respectively. Images of this droplet at different surface areas are shown as inserts in panel a. It can be found that the change of surface area was controlled largely linear with respect to time without significant overshoot once reaching the target values within a 1% tolerance, with the similar tendency of drop volume control. During the manipulation of surface area, the surface tension (panel a) of pure water is largely unchanged and drop volume follows the same tendency of surface area.

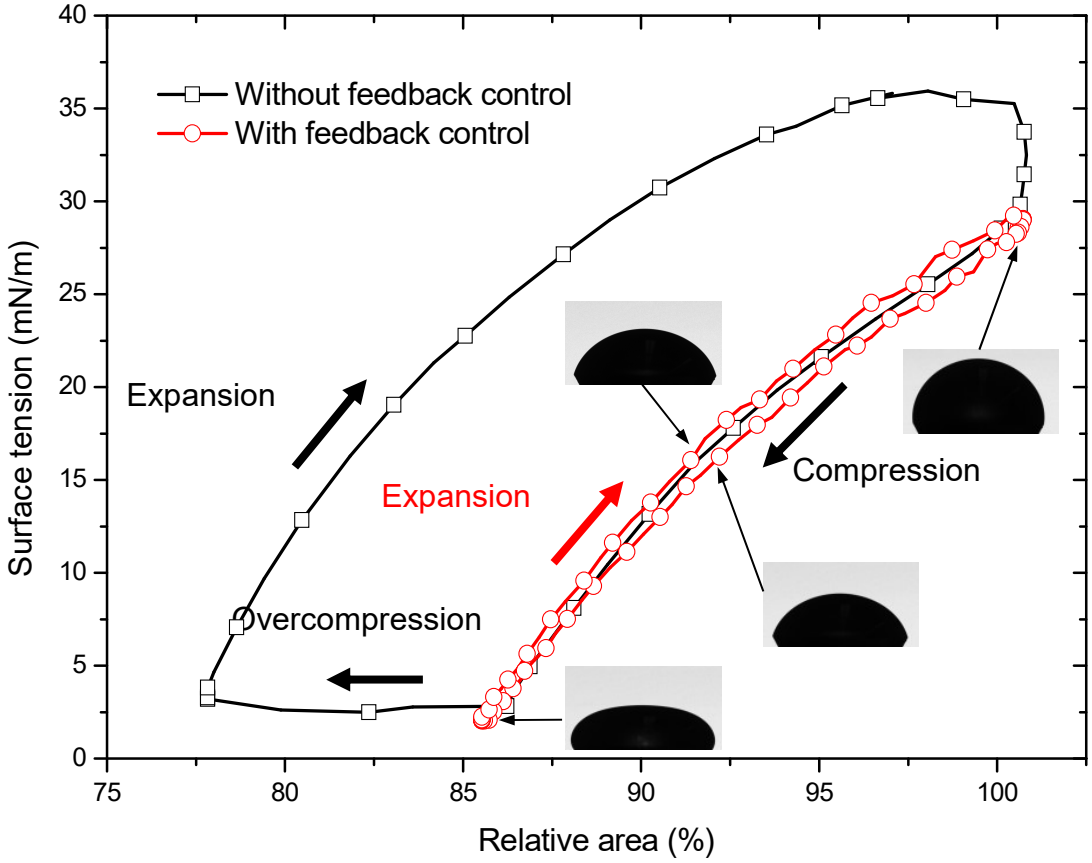

Figure 2.11 Demonstration of the closed-loop ADSA for controlling area variations in biophysical simulation of a natural pulmonary surfactant, Infasurf, under physiologically relevant conditions. With the area control, the surfactant film was compressed precisely by15% area reduction, and subsequently expanded back to its original area. A minimum surface tension of ~2 mN/m was reached with the 15% compression. The compression and expansion curves coincide closely with each other without showing a significant hysteresis. Without the area control, the surfactant film was compressed by 22% area reduction. When the area was reduced beyond 15%, the surface tension did not decrease but leveled off at the minimum value, indicating extensive film collapse, which is an artifact due to overcompression of the surfactant film. Images of the droplets along the cycle path are demonstrative of surface tension being a function of drop shape.

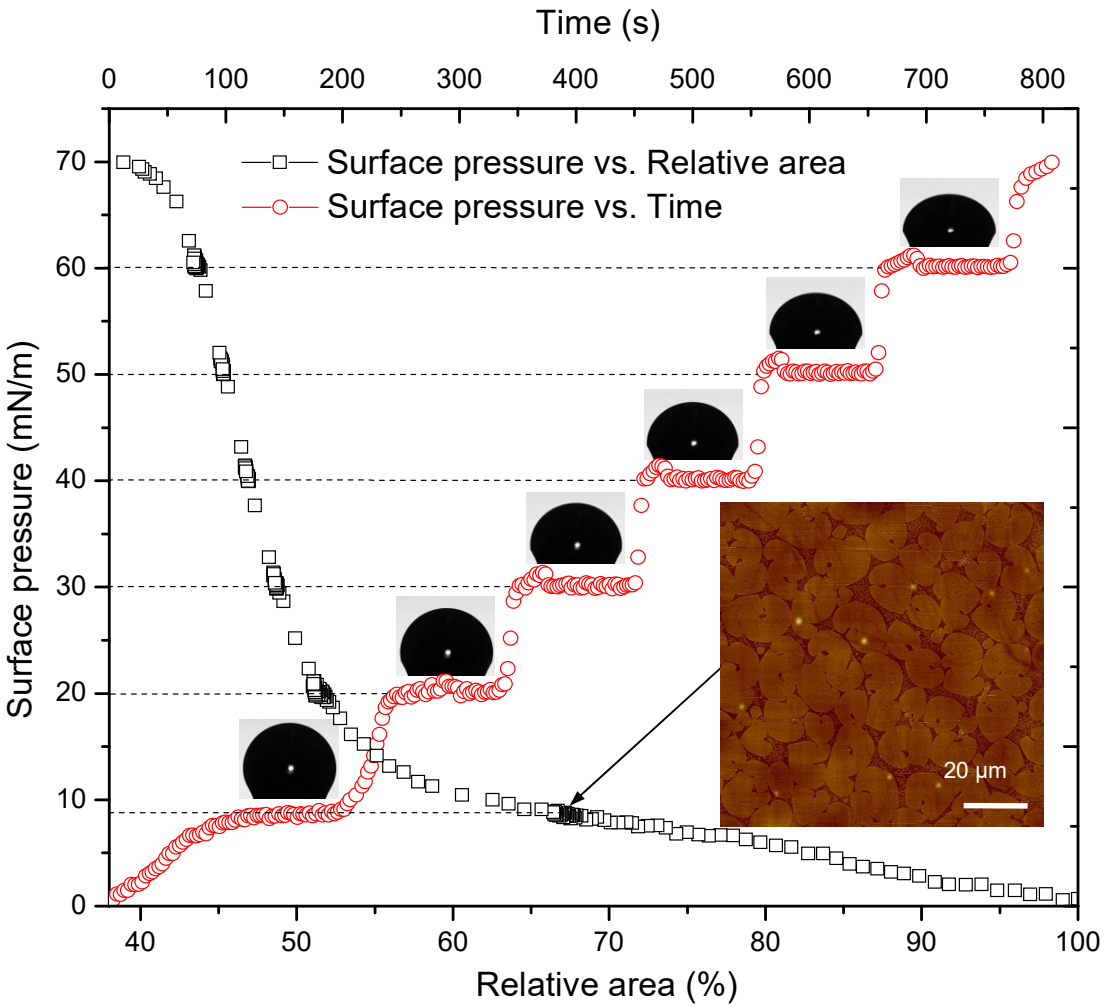

Figure 2.12 Demonstration of the closed-loop ADSA for controlling surface pressure for in situ Langmuir-Blodgett (LB) transfer of DPPC monolayers from the droplet. The obtained surface pressure-area curve is consistent with well-characterized DPPC compression isotherms reported in literature. The surface pressure-time curve shows the compression of the DPPC monolayer to a target surface pressure (*i.e.*, 8.5, 20, 30, 40, 50, and 60 mN/m) and maintained over a 100 s period. When the controlled pressure beyond 30 mN/m, a small overshoot appears due to the hysteresis incurred by stiction of the piston-syringe system. However, the controller is able to correct the overshoot and bring the steady-state surface pressure to the target value. The steady-state error of this control is <1.5%. The insert shows an AFM topographic image (100×100 μm; z-range 5 nm) of the DPPC monolayer transferred under a controlled surface pressure within the phase transition plateau region, *i.e.*, 8.5 mN/m. The image shows clearly coexistence of the LE phase and the signature kidney-shaped TC domains well-documented in literature.

Table 2.1 The benefit decision matrices of five plotting solutions. Usability, the elementary function of the plotting interface, earned a weight of 5 of 10, while other criteria earned lesser weight; and technical options yielded more benefit. The significance of each of the factors was distributed in accordance to the projected relative time over the course of the project.

	Usability (5)	Mathematic Potential (2)	Computing Speed (2)	Friendliness/ Cosmetics (1)	Sum (50)	Percent (100)
MathGL	4 ×5	5 ×2	4 ×2	4 ×1	43	86
GNU plot	4 ×5	4 ×2	4 ×2	3 ×1	39	78
PLplot	3 ×5	4 ×2	4 ×2	2 ×1	34	68
MS Chart Controls	4 ×5	3 ×2	3 ×2	2 ×1	33	66
MiniPlot	3 ×5	2 ×2	3 ×2	1 ×1	25	50
Build Anew	4 ×5	3 ×2	3 ×2	2 ×1	33	66

Table 2.2 The time cost decision matrices of five plotting solutions. For the time cost matrix, more technically challenging options required longer implementation and maintenance times. The significance of each of the factors was distributed in accordance to the projected relative time over the course of the project.

	Construction Costs (4)	Integration Costs (3)	Maintenance Costs (2)	Compilation Costs (1)	Sum (50)	Percent (100)
MathGL	3 ×4	5 ×3	4 ×2	5 ×1	40	80
GNU plot	3 ×4	4 ×3	4 ×2	5 ×1	36	72
PLplot	2 ×4	4 ×3	5 ×2	4 ×1	33	66
MS Chart Controls	2 ×4	3 ×3	3 ×2	3 ×1	26	52
MiniPlot	4 ×4	2 ×3	2 ×2	2 ×1	28	56
Build Anew	4 ×4	1 ×3	1 ×2	1 ×1	22	44

Chapter 3. Arbitrary Waveform Generation

3.1 Introduction

Droplet oscillation has an important role in a wide range of scientific and industrial applications, such as mass transfer,[45] thin films,[6] microfluidics,[46] biophysical simulations,[47] interfacial reactions,[7] and interfacial rheology.[48] In these applications. studying interfacial models through droplet oscillation offers a number of advantages.[49] First, recent advances in droplet tensiometric methodologies have increased the effectiveness of droplet oscillation.[50] Second, the droplet platform has a large surface-area-to-volume ratio which increases the rate of surface reactions and interfacial assemblies. Third, the small volume of droplets can facilitate the study of expensive chemicals, such as scarce biological fluids. Fourth, it is possible to enact a precise environmental control, including the control of temperature, atmosphere, and surface/interfacial composition, thereby avoiding contaminations and allowing versatile investigations across the droplet surface.[51] [2]

Droplet oscillation methods oscillate the droplet through preprogrammed fluid actuation movements, such as motorized syringe pumps. At sufficiently large Bond numbers, *e.g.,* at millimeter-sized diameters and/or at low surface tensions, the droplet deforms significantly from a spherical bead profile, such that the droplet volume and surface area largely deviate from a linear relationship.[15] [17] A number of techniques oscillate volume and surface area of micron-sized droplets with smaller Bond numbers.[12-14] However, when oscillating millimeter-sized droplets with larger Bond numbers, surface area is approximated through volume.[52] Moreover, volume oscillations are largely confined to preprogrammed ramp and sine waveforms. Hence, neither volume nor surface area can be directly and freely oscillated with current techniques.

In this paper, we developed a novel waveform generator for oscillating millimeter-sized droplets, based on axisymmetric drop shape analysis (ADSA). ADSA is a computational droplet measurement technique developed by Neumann et al.[1 4] ADSA determines the volume, surface area, and surface tension of a droplet numerically by fitting the experimental droplet profile to theoretical droplet profiles from the Laplace equation of capillarity. Recently, ADSA was coupled with real-time analysis and feedback control to manipulate droplet volume, surface area, and surface tension.[17] Extending upon this work, we developed, to the extent of our knowledge, the first waveform generator capable of directly controlling a droplet's volume or surface area to an arbitrary waveform. Through this waveform generator, we can oscillate millimeter-sized droplets with a high degree of freedom and accuracy, up to reported limiting frequencies and to an amplitude not previously possible.[53]

We demonstrate the strengths, applicability, and limitations of this droplet manipulation method in three ways. First, we demonstrated arbitrary waveform generation by controlling the volume and surface area of a pure water droplet to sine, triangle, square, and sawtooth waveforms. Second, we evaluated the accuracy of the arbitrary waveform generation through a coefficient of determination (R^2) analysis. Third, we apply arbitrary waveform generation to study the interfacial dilational rheology of adsorbed surfactant films.

3.2 Materials and Methods

3.2.1 Materials

Water used was Milli-Q water with resistivity greater than 18 MΩ·cm, filtrated by Millipore Corporation. (Millipore, Billerica, MA). C_{12}DMPO (MW=246.4 g/mol) used was from

Sigma-Aldrich Chemistry and used without further purification. A phosphate buffer solution of Na_2HPO_4 and NaH_2PO_4, from Sigma-Aldrich Chemistry, with ion strength of 0.03 (pH=7) and surface tension of 72.5mN/m, was used to dissolve the surfactant and proteins. On day of the experiment, a stock solution was prepared and diluted to desired concentrations. All measurements were at room temperature (20±1ºC).

3.2.2 Methods

The CDS is the experimental setup and the plant of the control system. The measurement in the control system is Axisymmetric Drop Shape Analysis, a computational technique written in C and C++. An image of the droplet is acquired by a machine vision camera (Model PLB-771U, PixeLink), and is fetched by an ADSA-based application. First, ADSA extracts the profile of the droplet through edge detection, to produce a 2D array of the edge pixel coordinates, known as the experimental profile. Second, a series of theoretical curves, with predefined physical properties, are generated through the Bashforth-Adams equation (Eq. 1.1), where axisymmetric interfaces can be expressed as a function of the arc length *s*:

$$\frac{d\theta}{ds} = \frac{2}{R_0} + \frac{\Delta\rho g}{\gamma} z - \frac{\sin\theta}{x} \qquad \text{(Eq. 3.1)}$$

$$\frac{dx}{ds} = \cos\theta \qquad \text{(Eq. 3.2)}$$

$$\frac{dz}{ds} = \sin\theta \qquad \text{(Eq. 3.3)}$$

$$x(0) = 0, z(0) = 0, \theta(0) = 0 \qquad \text{(Eq. 3.4)}$$

where θ is the tangential angle, *x* is the radius, and *z* is the height, R_0 is the curvature at the origin, and $\Delta\rho g / \gamma$ is the capillary constant of the system.[1] Third, a numerical fitting scheme fits and selects the theoretical drop profiles to the experimental profile, thereby outputting corresponding properties of the drop/bubble, including volume, surface area, and surface tension.

ADSA is capable of sampling up to a fast frequency of 10 Hz.[17] Recently, CDS based experiments was developed into a closed-loop control system where sampled droplet properties are fed back to control droplet/bubble toward a desired target.[17] A precise target volume, surface area, or surface tension can be reached through PID control:

$$u(t) = k_p * e(t) + \int_0^t k_i * e(\tau)\, d\tau + k_d \frac{de(t)}{dt} \quad \text{(Eq. 3.5)}$$

$$\mathrm{U(s)} = k_p * \mathrm{E(s)} + \left(\frac{k_i}{s}\right) * \mathrm{E(s)} + k_d * s * \mathrm{E(s)} \quad \text{(Eq. 3.6)}$$

$$\mathrm{U(z)} = k_p * \mathrm{E(z)} + \left(\frac{k_i}{1-\frac{1}{z}}\right) * \mathrm{E(z)} + k_d * (1 - \frac{1}{z}) * \mathrm{E(z)} \quad \text{(Eq. 3.7)}$$

Where k_p is the proportional gain, k_i is the integral gain, k_d is the derivative gain, e is the value of the error, and u is the value of the command signal, expressed as a function of t in the time domain, as a function of s in the Laplace domain, as a function of z in the Z domain. For most transients, the settling time is less than 5 seconds.[17]

3.3 Development of Waveform Generator.

Here, we extend the close-loop control to waveform generation. An arbitrary waveform is discretized to intervals up to 0.20s, bottlenecked by the motor's cycle between different movements. Through the discretize intervals, we control the volume or surface area to the arbitrary waveform. Prior to each interval, the error, *i.e.*, the difference between the current droplet value and the target value of the next interval, is calculated. Thereafter, the feedback control actuates the droplet through a motorized syringe. Parallel to PID control, to minimize oscillatory transients, a fuzzy control component is added. Moreover, through previous waveform periods, the PID gains and the fuzzy table can be fined tuned to minimize future error.

ADSA then feeds back and updated data for upcoming intervals and periods. A diagram of the flowchart of this waveform generation is illustrated in **Figure 1**.

There are a number of advantages and novelties of this waveform generation compared to previous drop/bubble oscillation methods:

1. This waveform generator is the first method capable of directly feedback controlling the volume and surface area of millimeter-sized droplets. In most oscillation methods, droplet surface area is approximated from its volume. However, given a sufficiently large Bond number, from droplet size and/or the presence of surfactants, the droplet deforms from a spherical bead profile, such that droplet surface area and volume are not linear with respect to each other.[17]

2. The waveforms demonstrated here are sine, triangle, square, and sawtooth waves. However, this waveform generator is not constrained to the waveforms shown here. Due to its principle of operation, this waveform generator can generate any arbitrarily defined waveform, similar to arbitrary waveform generators for electric signals.

3. Closed-loop ADSA is a free-standing method that can manipulate droplet in four different configurations. Although waveforms demonstrate here is through the sessile drop; pendant drop, pendant bubble, and sessile bubble are also applicable.

4. This waveform generator is independent of the physical method of fluid actuation, regardless driven through motorized syringes, piezoelectric transducers, or any other means. Faster fluid actuation methods are expected generate waveforms at even higher frequencies.

5. These waveforms can be generated at a frequency that coincides with the limiting frequency of other drop/bubble oscillation systems.[53] However, these waveform can be generated at significantly higher amplitudes.

3.4 Results and Discussion

3.4.1 Control of Droplet Volume and Surface Area

In this study, we demonstrate the generation of droplet volume and surface area waveforms of periodic functions of sine, triangle, square, and sawtooth. These four functions represent simple examples of periodic waveforms. a combination of these four or a part thereof can produce any arbitrary waveform. Volume and surface area are generated through the following equations:

$$\mathrm{Sine}(A_0,\ A,\ \omega,\ \varphi) = \mathrm{A}_0 + \mathrm{A} * \sin(\omega(t\ + \varphi)) \qquad \text{(Eq. 3.8)}$$

$$\mathrm{Triangle}(A_0,\ A,\ \omega,\ \varphi) = A_0 + 4\mathrm{A} * \omega((t + \varphi) - \frac{1}{2\omega}\left\lfloor 2\omega(t + \varphi\ ) + \frac{1}{2}\right\rfloor)(-1)^{\left\lfloor 2\omega(t+\varphi)+\frac{1}{2}\right\rfloor} \qquad \text{(Eq. 3.9)}$$

$$\mathrm{Square}(A_0,\ A,\ \omega,\ \varphi) = A_0 + \mathrm{A} * \mathrm{sgn}(\sin(\omega(t\ + \varphi)) \qquad \text{(Eq. 3.10)}$$

$$\mathrm{Sawtooth}(A_0,\ A,\ \omega,\ \varphi) = A_0 + \mathrm{A} * \omega((t + \varphi) - \frac{1}{\omega}\lfloor\omega(t + \varphi\ )\rfloor) \qquad \text{(Eq. 3.11)}$$

where A_0 is the offset, A is the amplitude, ω is the angular frequency, and φ is the phase shift. All four parameters of $A_0,\ A,\ \omega,$ and φ can be controlled. There are multiple equations to express some of these waveforms, and presented are general forms selected owning to lower computational costs. **Figure 3.2** shows the generation of periodic functions including, sine, triangle, square, and sawtooth of a water droplet on the CDS platform at room temperature.

In volume control, drops are controlled an offset of 15 μl, an amplitude of 20%, and a period of 20s. In surface area control, drops are controlled to an offset of 0.25cm2, an amplitude of 20%, and a period of 20s. **Figure 3.3** demonstrations surface tension control through sinusoidal waveform generation. **Figure 3.4** demonstrations of evaporation compensation through sinusoidal waveform generation. The ideal waveform is inserted as a red line. It is clear the volume and surface area follow the ideal waveforms very closely, except during the instantaneous jump of the square and sawtooth waves.

3.4.2 Evaluation of the Waveform Generation Accuracy and Limitations.

In this study, we demonstrate the accuracy of the waveform generation. **Figure 3.5.1** shows the coefficient of determination (R^2) analysis of periodic functions including, sine, triangle, square, and sawtooth of a water droplet on the CDS platform at room temperature. Three parameters of parameters of $A_0,\ A,$ and ω are controlled. Here, R^2 is calculated on a fixed $A_0,\ A,$ and ω through a Levenberg–Marquardt algorithm, such that this calculation encompasses both the relative error of $A_0,\ A,$ and ω and the closeness to the wave profile. Volume and surface area are controlled to an offset of 15 μl and 0.02 cm^2. Volume is controlled to an amplitude to 10% and 20%, 1.5 and 3 μl, respectively. Surface area is controlled to an amplitude to 10% and 20%, 0.02 and 0.04 cm^2, respectively. Volume and surface area are controlled to an oscillation frequency of 0.01Hz, 0.025Hz, 0.05Hz, 0.1Hz, 0.2Hz, and 0.5Hz.

The R^2 value is similar for both volume waves and surface area waves, and similar for both 10% and 20% amplitude variations. The R^2 value marginally deteriorates for triangle waveforms, due to the sharp peaks and crests with respect to a sine wave. The R^2 value deteriorates for square and sawtooth waveforms, due to the instantaneous jumps, and possible

ensuing oscillatory behaviors. The R^2 value deteriorates for waveforms frequencies above 0.1Hz. ADSA can sample at a frequency of ~10 Hz, and the limiting motor cycle is ~5 Hz, such that the motor cycle is assumed to be the bottleneck. For example, waveforms with a waveform with a frequency of 0.5Hz is allotted a maximum of 10 motor movements, incurring a sharper wave profile. Given a fluid actuation method with a faster turnaround time, this is expected to improve.

To quantify the limitations the waveform generation, a R^2 value of over 0.9 is defined and benchmarked as excellent waveform tracking. **Figure 3.5.2** illustrates this. It can be observed that the R^2 value is high and over 0.9 across the entire examined frequency spectrum for sine and triangle waveforms. For square and sawtooth waveforms, the R^2 value is over 0.9 for frequencies of 0.05Hz and 0.1Hz and below. From this, it can be concluded that frequencies below this benchmark can be administered acceptable tracking for various applications.[53]

3.4.3 Dilational Rheology Investigation

In this study, we engage the sinusoidal waveform generation to study dilational rheology. Dilational rheology is relevant in numerous technical and natural processes, including mass transfers, monolayers, foams, and emulsions.[54-55] In general, interface rheology studies mechanical modifications induced by elastic and viscous dilational and shear stress.[56] Dilational rheology can study the properties and composition of interfacial layers of proteins, lipids, polymers, particles, and surfactants.[54] The surface dilational rheology modulus, a complex number with a real part equal for surface elasticity and an imaginary part for surface viscosity, can be determined from surface area perturbations and resulting surface tension responses. A variety of methodologies have been developed for dilational rheology investigations, including oscillating barriers, [57-58], drop shape analysis.[59-61], capillary pressure,[62] and bubble pressure.[63-64]

A widely-used methodology for investigating dilational rheology is drop/bubble oscillation through surface tensiometry, where interfacial tension varies due to controlled surface area modifications. In modern drop/bubble profile tensiometry (DPT), surface area variation is possible through feedback control.[50] However, accurate droplet oscillation has many complications and limitations. Inaccurate surface area oscillation will lead to inaccurate surface tension oscillation, thereby resulting in inaccurate dilational rheology measurements. It is possible ensure greater accuracy in piezo-driven systems capable of nanometer step sizes,[65] however, this imposes inhibitions in the amplitude and frequency of the oscillation. In addition, the upper frequency limit may lead to artefacts in surface tension measurement.[53]

To demonstrate waveform generation in a dilational rheology study, a typical system of low molecular-weight surfactant is selected. The non-ionic surfactant dodecyldimethylphosphine oxide (C_{12}DMPO) was measured at different frequencies. The result was compared with experimental results in the literature. This application has demonstrated that the waveform generator is highly practical in studying the surface dilational rheology.

Surfactant can be considered as a thin film on a liquid surface such that the normal stress on any sectional area is the same. This is demonstrated in **Figure 3.6.** If we consider a small square region, there are normal stresses on each side of the square plate. This biaxial loading can be separated to the uniaxial loading along x and y directions. From stress along the *x* direction, the strain along *x* and *y* directions are defined as ε_x' and ε_y', and from stress along the *y* direction, the strain along *x* and *y* directions are defined as ε_x'' and ε_y'':

$$\varepsilon_x' = \frac{\sigma}{E},\ \varepsilon_y' = -\nu\frac{\sigma}{E} \qquad \text{(Eq. 3.12)}$$

$$\varepsilon_x'' = -\nu\frac{\sigma}{E},\ \varepsilon_y'' = \frac{\sigma}{E} \qquad \text{(Eq. 3.13)}$$

thus, from a biaxial perspective, the strain can be given as:

$$\varepsilon_x = \varepsilon_x' + \varepsilon_x'' = \frac{1-\nu}{E}\sigma,\ \varepsilon_y = \varepsilon_y' + \varepsilon_y'' = \frac{1-\nu}{E}\sigma \ \rightarrow\ \varepsilon_x = \varepsilon_y = \frac{1-\nu}{E}\sigma \qquad \text{(Eq. 3.14)}$$

where ε_x' and ε_y' are strains along the x direction, ε_x'' and ε_y'' are strains along the y direction, ε_x and ε_y are strains from a biaxial perspective, σ is the stress, E is the modulus, and ν is the Poisson's ratio.

The surface dilational modulus, a complex quantity with a real part expressing surface elasticity and an imaginary part expressing surface viscosity, can be determined from harmonic surface area perturbations and resulting surface tension responses.[48] For elastic behavior, the surface stress is proportional to the relative surface area perturbation. For viscous behavior, the surface stress is proportional to the rate of surface area perturbation.[66] A general expression for the surface dilational modulus is:

$$E = \frac{\Delta\gamma}{A/A_0} = E_0 + i2\pi\omega\eta = E_r + iE_i \qquad \text{(Eq. 3.15)}$$

where E is the dilational viscoelasticity modulus, $\Delta\gamma$ is amplitude of surface tension variations, A_0 is the reference surface area, A is the amplitude of the surface area oscillation, ω is the angular frequency of the harmonic surface area oscillations, E_0 is the dilational elasticity, η is the dilational viscosity, $E_0 = E_r$ is the real part of the dilational modulus, and $2\pi\nu\eta = E_i$ is the imaginary part of the dilational modulus.

When investigating the dynamics of interfacial layers, the dilational modulus is significant given its relation to the frequency of surface area perturbations.[54] Usually, in

experiments involving harmonic surface area perturbations, a frequency sweep of surface area occurs in the following form:

$$A = A_0 + \tilde{A}\sin(2\pi\omega t) \quad \text{(Eq. 3.16)}$$

where A is surface area, A_0 is the reference surface area, $\tilde{A}$ is the amplitude of surface area oscillations, and ω is the frequency. The harmonic response of surface tension γ is:

$$\gamma = \gamma_0 + \tilde{\gamma}\sin(2\pi\omega t + \varphi) \quad \text{(Eq. 3.17)}$$

where γ is the surface tension, γ_0 is the equilibrium reference surface tension, $\tilde{\gamma}$ is amplitude of surface tension variations, and φ is the phase shift between the surface area perturbations and surface tension response. Here, A_0, $\widetilde{A}$, and ω are controlled through the waveform generator, γ_0, $\tilde{\gamma}$ and φ are extracted through a Levenberg–Marquardt curve fit of the measured surface tension. The phase shift φ is the phase of the complex dilational modulus, and the elastic and viscous moduli can be determined experimentally:

$$|E| = A_0 \frac{\tilde{\gamma}}{\tilde{A}} \quad \text{(Eq. 3.18)}$$

$$|E_r| = A_0 \frac{\tilde{\gamma}}{\tilde{A}}\cos(\varphi) \quad \text{(Eq. 3.19)}$$

$$|E_i| = A_0 \frac{\tilde{\gamma}}{\tilde{A}}\sin(\varphi) \quad \text{(Eq. 3.20)}$$

To demonstrate dilational rheology measurement, the widely studied non-ionic surfactant dodecyldimethylphosphine oxide (C_{12}DMPO) is studied. A surface area frequency sweep is applied to measure the dilational rheology modulus of C_{12}DMPO at different frequencies. The result was compared with experimental results in literature. **Figure 3.7** demonstrates the

dilational rheology modulus measurement of C_{12}DMPO (c=0.22 mM) on the CDS platform at room temperature. (a) In this control, the droplet is controlled to an offset of 0.2cm^2 and an amplitude of 10%. The ideal waveform is inserted as a red line. It is clear the surface area follows the ideal waveform closely. The blue line is the Levenberg–Marquardt curve fit of the surface tension measurement. The amplitude and phase lead of the surface tension response is 1.9 mN/m and 20^o, respectively. (b) Real and imaginary parts of surface dilational modulus of C_{12}DMPO (c=0.22 mM), measured at frequencies of 0.01Hz, 0.025Hz, 0.05Hz, 0.1Hz, 0.2Hz, and 0.5Hz. Literature surface dilational modulus values at frequencies of 0.01Hz, 0.02Hz, 0.04Hz, 0.08Hz, 0.16Hz, 0.32Hz, and 0.5Hz are included in this figure.[6363] This study has demonstrated the waveform generator is highly applicable in studying surface dilational rheology.

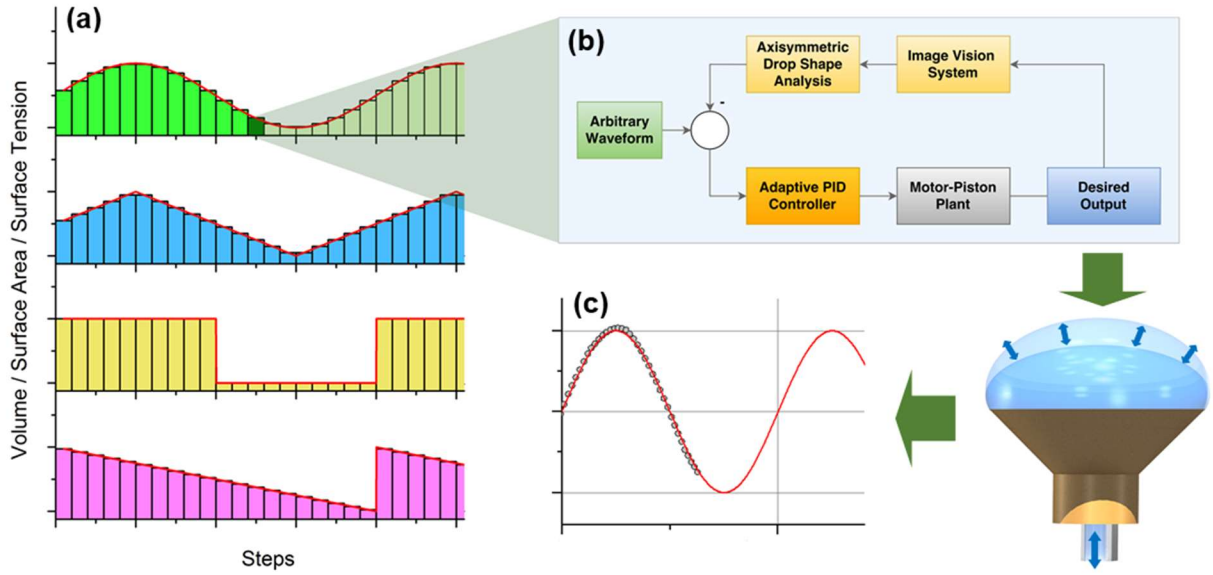

Figure 3.1. Schematic arbitrary waveform generation for droplet volume and surface area. (a) Four waveforms demonstrated are sine, triangle, square and sawtooth waves. To achieve tracking, the waveforms discretized to a series of intervals, each a control loop to actuate the droplet. (b) Schematic for the control loop of every interval. Through a modified proportional-integral-derivative (PID) control and servomotor piston-syringe plant, the droplet is controlled to the target of the interval, collectively generating waveforms. (c) The resulting image is fetched by an image processing algorithm and Axisymmetric drop shape analysis (ADSA) to produce experimental results.

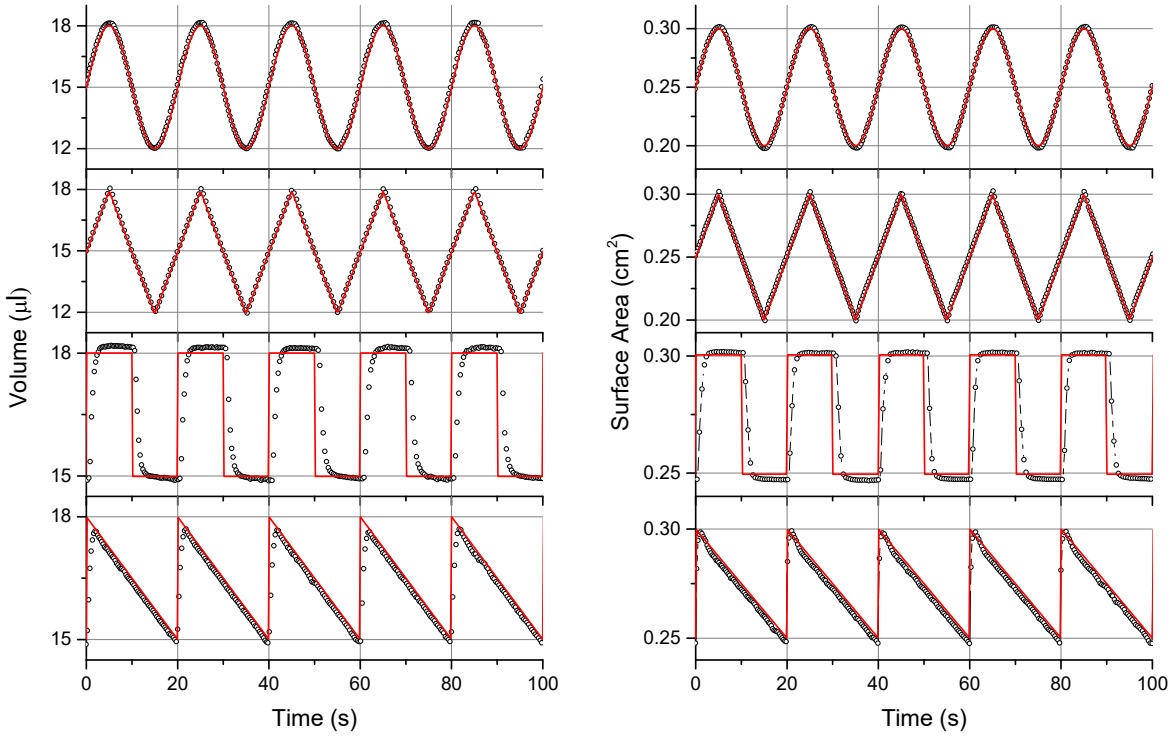

Figure 3.2. Demonstration of waveform generation for droplet volume and surface area of pure water on the CDS platform at room temperature. Four waveforms demonstrated are sine, triangle, square, and sawtooth waves. In volume control, drops are controlled an offset of 15µl, an amplitude of 20%, and a period of 20s. In surface area control, drops are controlled to an offset of 0.25cm^2, an amplitude of 20%, and a period of 20s. The ideal function is inserted as a red line. It is clear volume and surface area follows the ideal waveform closely.

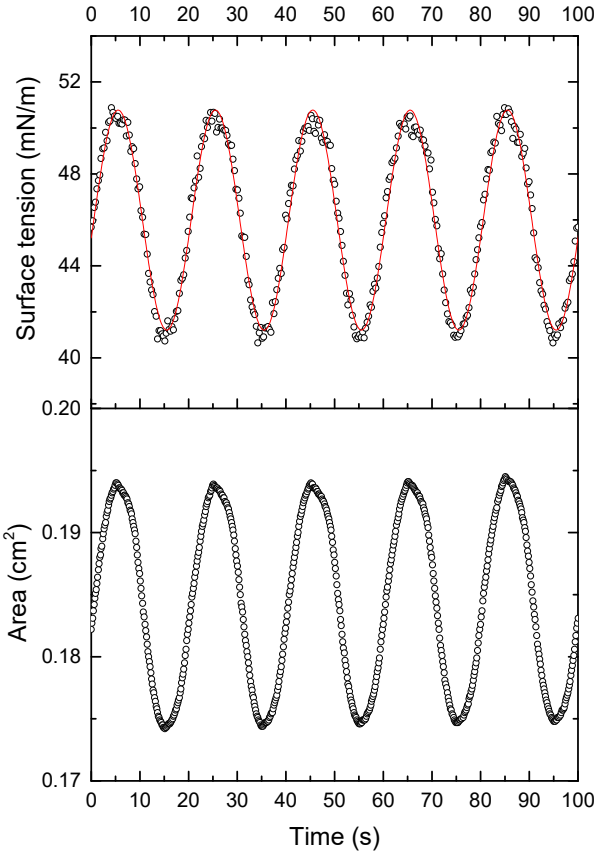

Figure 3.3. Demonstration of sinusoidal waveform generation of surface tension of DOPC on the CDS platform at room temperature. Drops are controlled an offset of 46 mN/m, an amplitude of 5 mN/m, and a period of 20s. The ideal function is inserted as a red line. While there is noise surface tension sampling, it is clear volume and surface tension wave follows the ideal waveform closely.

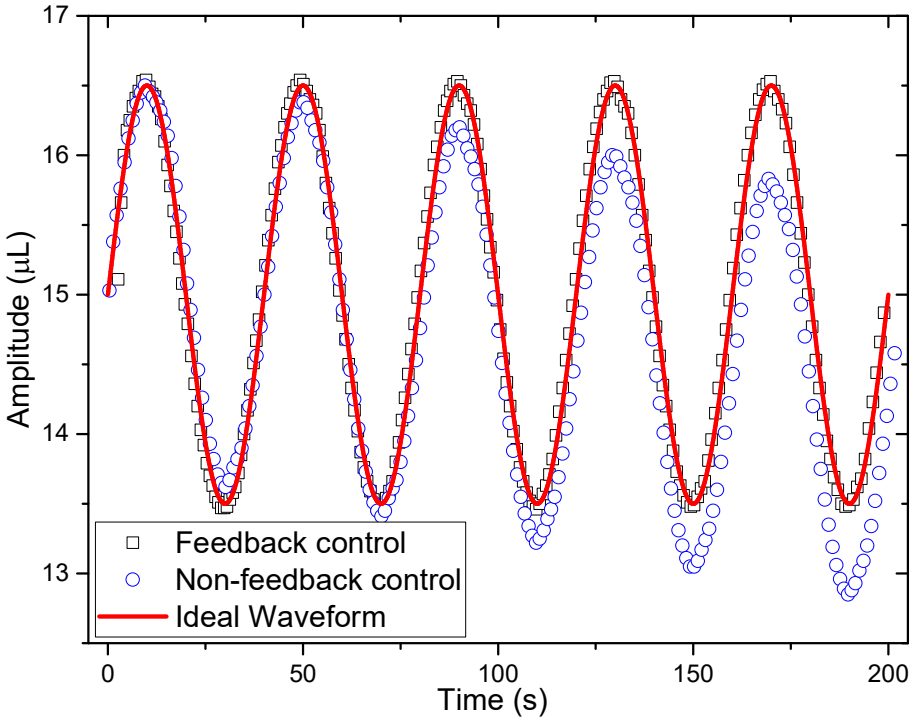

Figure 3.4. Demonstration of sinusoidal waveform generation volume by automatically compensating evaporation. Two waveforms of feedback waveform generation and non-feedback waveform generation are controlled an offset of 15µl, an amplitude of 10%, and a period of 40s. The ideal function is inserted as a red line. Without feedback control, droplet volume shrinks significantly over 200 seconds due to natural evaporation. With feedback control, droplet volume was controlled in the same time period, following the ideal waveform closely.

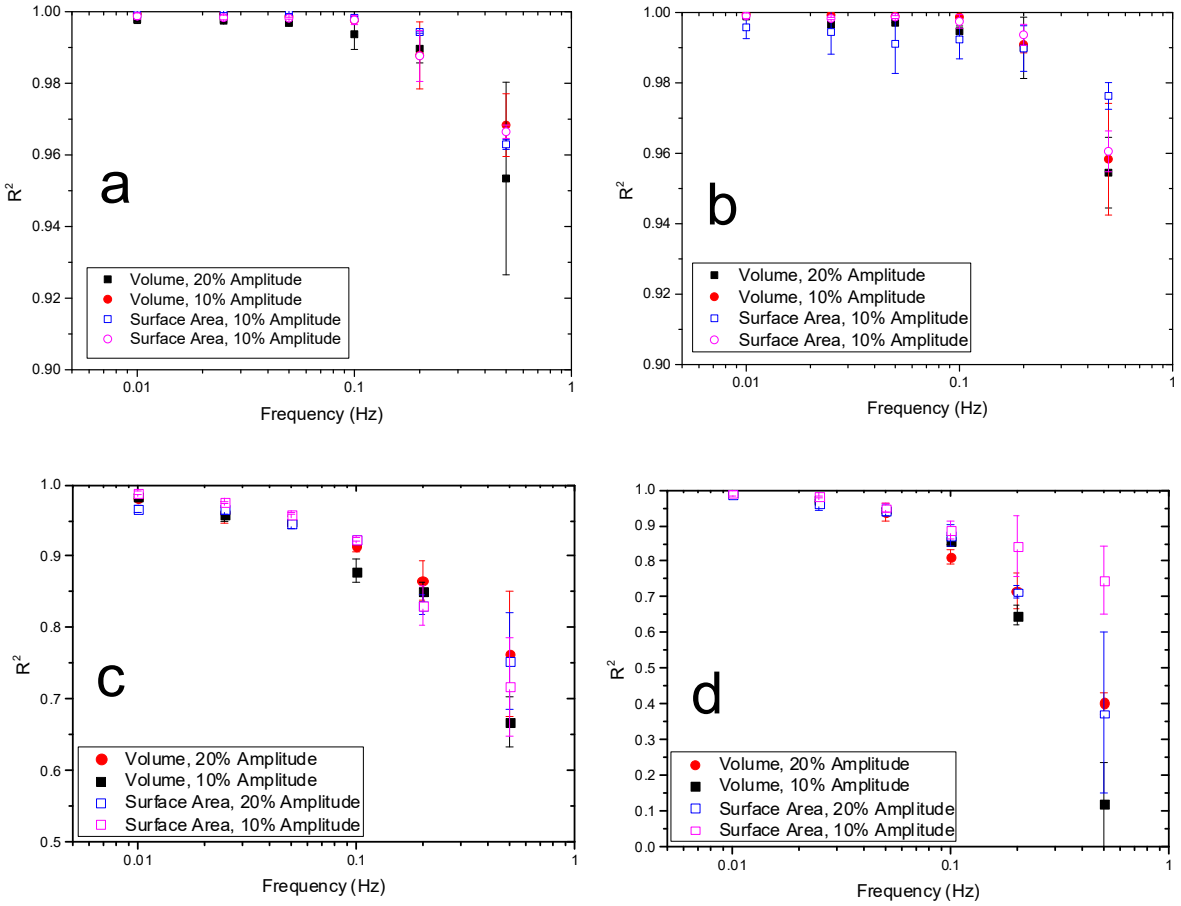

Figure 3.5.1 Accuracy evaluation of waveforms using the coefficient of determination or R^2 for (a) sine, (b) triangle, (c) square, and (d) sawtooth waveforms, for volume and surface area at two amplitudes (10% and 20%). Six frequencies are evaluated, 0.01Hz, 0.025Hz, 0.05Hz, 0.1Hz, 0.2Hz, and 0.5Hz. Four observations can be made. 1. The coefficient of determination is similar for both volume waves and surface area waves. 2. The coefficient of determination is similar for both volume control and area control for both 10% and 20% amplitude variations. 3. The coefficient of determination deteriorates at high frequencies of 0.2hz, and 0.5hz. 4. The coefficient of determination deteriorates for square and sawtooth waveforms.

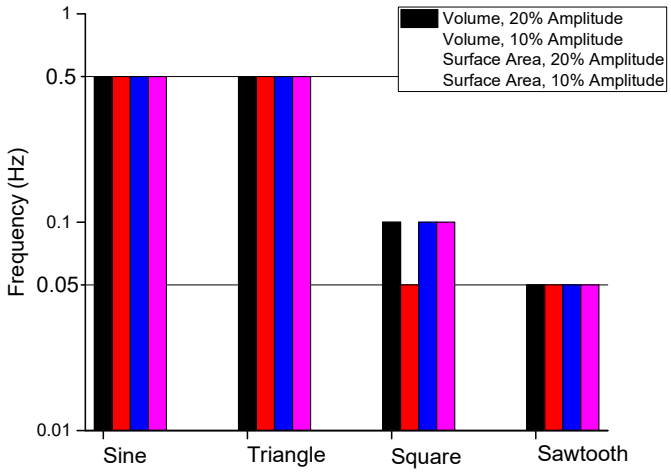

Figure 3.5.2 Evaluation of waveform generation based on the coefficient of determination. The coefficient of determination threshold of the waveforms is defined 0.9, beyond which, the experimental waveform is evaluated to track the ideal waveform with a high degree of accuracy. For higher frequencies above 0.2hz and 0.5hz, the accuracy decreases due to sampling limitations and motor limitations. For square and sawtooth waveforms, accuracy decreases due to the transience of the instantaneous jump. The accuracy decreases when frequency increases from 0.5 Hz or 0.1 Hz.

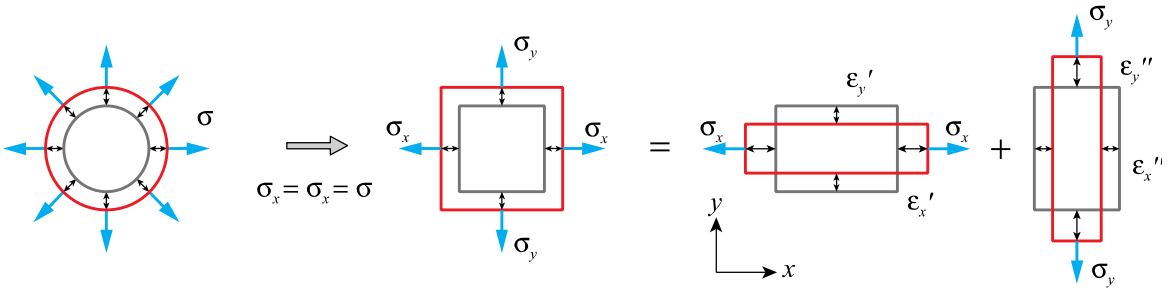

Figure 3.6 Diagram of biaxial loading and uniaxial loading. On the left, a surfactant film experiences normal stress on all directions. If we consider a small square region, there are normal stresses on each side of the square plate. This biaxial loading can be separated to the uniaxial loading along x and y directions. From stress along the *x* direction, the strain along *x* and *y* directions are defined as ε_x' and ε_y', and from stress along the *y* direction, the strain along *x* and *y* directions are defined as ε_x'' and ε_y'':

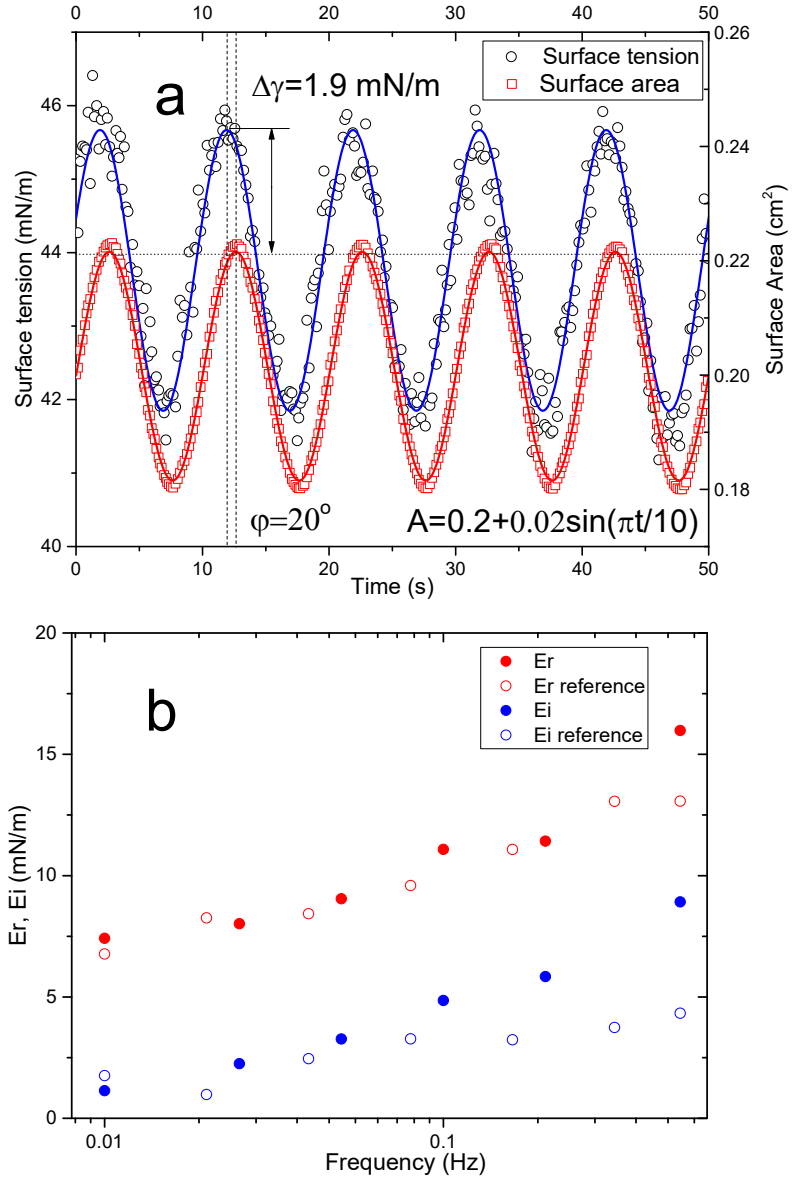

Figure 3.7 Demonstration of sinusoidal waveform generation of surface area of C12DMPO (c=0.22 mM) on the CDS platform at room temperature. (a) In this control, drops are controlled to an offset of 0.2cm^2, an amplitude of 10%, and a period of 10s. The ideal function is inserted as a red line. It is clear volume and surface area follows the ideal waveform closely. The dashed blue line is the best sinusoidal fitting of the surface tension, and the phase lead of surface tension is 20^o. The amplitude of the surface tension response is 1.9 mN/m. (b) Real and imaginary parts of surface dilational modulus of C_{12}DMPO (c=0.22 mM), calculated for frequencies of 0.01Hz, 0.025Hz, 0.05Hz, 0.1Hz, 0.2Hz, and 0.5Hz. Literature surface dilational modulus values at frequencies of 0.01Hz, 0.02Hz, 0.04Hz, 0.08Hz, 0.16Hz, 0.32Hz, and 0.5Hz are included in the figure.

Chapter 4. Conclusions and Recommendations

4.1 Summary of Contributions

1. I developed a unified droplet/bubble coordinate system, through C and C++. Combined with ADSA and the experimental setup CDS, we measure both surface and interfacial tensions for four configurations, *i.e.*, sessile drop, pendant drop, sessile bubble, and pendant bubble. The measurements of surface and interfacial tensions for a number of surface and interfaces demonstrated the accuracy and feasibility of the ADSA and the CDS.

2. I developed a feedback control system with ADSA, through C and C++. I interfaced the feedback control system with the CDS to manipulate droplets. Closed-loop ADSA extends the applications of the CDS from a surface tension measurement methodology to a sophisticated tool for automatically manipulating droplets in real-time. We have demonstrated the feasibility and advantages of closed-loop ADSA in three applications, including control of drop volume by automatically compensating natural evaporation, precise control of surface area variations for high-fidelity biophysical simulations of natural pulmonary surfactant, and steady control of surface pressure for *in situ* Langmuir-Blodgett transfer from droplets. The closed-loop ADSA holds great promise for advancing droplet manipulation in a variety of material and surface science applications, such as thin-film fabrication, self-assembly, and biophysical study of pulmonary surfactant.

3. I developed an arbitrary waveform generator for droplets and bubbles, through C and C++. To demonstrate this droplet manipulation method, we engaged in demonstration, evaluation, and application. First, we demonstrate arbitrary waveform generation through manipulating a pure water droplet's volume and surface area to sine, triangle, square, and

sawtooth waveforms. The amplitude and period of the waveform is precisely controlled. Second, we evaluate arbitrary waveform generation through a coefficient of determination (R^2) analysis. Third, we apply arbitrary waveform generation to dilational rheology measurement for layers of surfactants. The strengths, applicability, and limitations of our method will also be discussed.

4.2 Recommendations

4.2.1 Parallel Computing ADSA

Through the advances of multi-core processors. parallel computing has become the paradigm in computer architecture. Parallel computing allows for many calculations to executions simultaneously. Distributing the computation of ADSA can potentially increase its sampling speed by an order of magnitude. Parallel loops, parallel tasks, and parallel aggregation can be sequentially implemented. Parallelization issues including but not limited to deadlocking will need to be minimized. OpenMP API and the Microsoft developer network may be good places to start.

4.2.2 Image Processing Techniques

Image processing is applying algorithms on images for processing. A wide range of operations can be applied to the image. Superior image processing techniques will improve the sampling time of ADSA without the loss of quality, this includes but is not limited to fast canny analysis and SUSAN edge detection.

4.2.3 Machine Learning Feedback Control

Adaptive control is a control method where a controller adapts to a controlled system. Adaptive control does not operate upon previous information regarding the time-varying parameters. Given the error of the waveform changes with different control parameters, a machine learning control algorithm can be implemented to minimize error in future cycles or periods.

Vita

Kyle Yu received his Bachelors of Applied Science in Mechatronics Engineering from the University of Waterloo, Waterloo, Ontario, Canada, in 2016. He worked as a control system engineer for the Department of Mechanical Engineering in the University of Hawaii at Manoa, in 2013 and 2015. He is a candidate for a Master of Science in Mechanical Engineering degree from the University of Hawaii at Manoa, in 2017. The title of his thesis is "Feedback Control in Droplet Manipulation".

Papers of refereed journals for publication:

1. Yang, J., **Yu, K.,** and Zuo, Y. Y. (2017). Accuracy of axisymmetric drop shape analysis in determining surface and interfacial tensions. *Langmuir*, *33*(36), 8914-8923.

3. **Yu, K.*,** Yang, J.*, and Zuo, Y. Y. (2016). Automated droplet manipulation using closed-loop axisymmetric drop shape analysis. *Langmuir*, *32*(19), 4820-4826. (*co-first authors)

Papers in preparation:

1. **Yu, K.,** Yang, J., and Zuo, Y. Y., Arbitrary waveform generation through oscillating droplet. To be submitted to *Applied Physics Letters*.

2. Yang, J., **Yu, K.,** Tsuji, T., Jha, R., and Zuo, Y. Y., Surface dilational rheology measured by a droplet waveform generator. To be submitted to *ACS Applied Materials and Interfaces*.

3. Xu, L., Bosiljevac G, **Yu K.,** and Zuo, Y. Y., Melting of Dipalmitoylphosphatidylcholine Monolayers. To be submitted to *Langmuir.*

References

1. del Rıo, O.; Neumann, A. W., Axisymmetric drop shape analysis: computational methods for the measurement of interfacial properties from the shape and dimensions of pendant and sessile drops. *Journal of colloid and interface science* **1997,** *196* (2), 136-147.

2. Valle, R. P.; Wu, T.; Zuo, Y. Y., Biophysical Influence of Airborne Carbon Nanomaterials on Natural Pulmonary Surfactant. *ACS Nano* **2015,** *9* (5), 5413-5421.

3. Roberts, G., *Langmuir-Blodgett Films*. Springer: 1990.

4. Rotenberg, Y.; Boruvka, L.; Neumann, A., Determination of surface tension and contact angle from the shapes of axisymmetric fluid interfaces. *Journal of colloid and interface science* **1983,** *93* (1), 169-183.

5. Saad, S. M.; Neumann, A. W., Axisymmetric Drop Shape Analysis (ADSA): An Outline. *Adv Colloid Interface Sci* **2016,** *238*, 62-87.

6. He, Q.; Zhang, Y.; Lu, G.; Miller, R.; Mohwald, H.; Li, J., Dynamic adsorption and characterization of phospholipid and mixed phospholipid/protein layers at liquid/liquid interfaces. *Adv Colloid Interface Sci* **2008,** *140* (2), 67-76.

7. Cabrerizo-Vilchez, M. A.; Wege, H. A.; Holgado-Terriza, J. A.; Neumann, A. W., Axisymmetric drop shape analysis as penetration Langmuir balance. *Review of Scientific Instruments* **1999,** *70* (5), 2438-2444.

8. Russev, S. C.; Alexandrov, N.; Marinova, K. G.; Danov, K. D.; Denkov, N. D.; Lyutov, L.; Vulchev, V.; Bilke-Krause, C., Instrument and methods for surface dilatational rheology measurements. *The Review of scientific instruments* **2008,** *79* (10), 104102.

9. Teh, S.-Y.; Lin, R.; Hung, L.-H.; Lee, A. P., Droplet microfluidics. *Lab on a Chip* **2008,** *8* (2), 198-220.

10. Neumann, A. W.; David, R.; Zuo, Y., *Applied surface thermodynamics*. CRC press: 2010; Vol. 151.

11. Valle, R. P.; Wu, T.; Zuo, Y. Y., Biophysical influence of airborne carbon nanomaterials on natural pulmonary surfactant. *ACS Nano* **2015,** *9* (5), 5413-21.

12. Baratian, D.; Cavalli, A.; van den Ende, D.; Mugele, F., On the shape of a droplet in a wedge: new insight from electrowetting. *Soft matter* **2015,** *11* (39), 7717-7721.

13. Gong, J.; Kim, C.-J., All-electronic droplet generation on-chip with real-time feedback control for EWOD digital microfluidics. *Lab on a Chip* **2008,** *8* (6), 898-906.

14. Miller, E.; Rotea, M.; Rothstein, J. P., Microfluidic device incorporating closed loop feedback control for uniform and tunable production of micro-droplets. *Lab on a Chip* **2010,** *10* (10), 1293-1301.

15. Wege, H. A.; Holgado-Terriza, J. A.; Cabrerizo-Vilchez, M. A., Development of a constant surface pressure penetration langmuir balance based on axisymmetric drop shape analysis. *J Colloid Interface Sci* **2002,** *249* (2), 263-73.

16. Horch, A. e. a., Assessment of the sampling rate in control systems. *Control Engineering Practice* **2001,** *Volume 9* (Issue 5).

17. Yu, K.; Yang, J.; Zuo, Y. Y., Automated droplet manipulation using closed-loop axisymmetric drop shape analysis. *Langmuir* **2016,** *32* (19), 4820-4826.

18. Zhang, H.; Fan, Q.; Wang, Y. E.; Neal, C. R.; Zuo, Y. Y., Comparative study of clinical pulmonary surfactants using atomic force microscopy. *Biochim Biophys Acta* **2011,** *1808*, 1832-1842.

19. Zhang, H.; Wang, Y. E.; Fan, Q.; Zuo, Y. Y., On the low surface tension of lung surfactant. *Langmuir* **2011,** *27* (13), 8351-8358.

20. Valle, R. P.; Huang, C. L.; Loo, J. S. C.; Zuo, Y. Y., Increasing Hydrophobicity of Nanoparticles Intensifies Lung Surfactant Film Inhibition and Particle Retention. *ACS Sustainable Chemistry & Engineering* **2014,** *2* (7), 1574-1580.

21. Dagan, M. P.; Hall, S. B., The Equilibrium Spreading Tension of Pulmonary Surfactant. *Langmuir* **2015,** *31* (48), 13063-7.

22. Jasper, J. J., The surface tension of pure liquid compounds. *J. Phys. Chem. Ref. Data* **1972,** *1* (4), 841-1009.

23. Phillips, C. L.; Nagle, H. T.; Chakrabortty, A., *Digital control system analysis & design, global edition*. Pearson Education: 2014.

24. Saad, S. M.; Neumann, A. W., Total Gaussian curvature, drop shapes and the range of applicability of drop shape techniques. *Adv Colloid Interface Sci* **2014,** *204*, 1-14.

25. Berry, J. D.; Neeson, M. J.; Dagastine, R. R.; Chan, D. Y. C.; Tabor, R. F., Measurement of surface and interfacial tension using pendant drop tensiometry. *Journal of Colloid and Interface Science* **2015,** *454*, 226-237.

26. Miller, R.; Fainerman, V. B.; Makievski, A. V.; Kragel, J.; Grigoriev, D. O.; Kazakov, V. N.; Sinyachenko, O. V., Dynamics of protein and mixed protein/surfactant adsorption layers at the water/fluid interface. *Adv Colloid Interface Sci* **2000,** *86* (1-2), 39-82.

27. Mitropoulos, V.; Mütze, A.; Fischer, P., Mechanical properties of protein adsorption layers at the air/water and oil/water interface: A comparison in light of the thermodynamical stability of proteins. *Advances in Colloid and Interface Science* **2014,** *206*, 195-206.

28. Tankovsky, N.; Zografov, N.; Andreeva, A., Gas-adsorption dynamics at the water–air interface, revealed by resonant droplet tensiometry. *Chemical Engineering Science* **2016,** *144*, 283-287.

29. Bonaccurso, E.; Butt, H. J., Microdrops on atomic force microscope cantilevers: evaporation of water and spring constant calibration. *The journal of physical chemistry. B* **2005,** *109* (1), 253-63.

30. Birdi, K. S.; Vu, D. T.; Winter, A., A study of the evaporation rates of small water drops placed on a solid surface. *The Journal of Physical Chemistry* **1989,** *93* (9), 3702-3703.

31. Shanahan, M. E. R. B., C., Effects of evaporation on contact angles on polymer surfaces. *International Journal of Adhesion and Adhesives* **1994,** *14* (3), 201-205.

32. Hu, H.; Larson, R. G., Evaporation of a Sessile Droplet on a Substrate. *The Journal of Physical Chemistry B* **2002,** *106* (6), 1334-1344.

33. Bachofen, H.; Schurch, S.; Urbinelli, M.; Weibel, E. R., Relations among alveolar surface tension, surface area, volume, and recoil pressure. *J. Appl. Physiol.* **1987,** *62* (5), 1878-1887.

34. Bachofen, H.; Schürch, S., Alveolar surface forces and lung architecture. *Comparative Biochemistry and Physiology - A Molecular and Integrative Physiology* **2001,** *129* (1), 183-193.

35. Kharge, A. B.; Wu, Y.; Perlman, C. E., Surface tension in situ in flooded alveolus unaltered by albumin. *Journal of applied physiology* **2014,** *117* (5), 440-451.

36. Piknova, B.; Schram, V.; Hall, S. B., Pulmonary surfactant: phase behavior and function. *Current opinion in structural biology* **2002,** *12* (4), 487-94.

37. Possmayer, F.; Hall, S. B.; Haller, T.; Petersen, N. O.; Zuo, Y. Y.; Bernardino de la Serna, J.; Postle, A. D.; Veldhuizen, R. A. W.; Orgeig, S., Recent advances in alveolar biology: Some new looks at the alveolar interface. *Respiratory Physiology & Neurobiology* **2010,** *173* (Supplement 1), S55-S64.

38. Rugonyi, S.; Biswas, S. C.; Hall, S. B., The biophysical function of pulmonary surfactant. *Respir Physiol Neurobiol* **2008,** *163* (1-3), 244-55.

39. Zuo, Y. Y.; Veldhuizen, R. A.; Neumann, A. W.; Petersen, N. O.; Possmayer, F., Current perspectives in pulmonary surfactant--inhibition, enhancement and evaluation. *Biochim Biophys Acta* **2008,** *1778* (10), 1947-77.

40. Yan, W.; Biswas, S. C.; Laderas, T. G.; Hall, S. B., The melting of pulmonary surfactant monolayers. *J Appl Physiol* **2007,** *102* (5), 1739-45.

41. Saad, S. M.; Policova, Z.; Acosta, E. J.; Hair, M. L.; Neumann, A. W., Mixed DPPC/DPPG monolayers at very high film compression. *Langmuir* **2009,** *25* (18), 10907-12.

42. Kaganer, V. M.; Mohwald, H.; Dutta, P., Structure and phase transitions in Langmuir monolayers. *Rev Mod Phys* **1999,** *71* (3), 779-819.

43. Keating, E.; Zuo, Y. Y.; Tadayyon, S. M.; Petersen, N. O.; Possmayer, F.; Veldhuizen, R. A., A modified squeeze-out mechanism for generating high surface pressures with pulmonary surfactant. *Biochim Biophys Acta* **2012,** *1818* (5), 1225-34.

44. McConlogue, C. W.; Vanderlick, T. K., A close look at domain formation in DPPC monolayers. *Langmuir* **1997,** *13* (26), 7158-7164.

45. Haydon, D. A., An investigation of droplet oscillation during mass transfer I. The conditions necessary, and the source of the energy for the oscillations. *Proceedings of the Royal Society of London. Series A. Mathematical and Physical Sciences* **1958,** *243* (1235), 483-491.

46. Mugele, F.; Baret, J.-C.; Steinhauser, D., Microfluidic mixing through electrowetting-induced droplet oscillations. *Applied Physics Letters* **2006,** *88* (20), 204106.

47. Yu, L. M.; Lu, J. J.; Chan, Y. W.; Ng, A.; Zhang, L.; Hoorfar, M.; Policova, Z.; Grundke, K.; Neumann, A. W., Constrained sessile drop as a new configuration to measure low surface tension in lung surfactant systems. *Journal of applied physiology* **2004,** *97* (2), 704-15.

48. Miller, R.; Liggieri, L., *Interfacial rheology*. CRC Press: 2009; Vol. 1.

49. Neumann, A. W.; David, R.; Zuo, Y., *Applied Surface Thermodynamics, Second Edition*. Taylor & Francis: 2012; Vol. surfactant science series.

50. Ravera, F.; Loglio, G.; Kovalchuk, V. I., Interfacial dilational rheology by oscillating bubble/drop methods. *Current Opinion in Colloid & Interface Science* **2010,** *15* (4), 217-228.

51. Egry, I., Surface tension measurements of liquid metals by the oscillating drop technique. *Journal of Materials Science* **1991,** *26* (11), 2997-3003.

52. Milne, A. J. B.; Defez, B.; Cabrerizo-Vílchez, M.; Amirfazli, A., Understanding (sessile/constrained) bubble and drop oscillations. *Advances in Colloid and Interface Science* **2014,** *203* (Supplement C), 22-36.

53. Leser, M. E.; Acquistapace, S.; Cagna, A.; Makievski, A. V.; Miller, R., Limits of oscillation frequencies in drop and bubble shape tensiometry. *Colloids and Surfaces A: Physicochemical and Engineering Aspects* **2005,** *261* (1-3), 25-28.

54. Dukhin, S. K., G.; Miller, R., *Dynamics of adsorption at liquid interfaces*. Elsevier: 1995; Vol. 1.

55. Berg, J. C., *An Introduction to Interfaces and Colloids: The Bridge to Nanoscience*. World Scientific: Singapore, 2010.

56. Miller, R.; Ferri, J. K.; Javadi, A.; Krägel, J.; Mucic, N.; Wüstneck, R., Rheology of interfacial layers. *Colloid and Polymer Science* **2010,** *288* (9), 937-950.

57. Lucassen, J.; Van Den Tempel, M., Dynamic measurements of dilational properties of a liquid interface. *Chemical Engineering Science* **1972,** *27* (6), 1283-1291.

58. Benjamins, J.; Lucassen-Reynders, E., Surface dilational rheology of proteins adsorbed at air/water and oil/water interfaces. *Studies in Interface Science* **1998,** *7*, 341-384.

59. Loglio, G.; Pandolfini, P.; Miller, R.; Makievski, A.; Ravera, F.; Ferrari, M.; Liggieri, L., Drop and Bubble Shape Analysis As a Tool for Dilational Rheological Studies of Interfacial Layers. *Studies in Interface Science; Möbius, D.; Miller, R., Eds*, 439-483.

60. Stubenrauch, C.; Miller, R., Stability of foam films and surface rheology: an oscillating bubble study at low frequencies. *The Journal of Physical Chemistry B* **2004,** *108* (20), 6412-6421.

61. Kotsmar, C.; Kragel, J.; Kovalchuk, V. I.; Aksenenko, E. V.; Fainerman, V. B.; Miller, R., Dilation and shear rheology of mixed β-casein/surfactant adsorption layers. *The Journal of Physical Chemistry B* **2008,** *113* (1), 103-113.

62. Noskov, B. A.; Akentiev, A. V.; Bilibin, A. Y.; Zorin, I. M.; Miller, R., Dilational surface viscoelasticity of polymer solutions. *Advances in Colloid and Interface Science* **2003,** *104* (1), 245-271.

63. Kovalchuk, V. I.; Krägel, J.; Makievski, A. V.; Ravera, F.; Liggieri, L.; Loglio, G.; Fainerman, V. B.; Miller, R., Rheological surface properties of C12DMPO solution as obtained from amplitude- and phase-frequency characteristics of an oscillating bubble system. *Journal of Colloid and Interface Science* **2004,** *280* (2), 498-505.

64. Wantke, K.-D.; Fruhner, H., Determination of surface dilational viscosity using the oscillating bubble method. *Journal of colloid and interface science* **2001,** *237* (2), 185-199.

65. Russev, S. C.; Alexandrov, N.; Marinova, K. G.; Danov, K. D.; Denkov, N. D.; Lyutov, L.; Vulchev, V.; Bilke-Krause, C., Instrument and methods for surface dilatational rheology measurements. *Review of scientific instruments* **2008,** *79* (10), 104102.

66. Ivanov, I. B.; Danov, K. D.; Ananthapadmanabhan, K. P.; Lips, A., Interfacial rheology of adsorbed layers with surface reaction: on the origin of the dilatational surface viscosity. *Advances in colloid and interface science* **2005,** *114*, 61-92.

DROPLET MANIPULATION WITH FEEDBACK CONTROL

A THESIS SUBMITTED TO THE GRADUATE DIVISION OF THE UNIVERSITY OF HAWAIʻI AT MĀNOA IN PARTIAL FULFILLMENT OF THE REQUIREMENTS FOR THE DEGREE OF

MASTER OF SCIENCE
IN
MECHANICAL ENGINEERING

DECEMBER 2017

Kyle Yu

Thesis Committee:
Yi Zuo, PhD
John S. Allen, PhD
Weilin Qu, PhD

Acknowledgements

I thank the University of Hawaii, where I conducted research, practiced engineering, and fostered relationships.

I thank Dr. Yi Zuo for participation, assistance, and advice in content presented in this thesis.

I thank Dr. John S. Allen, Dr. Weilin Qu, and Dr. Yi Zuo for participation and evaluation in the thesis committee.

I thank Jerry Yang and Dayne Sasaki for cooperation and assistance, on a professional and personal basis.

I thank friends and family for support during my time at the University of Hawaii.

I acknowledge financial support from NSF under the grant number CBET-1254795.

I am grateful to you all.

Abstract

Droplet manipulation has an important role in a wide range of scientific and industrial applications, such as thin film, soft matter, microfluidics, biophysical simulations, interfacial reactions, and interfacial rheology. We developed a feedback-controlled closed-loop axisymmetric drop shape analysis (CL-ADSA) to manipulate millimeter-sized droplets, based on the experimental methodology constrained drop surfactometer (CDS). With CL-ADSA, we extended the CDS from a surface tension measurement tool to a sophisticated droplet manipulation instrument. We demonstrated the usefulness of this methodology in three practical applications, control of droplet volume by automatically compensating natural evaporation, precise control of surface area variations for high-fidelity biophysical simulations of natural pulmonary surfactant, and steady control of surface pressure for *in situ* Langmuir-Blodgett transfer from droplets. Furthermore, we developed an arbitrary waveform generator for controlled oscillation of a droplet/bubble. We demonstrated this methodology in three ways. First, we demonstrated arbitrary waveform generation by controlling the volume and surface area of a water droplet to sine, triangle, square, and sawtooth waveforms. Second, we evaluated the accuracy of the arbitrary waveform generation through a coefficient of determination analysis. Third, we apply arbitrary waveform generation to study the interfacial dilational rheology of adsorbed surfactant films. Our studies suggest the feedback control system developed in this thesis hold great promise for advancing droplet manipulation in a variety of material and surface science applications, such as thin-film fabrication, self-assembly, and biophysical study of pulmonary surfactants.

Table of Contents

List of Figures

List of Tables

List of Abbreviations

V	Volume
A	Surface Area
γ	Surface Tension
π	Surface Pressure
θ	Contact Angle
κ	Compressibility
ADSA	Axisymmetric Drop Shape Analysis
AFM	Atomic Force Microscopy
CDS	Constrained Drop Surfactometer
PD	Pendant Drop
SD	Sessile Drop
PB	Pendant Bubble
SB	Sessile Bubble
G	Gravitational Acceleration
E_0	Limiting Elasticity
Er	Elastic Modulus
Ei	Viscous Modulus
$\|E\|$	Total Modulus
FPS	Frames Per Second
SD	Standard Deviation
FEM	Finite Element Method
RAM	Random-Access Memory
.DAT	Data File Format
PI	Proportional Integral
PD	Proportional Derivative
PID	Proportional Integral Derivative
C_{12}DMPO	Dodecyldimethylphosphine Oxide
DPPC	Dipalmitoyl Phosphatidylcholine
DOPC	1,2-Dioleoyl-Sn-Glycero-3-Phosphocholine
PL	Phospholipids

Chapter 1. Introduction

1.1 Introduction

Surface science is the study of physical and chemical properties between interfacial interfaces, for example, air and water, oil and water, or metal and water. Surface science is an interdisciplinary study and has many scientific and industrial applications, namely adhesives, coatings, pharmaceuticals, sprays, and semiconductors. A fluid surface can be broadly described by its surface tension, a cohesive phenomenon of the surface of fluids defined as the force per unit length. This phenomenon is observed in a liquid's ability to maintain droplets; a droplet with a higher surface tension will maintain a more spherical profile and vice versa.

Surface tension and other characterizing properties can be measured using a computational technique known as Axisymmetric Drop Shape Analysis (ADSA). In equilibrium, a fluid droplet is shaped by gravity and its own surface tension.[1] By inversely solving the Laplacian equation which the drop shape can be modeled upon, it is possible to calculate a surface tension from an image.[1] ADSA, developed by Del Rio et al, computerizes this process to seconds on a modern computer.[1] The experimental apparatus for ADSA based experiments are surface tensiometers. For the purpose of this thesis, the tensiometer is known as the Constrained Drop Surfactometer (CDS).[2] Through ADSA and the CDS, the Laboratory of Biocolloids and Biointerfaces at the University of Hawaii study a number of surface phenomena, namely interactions involving self-assembled monolayers, pulmonary surfactants, and toxicology of nanomaterials.

1.2 Surfaces and Surface Tension

A critical concept in the study surface science is surface tension, a cohesive phenomenon of the surface of fluids. In general, there are five types of interfaces, liquid-gas, liquid-liquid, liquid-solid, solid-gas, and solid-solid.

Distance between liquid molecules is significantly less than distance in gas molecules, henceforth, gas molecules produce significantly less attraction. At a liquid-gas interface, a molecule is more attracted more by liquid than gas. Thus, the interface will minimize its surface area, resulting in a phenomenon known as surface tension. For liquid-gas interfaces, this phenomenon is commonly observed in a liquid's ability to maintain droplets; a droplet with a high surface tension will maintain a more spherical profile, vice versa, a droplet with a low surface tension a less spherical profile. Surface tension, represented by the Greek symbol Gamma "γ", is defined as force per unit length, often as mN/m.

Surface tension can be altered by surfactants. The term surfactant is an abbreviation for surface active agent. Surfactants are amphipathic molecules containing both hydrophilic and hydrophobic components. At water-air interfaces, the hydrophilic head sits in water, while the hydrophobic tails points into air. This amphipathic structure gives surfactant molecules a relocation preference for the interface. Surfactants form a single layer of molecules at the interface, called a monolayer, which is shortened for "monomolecular film".[3] Intermolecular forces between surfactant molecules and liquid molecules are weaker than intermolecular forces between liquid molecules alike. Thus, surfactant molecules at water-air interfaces decreases surface tension.

There are many types of surfactants, namely laundry detergents, foaming agents, and lung surfactant. In mammalian lungs, a part of required work is from expanding the alveoli against surface tension; and lung surfactant reduces this work by reducing the surface tension around the alveoli. Lung surfactant, by weight, is approximately 90% lipids and 10% proteins. The lipids consist of phospholipids (PLs, 90–95 wt.%) with a small amount of neutral lipids (5–10 wt.%).

Surface tension can be measured using a number of techniques known as drop shape analysis. In equilibrium, a fluid droplet or bubble is shaped by gravity and its own surface tension; moreover, this phenomenon can be modeled by the Laplace equation of capillarity[1]. As such, by inversely solving the Laplace equation, it is possible to calculate the surface tension from an image of a drop or bubble.[1]

1.3 Constrained Drop Surfactometer

The Constrained Drop Surfactometer (CDS) is a surface tensiometer developed by the Laboratory of Biocolloids and Biointerfaces at the University of Hawaii. The CDS consists of an image acquisition component, an environmental control component, and a liquid flow component. **Figure 1.1** demonstrates a schematic of the CDS. **Figure 1.2** demonstrates a photo of the CDS.

The image acquisition component consists of a camera (Model PLB-771U, PixeLink), a droplet, a light source (Model NT62-817, Edmund Optics). When these three are aligned, a high contrast silhouette of the droplet reaches the camera sensor. The camera acquires images

between 0 to 30 frames per second (FPS). The backlight and diffusing lens provides parallel backlight for illumination.

The liquid flow component manipulates fluid flow to the droplet for formation and deformation. This component consists of a motor driver (1002C, Gastight, Hamilton), a servomotor (Model LTA-HS, Newport), a syringe (1002C, Gastight, Hamilton), and a droplet, which form a motor-piston-syringe. Motor displacement manipulates the liquid flow, and hence the droplet volume.

The environmental control component maintains temperature and humidity for the droplet. This component consists of a thermoelectric plate (Model CP-61, TE Technology) and a machined environmental chamber. The thermoelectric plate provides heating or cooling to the environmental chamber. The environmental chamber has glass windows to pass light. Upon simulating physiological conditions, air in the environmental chamber is maintained at 37 ºC and is saturated with water vapor.

Over the course of an experiment, the environmental conditions are maintained, the volume of a droplet is manipulated by the liquid flow component; in parallel, a series of droplet images may be captured. After an experiment, droplet images are sent to the computer for ADSA calculations.

1.4 Axisymmetric Drop Shape Analysis

Drop shape analysis can determine surface tensions between liquid-gas or liquid-liquid interfaces of sessile drops (SD), sessile bubbles (SB), pendant drops (PD), and pendant bubbles (PB). The shape of droplet is determined by gravitational forces, which deforms the droplet (i.e.,

elongating PD and PB and flattening SD and SB), and surface tension forces, which rounds droplet. The force between gravity and surface tension can be modeled by the Laplace equation of capillarity:[1]

$$\gamma\left(\frac{1}{R_1}+\frac{1}{R_2}\right)=\Delta\rho g z+\frac{2\gamma}{R_0} \qquad \text{(Eq. 1.1)}$$

where R_1 and R_2 are the two principal radii of curvature, $\Delta\rho$ is the density difference between the interface, z is the height of the droplet normal from the reference plane, R_0 is the radii at the apex of the droplet. Therefore, given γ and other parameters above, the shape of droplet may be determined, vice versa, it is possible to determine the surface tension from a given drop shape profile.

It is timely to solve the surface tension from the droplet profile analytically. Among numerical solutions, Axisymmetric Drop Shape Analysis-Profile (ADSA-P), developed by Neumann et al, is amongst the most powerful due to its efficiency, accuracy, and flexibility.[1, 4] ADSA-P computerizes the numerical solution and reduces timely manual calculation to seconds on a modern computer.

Axisymmetric Drop Shape Analysis (ADSA) performs calculations on imported droplet images. Firstly, the image is processed through an edge detection routine. This generates a number of pixels, typically around 1000, along the shape of the droplet, to produce a 2D array of the edge pixel coordinates, known as the experimental profile. Moreover, the unit of the experimental profile are pixel coordinates and these coordinates needs to be distance coordinates. This scale factor is constant for every experimental setup. Given physical constraints such as density and gravity, a series of ideal Laplacian curve profiles, known as theoretical profiles, are

generated through the Bashforth-Adams equation (Eq. 1.1), where axisymmetric interfaces can be expressed as a function of the arc length *s*:

$$\frac{d\theta}{ds} = \frac{2}{R_0} + \frac{\Delta\rho g}{\gamma} z - \frac{\sin\theta}{x} \quad \text{(Eq. 1.2)}$$

$$\frac{dx}{ds} = \cos\theta \quad \text{(Eq. 1.3)}$$

$$\frac{dz}{ds} = \sin\theta \quad \text{(Eq. 1.4)}$$

$$\frac{dV}{ds} = \pi x^2 \sin\theta \quad \text{(Eq. 1.5)}$$

$$\frac{dA}{ds} = 2\pi x \quad \text{(Eq. 1.6)}$$

$$x(0) = 0, z(0) = 0, \theta(0) = 0, V(0) = 0, A(0) = 0 \quad \text{(Eq. 1.7)}$$

where θ is the tangential angle, *x* is the radius, and *z* is the height, R_0 is the curvature at the origin, $\Delta\rho g / \gamma$ is the capillary constant, A is surface area, and V is droplet volume[1]. Third, a numerical fitting scheme fits and selects the theoretical drop profiles to the experimental profile, thereby outputting corresponding properties of the drop/bubble, such as droplet volume, surface area, and surface tension. The theoretical profile that best fits the experimental profile is selected. The theoretical profile is exported along with its droplet volume, surface area, surface tension, and contact angle.

The Graphical User Interface (GUI) of ADSA was developed with Microsoft Visual Studios as a Multiple Document Interface program, allowing for multiple child windows to reside under one main window. A powerful function of ADSA GUI is the analysis of a run of images, which are droplet images with identical physical constraints. This allowed the automatic calculation of an entire set of images from an experiment. However, this function is confined to the precondition that the images must be prepared prior to analysis.

1.4.1 Edge Detection

Image files of the droplet/bubble are acquired through a machine vision camera (Model PLB-771U, PixeLink). A parallel backlight illuminates the droplet/bubble. Image files are stored as 8-bit grayscale uncompressed .tiff files, with a max resolution of 1280×1024. Generally, Canny edge detection is used for edge detection in droplet/bubble.[5] First, a Gaussian blur is applied to reduce noise. Second, differentiation in x and y directions produce gradient vectors. Third, non-maximum suppression suppresses a gradient upon a larger gradient neighbor, in x and y directions, removing a number of pixels. Fourth, hysteresis thresholding selects gradient vectors above a high threshold as an edge pixel, and removes gradient vectors below a low threshold. Remaining gradients are selected upon the condition of neighboring a previously selected pixel.

1.4.2 Numerical Fitting

The numerical scheme, introduced by Rotenberge et al.[4], is used to find the theoretical curve that best fit the experimental profile. The strategy is to minimize an objective function E, the sum of weighted squared normal distances, e_i, between all coordinates of experimental profile and theoretical profiles:

$$e_i = \frac{1}{2} d_i^2 = \frac{1}{2}[(x_i - X_i)^2 + (z_i - Z_i)^2] \quad \text{(Eq. 1.8)}$$

$$\min E(a) = \sum_{i=1}^{N} w_i e_i\,(a) \quad \text{(Eq. 1.9)}$$

where w_i is the weighting factor of the i^{th} point, (X_i, Z_i) are experimental coordinates and (x_i, z_i) are the corresponding Laplacian coordinates closest to (X_i, Z_i), a is a set of optimizing parameters $a = [x_0 \;\; z_0 \;\; b \;\; c]$, where (x_0, z_0) is the coordinate of the apex, and b is the curvature of the apex, and c is the capillary constant $\Delta\rho g / \gamma$. This becomes a multidimensional nonlinear

least-square problem, which requires an iterative Newton-Raphson or Levenberg-Marquardt optimization procedure.[1] Once the minimum is found, the optimization parameters determine the theoretical profile that best fit the experimental profile, and surface tension and other properties are computed.

1.5 Control Systems Overview

Control systems commands and regulates systems through control loops. In continuous control, feedback loops can automatically control a process or operation. Feedback control systems compares the controlled variable's value or status with the desired value, and thereby apply a control signal to change the controlled variable's value or status to the same value as the desired value.

Traditionally, ADSA and CDS based experiments are limited to the measurement of droplet, while control of droplet remains mostly a manual procedure. Automatic control of droplet volume, surface area, and surface tension reduces significant manual work and can open up new areas of study entirely. A controller system is to be integrated on the existing system. Here, the plant, which is the process and the actuator, is the constrained Drop Surfactometer (CDS). The measurement, which is the required feedback, is the Axisymmetric Drop Shape Analysis (ADSA). Upon the completion of feedback control, arbitrary waveform generation is to be explored.

Prerequisites for feedback control, control design specifications, are control model are prepared prior to the implementation of feedback control. Common control algorithms are Bang–bang control, Proportional control, Proportional Integral (PI) control, Proportional Derivative

(PD) control, and Proportional Integral Derivative (PID) control, and fuzzy control. The implementation is compared and discussed. Adaptive control, which adapts to the control system, will also be discussed. Feedback control applications including but not limited to evaporation compensation, physiological simulations, and surface rheology will be explored and discussed.

1.6 Thesis Outline

This thesis communicates the development process of feedback control for droplet manipulation. The feedback control will be based on the existing plant, the constrained Drop Surfactometer (CDS), and the existing measurement, Axisymmetric Drop Shape Analysis (ADSA). The development of feedback control system is through software and hardware interfacing, with C based computer languages.

This thesis is suitable for readers with a basic understanding of physics, chemistry, engineering, and information technology. Other technical content will be explained where applicable. This thesis states the background of drop shape analysis, image processing, physiological simulations, and surface thermodynamics, but does not elaborate upon these. This thesis demonstrates feedback control for four drop/bubble configurations: sessile drop, sessile bubble, pendant drop, and pendant bubble, but will focus on the sessile drop. This thesis discusses the conception and validation of the implemented control system, but does not discuss the details of C and C++ implementation. The computer interfaces with experimental hardware through serial and parallel communication. There exist device drivers for various experimental hardware, however, significant infrastructure was developed to readily communicate with the

aforementioned hardware, and this thesis does not discuss the structure, algorithm, and parallelization of the implemented infrastructure.

Chapter 2 discusses feedback control. This includes a prerequisite for feedback control which is real-time measurement, control limitations, control equations and models, and applications and discussion. Chapter 3 discusses the extension of feedback control, arbitrary waveform generation. This includes control limitations, generated waveforms, and applications and discussion. Chapter 4 summarizes this thesis work and contributions thereof.

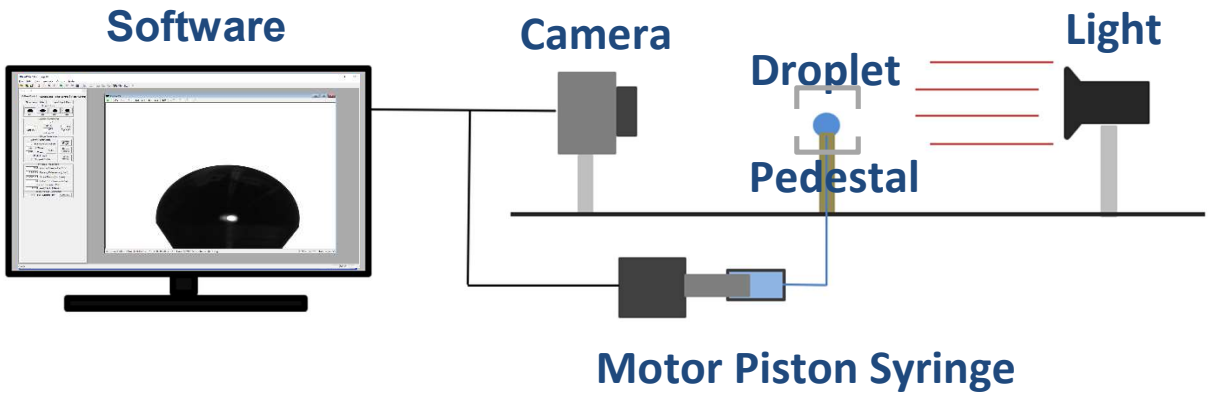

Figure 1.1 The Constrained Drop Surfactometer (CDS). A droplet is formed on a pedestal. The pedestal is connected to the motor-piston-syringe, pushing/pulling fluid, thereby resulting in formation and deformation. The light source on the left projects images of the droplet into the camera on the right. Images are then sent to ADSA for analysis. These three components are controlled independently by a computer.

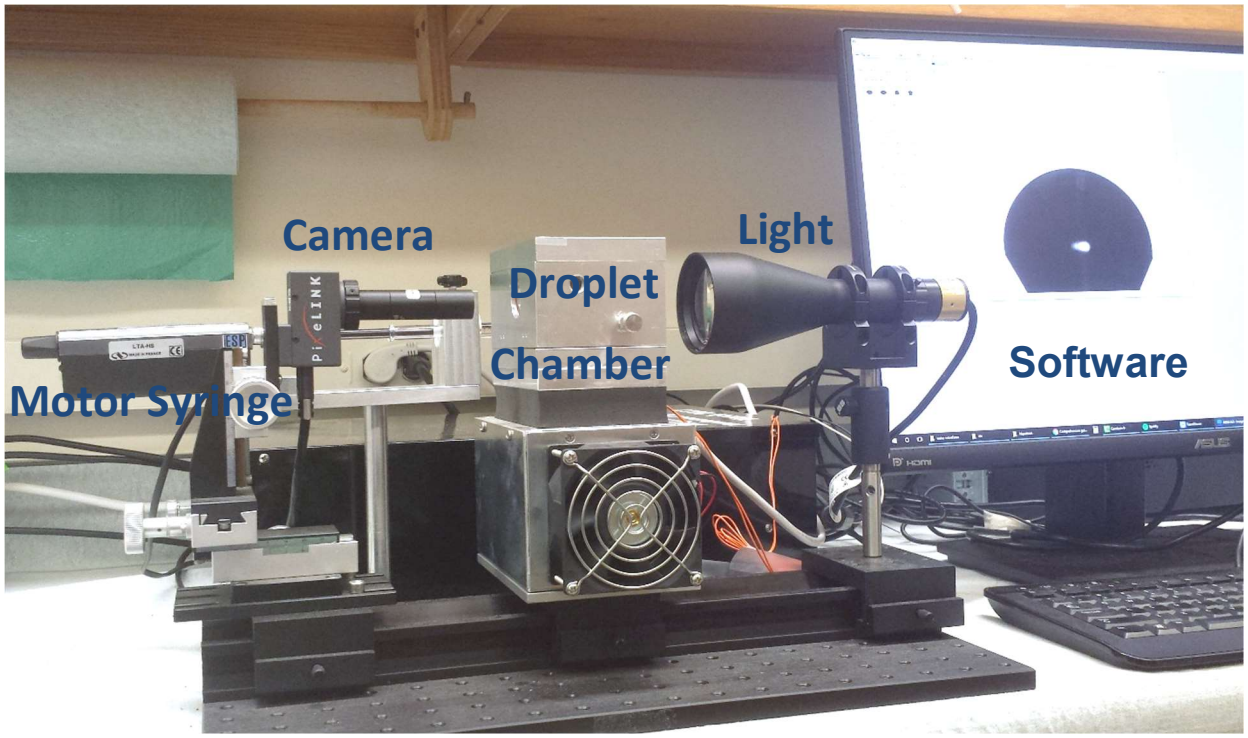

Figure 1.2 Photo of the experimental setup CDS. A droplet is formed on a pedestal. The CDS is composed of three parts, the camera and light for visualization, the motor-piston-syringe and pedestal for actuation, software for analysis. The droplet and pedestal is placed in an environmental chamber above a thermoelectric plate.

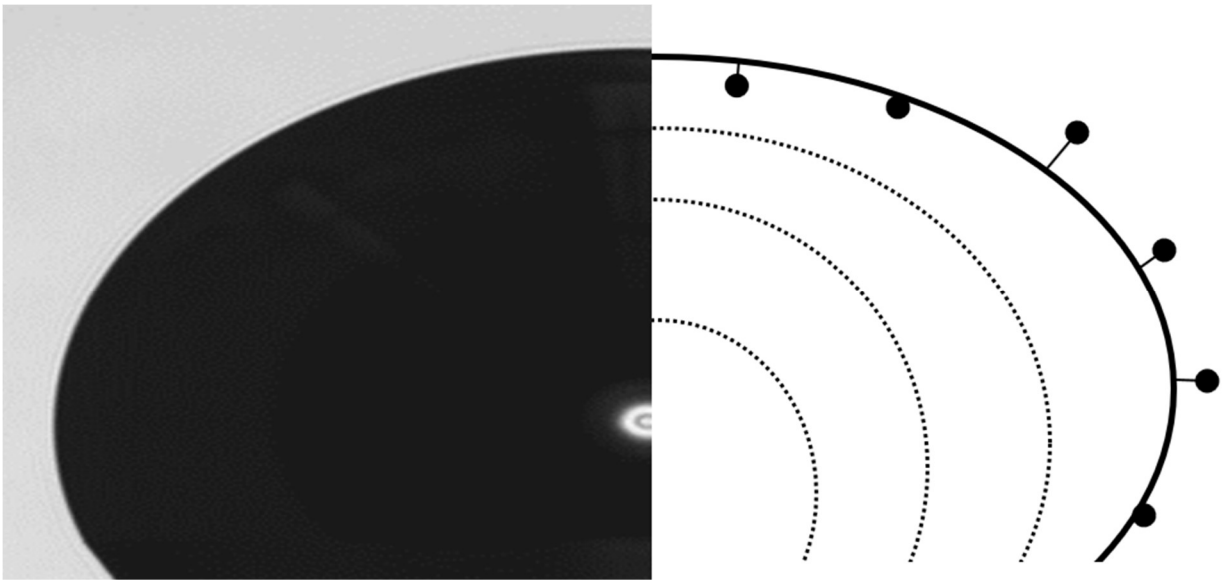

Figure 1.3 Procedure of ADSA on a sessile drop. First, ADSA opens an image file, this is shown on the left half of the image. Second, through edge detection, the edge or profile coordinates is extracted (large black dots). Third, a series of theoretical profiles (dashed black lines) are generated to match the detected profile (solid black line). Through the matched profile, surface properties, such as drop(s)/bubble volume, surface area, surface tension are obtained.

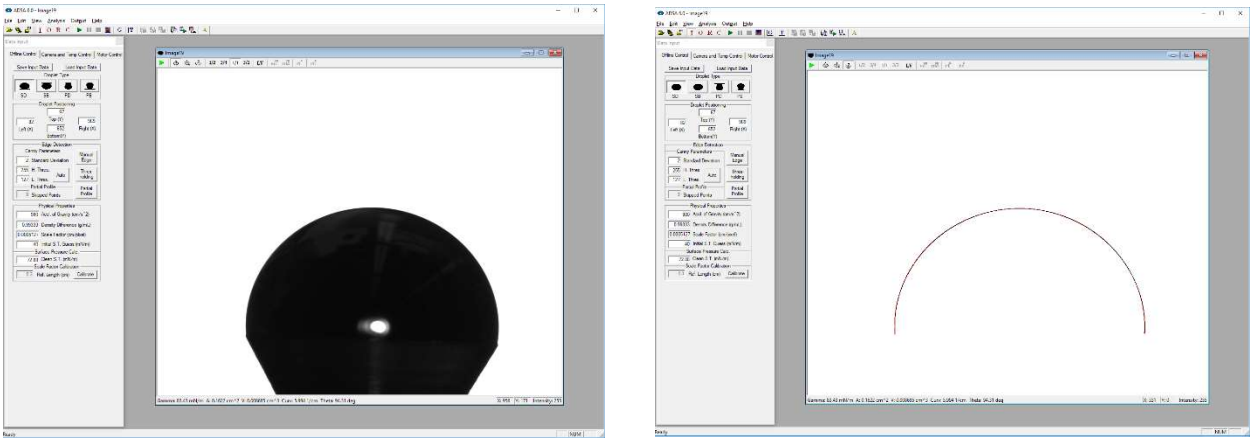

Figure 1.4 Sample screenshots of the ADSA GUI interface. The left screenshot shows the ADSA GUI with an original raw experimental image of a sessile bubble while the right screenshot shows the ADSA GUI with a processed edge profile of a sessile droplets.

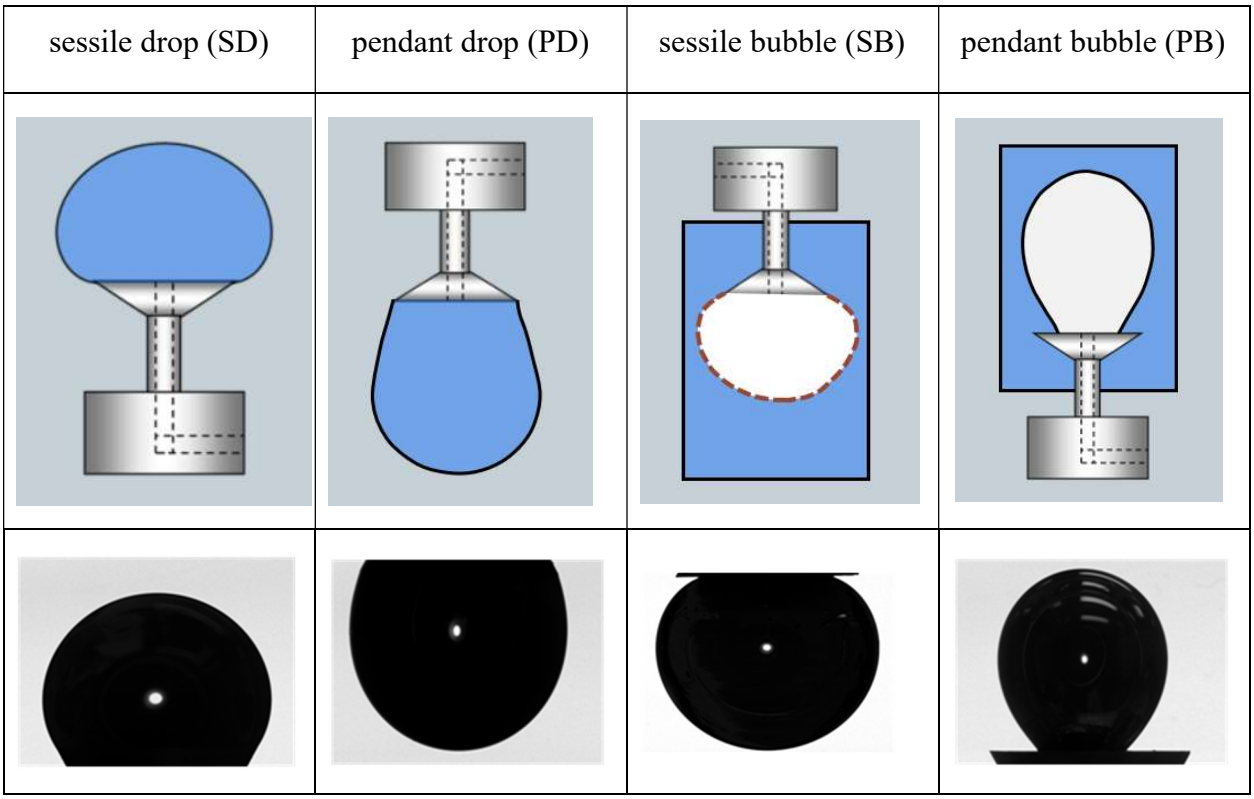

Figure 1.5 Four studied axisymmetric droplet/bubble configurations. These are the sessile drop (SD), pendant drop (PD), sessile bubble (SB), and pendant bubble (PB). The diagram is placed on top and the actual experimental images of formamide droplet/bubble are placed on the bottom. The coordinate system is defined through the polarities of the density difference ($\Delta\rho$) and the height of a point along the drop profile (z). $\Delta\rho$ is the density difference between the fluid inside the discrete droplet and the fluid outside the droplet. $\Delta\rho$ of PD and SD is positive and $\Delta\rho$ of SB and PB is negative. z coordinate is defined as positive for SD and PB and negative for SB and PD.

Chapter 2. Feedback Control Development

2.1 Introduction

Effective manipulation of liquid droplets plays an important role in a wide range of scientific and industrial applications, such as synthesis of thin-film materials,[6] control of interfacial reactions,[7] study of surface rheology,[8] and operation of digital microfluidics.[9] In these applications, droplets serve as a miniaturized platform that provides a number of unique advantages over traditional interfacial models such as the classical Langmuir trough.[10] First, the small volume of droplets facilitates study of scarce or expensive samples, such as biological or clinical fluids. Second, compared to bulk systems, droplets possess a much larger surface-area-to-volume ratio that makes droplets an ideal soft platform for studying surface reaction and interfacial assembly. Third, due to system miniaturization, it is feasible to ensure a rigorous environmental control, such as temperature and experimental atmosphere, with the droplet system, thus allowing for environmental studies across the droplet surfaces.[11]

Compared to the control of a flat surface as in the classical Langmuir trough, effective control and manipulation of a single droplet is not a trivial task. In general, the profile of a free-standing droplet is determined by the balance of gravitational and surface tension forces as predicted by the Bond number, $Bo = \frac{\Delta\rho g R^2}{\gamma}$, where $\Delta\rho$ is the density difference across the drop surface, g is the gravitational acceleration, R is the characteristic radius of the droplet, and γ is the surface tension. Droplets with very small Bond numbers, such as micron-sized droplets, are generally considered as spherical beads.[12] The key parameter for manipulating such droplets is their volume; while the surface area can be calculated by a spherical approximation and the

surface tension is routinely assumed to be a constant.[13] A number of techniques have been developed to manipulate the volume of micron-sized droplets.[12-14]

However, when the Bond number is sufficiently large, *e.g.,* for millimeter-sized droplets and/or at the presence of surfactants, the drop profile can be significantly deformed by gravity to assume a Laplacian shape.[10, 15] In these cases, the surface area of the droplet cannot be correlated with its volume using a simple spherical approximation. Meanwhile, the surface tension usually varies with the surface area at the presence of surfactants. Hence, all droplet properties, including its volume, surface area, and surface tension, need to be individually controlled for effective droplet manipulation. Nevertheless, in most applications, one can only control the drop volume using a high-precision syringe pump. Neither surface area nor surface tension of the droplet can be directly controlled with current techniques. Cabrerizo-Vilchez and coworkers have developed a fuzzy-logic algorithm to control the surface pressure or surface area of a pendant drop.[15] In spite of a suitable control method, the fuzzy-logic algorithm requires the definition of input and output fuzzy sets for every control process, which is not a trivial task.

In this chapter, we developed a novel feedback control method for manipulating millimeter-sized droplet based on axisymmetric drop shape analysis (ADSA). ADSA is a computer-based surface tension measurement methodology first developed by Neumann and coworkers.[1, 4] ADSA determines surface tension, surface area, and volume of a droplet by numerically fitting the experimental drop profile to theoretical profiles integrated with the numerical Laplace equation of capillarity. We have developed a high-speed ADSA algorithm capable of real-time analysis of droplet properties, including its volume, surface area, and surface tension. By coupling real-time ADSA with a proportional-integral-derivative (PID) controlled

motorized syringe, we have developed the first closed-loop ADSA that is capable of precisely controlling the volume, surface area, and surface tension of a millimeter-sized droplet.

2.2 Real-Time Analysis Development

ADSA is designed for analysis on existing droplet image files such that the images must be prepared in advance. This results in a timely and inefficient procedure to study surface phenomena and an obstacle for feedback control.

This procedure requires usage of multiple software. During an experiment, the operator first must prepare the droplet on the CDS for study. The droplet formation and deformation is through liquid flow from a motor-piston-syringe assembly. The motor in controlled by a **Newport SMC100 Motor Driver Software**. The operator next must capture images of the droplet. The camera is controlled by a **PixeLink camera driver**. After the experiment, the images are loaded into the **ADSA software** for analysis and output. After analysis, the resulting data file (.DAT) is plotted and visualized **OriginLab Origin Software.** This procedure is necessary for even the most basic experiments, and requires repetition for every successive experiment, leading to a timely process. **Figure 2.1** demonstrates this procedure.

Real time ADSA analysis can automate much of this procedure, and is a necessity for feedback control. There are several key operations to real time analysis. Firstly, ADSA must communicate with the camera firmware to retrieve images directly from the camera. Second, ADSA shall automatically perform analysis on retrieved images. Third, in parallel with the first two operations, ADSA must plot the analysis data for the operator to visualize. All of this shall

be automated and shall be performed simultaneously with the experiment. **Figure 2.2** demonstrates this procedure.

This automation increases efficiency significantly. For example, during dynamic cycling experiments, experiments involving cycles of rapid droplet size increase and decrease, several hours can be saved over the course of a day.

2.2.1 Camera Integration

There are two objectives for the camera communication. Upon selection, ADSA shall generates a live preview video from the camera. Upon additional selection, ADSA shall repeatedly retrieve image frames for analysis.

ADSA must first be able to communicate with the camera firmware. PixeLink provides C and C++ header files for additional software development. The ADSA visual studios project must integrate the camera class and function calls. An additional execution thread is necessary such that the preview video, analysis, and GUI all execute independently. In a multithreaded program, multiple sequence of programmed instructions executes concurrently, in this case, preventing video lag and freezing of the GUI. Also, another child frame class, a window residing in the main window of the ADSA program, was added and integrate in the visual studios project.

For real time analysis, ADSA retrieves an image frame as a 2D unsigned integer byte array (`uint8_t`), and dynamically allocates this structure to the random-access memory (RAM). The image array is then called directly by the ADSA class initiating image processing and analysis. In addition, an option to write the retrieved frame onto the hard disk was developed. This procedure increases speed by one frame write; testing showed this increased computational

time by roughly 150ms. An option to write the image file as TIFF or compressed to JPG was developed.

2.2.2 Plotting Integration

The plotting and visualization interface shall encompass basic plotting functions of Originlab origin. ADSA shall feed analyzed results into a plot window and shall plot the droplet's frame number, time, volume, surface area, surface tension, and contact angle.

In addition to camera development, an additional execution thread and an additional child frame class is necessary. The plot class shall receive results data from the analysis class, and shall manipulate data dynamically, with an option to export as a .DAT file.

The plot window involved existing plotting libraries or development anew. After elementary research and analysis on popular plotting libraries, it was concluded that libraries that mustered the most potential was MathGL, GNU Plot, PLplot, Microsoft Chart Control, and MiniPlot. These libraries share a same purpose, but are mutually exclusive in implementation. It is highly ineffective to implement multiple options, given time resources.

It is ideal to select a single implementation. Two decision matrices were employed, allowing for weighted and systematic identification and analysis of the local design criteria. Two decision matrices are constructed, one for benefit and one for time cost. The option with the highest ratio of benefit vs time shall be selected. The design factor's relative significance was based on its alignment to plotting specification and needs. **Table 1** and **Table 2** demonstrates this.

The implementation with the highest benefit vs cost ratio was to build anew. Building anew takes longer to start as foundation classes are missing, but no further integration and maintenance was required. Also, gaining experience with a math library is timely. Other libraries, notably MathGL and PLplot are more mathematical in design, which is not needed for this scope. Another factor that made building anew the most promising alternative was that it offered greater flexibility; the interface can later be adjusted with great ease. Moreover, **Figure 2.3** demonstrates a screenshot of the completed real-time analysis.

2.3 Closed-loop Feedback Control System

Six control algorithms of Bang–bang control, Proportional control, Proportional Integral (PI) control, Proportional Derivative (PD) control, and Proportional Integral Derivative (PID) control, and fuzzy control shall be implemented and integrated over real time analysis ADSA and the CDS. These six algorithms have strength and limitations with respect to each other, and each have suitable applications.

Open loop control is a control which does not feedback from ADSA. A predetermined command displacement is sent to the motor. Droplet control with the Newport SMC100 Motor Driver Software is open loop control. However, this type of control is processes no feedback control and is highly susceptible to system disturbances.

Bang–bang control sets the motor to two states of on and off. This controller actuates the motor when the droplet is outside a predefined command range, and switches the motor off when the droplet reaches within the command range. This is a continuous control process requiring

feedback control. Bang–bang control is straightforward and requires minimal processing. However, the motor speed is predefined thereby resulting in longer transient times.

Proportional control actuates the motor continuously to a value proportional to the error, which is the difference between the command state of the droplet and the measured state. This controller requires sampling from feedback control, and able to improve the transient time. However, proportional control may be prone to steady state errors, which occur when the current state of the droplet is close to the command state, and the proportional motor actuation is unable to propagate the droplet further to the command state.

Proportional-integral (PI) control extends proportional control by incorporating an integral component, which is a value proportional to the time integral of previous errors. In general, integral control is able to reach the command state faster and is able to eliminate steady state errors. However, due to the cumulative nature of integral control, it amplifies transient state errors such as overshoot, and requires marginally greater processing power.

Proportional-derivative (PD) control extends proportional control by incorporating a derivative component, which is a value proportional to the rate of change of the error. In general, derivative control stabilizes the error from oscillation by attenuating transient state errors such as overshoot. Furthermore, derivative control is very sensitive to erroneous samples from ADSA, which may occur from analysis on a bad image. Derivative control requires marginally greater processing power.

Proportional-integral-derivative (PID) control encompasses all three components of proportional integral and derivative control. It possesses the strengths of limitations of all three. It is noted that gains, the constant multiplier for each of P, I, and D control, needs to be

administrated. Inappropriately large gains may result in an oscillatory or unstable system. Such a system will not result in permanent equipment damage as the hardware is designed with limiters. However, an unstable system will require the manual reset of the entire CDS system if left unattended due to contamination and disconnection.

Fuzzy control is based on fuzzy logic. To simplify, bang-bang control is a control of discrete 0 and 1, and fuzzy control is a control continuous 0 and 1. For instance, when the error is large, the motor turns fast; when the error is small, the motor is slow; when the error is negligent, the motor stops; this is 3 states. In this case, the input is a fuzzy set and the output is a fuzzy set. The inputs can be the proportional error, the integral error, and the derivative error. The output can be the volume injected. In this case, the error fuzzy sets can translate (or fuzzifies) the actual error to a level. This volume fuzzy set can translate (or fuzzifies) the current volume to a level. Then the controller uses a "rule set" to find the output, the volume injected, fuzzy level. Lastly, the volume injected fuzzy set translates (or defuzzifies) this level to an actual volume to inject.

2.3.1 Closed Loop Control Limitations

Upon the completion of real time analysis, a control diagram for the proposed Single-Input-Single-Output (SISO) system is shown in **Figure 2.4**. There are several limitations in the controller design. Firstly, the ADSA's analysis or sampling rate greatly limits the controller. Secondly, there exists system disturbances in the plant; in an ideal system, the injected volume is proportional to the motor displacement. Lastly, there are transient state constraints such that the controller is to be applied to experiments involving Dipalmitoyl phosphatidylcholine (DPPC) monolayers and lung surfactants.

2.3.1.1 Sampling Time

In general, lower sampling rates requires less processing power, resulting in longer transient times or lower accuracy. Higher sampling rates requires more processing power, resulting in shorter transient times or better accuracy.[16] Due to the ADSA's numerical computations, its sampling rate is orders of magnitude slower than simpler measuring systems, such as displacement controllers or temperature controllers. Optimized by Yu et al, ADSA can sample at a max rate of 10 Hz.[17] Also, device latency shall be considered. After ADSA measures and reports the surface area of a droplet, the droplet may have propagated to another state. There is a latency of approximately 200ms.

2.3.1.2 System Disturbances

The CDS uses a motor-piston-syringe for droplet formation and deformation, shown in **Figure 1.1**. Motor displacement pushes the piston into the syringe, thereby injecting fluid into the droplet and vice versa. In an ideal system, motor voltage and on-time is proportional to motor displacement, which in turn is proportional to the volume of fluid injected. However, this was observed not to be the case. There are system disturbances arising from the physical system of the motor-piston-syringe which cannot be modeled due to its spontaneous action. For example, the static friction between the walls of the piston and the syringe, or fluid pressure disparities between push action and pull action in droplet expansion and compression, respectively.

2.3.1.3 Transient State Constraints

ADSA measures droplet in experiments involving biological fluids, namely lung surfactants. Lung surfactant facilitates the surface tension of alveolar cells. During pulmonary respiration simulation, the droplet is compressed and expanded at a physiologically relevant frequency of 15-20 periods per minute.[2] The transient state, of alveolar cells in pulmonary

respiration, is a near linear rise or fall. The controller shall not produce significant sharp rises or overshoots, and shall produce oscillation of 15-20 periods per minute at relevant amplitudes.

2.3.2 Open-Loop Plant (or Process) Model

The plant model, consisting of the high precision servomotor and the piston-syringe, can be approximated as a first order system. The input to this model can be modeled as a unit step. In the Laplace domain, the input can be modeled as:

$$\mathrm{f}(\mathrm{t}) = \begin{cases} 0, \mathrm{t} < 0 \\ \mathrm{k}, \mathrm{t} \geq 0 \end{cases} \rightarrow F(\mathrm{s}) = \frac{\mathrm{k}}{\mathrm{s}}, s \geq 0 \qquad \text{(Eq. 2.1)}$$

where k is the input value. The high precision servomotor contains a feedback loop such that its displacement response is nearly linear. The servomotor contains threaded shaft which acts as a helix gear to push a syringe piston. In the open-loop system where the inner servomotor control loop is closed, displacing below the rated velocity of 5 mm/s, there is a nearly linear transience and the absence of overshoot. The displacement error is in the order of micrometers. Hence, the relationship between the servomotor input and the piston displacement can be modeled as an integrator. In the Laplace domain, this first order system can be modeled as:

$$\mathrm{f}(\mathrm{t}) = \mathrm{k_m} * \mathrm{t} \rightarrow F(\mathrm{s}) = \frac{\mathrm{k_m}}{\mathrm{s}} \qquad \text{(Eq. 2.2)}$$

where $\mathrm{k_m}$ is the speed of the motor. There exist un-modeled nonlinearities observed to be non-dominant and are negligible. It was observed that this open loop model closely simulates the open-loop droplet control.

2.3.3 Closed Loop Model

Given the continuous-time feedback configuration can be represented in the figure below, the closed-loop transfer function in the Laplace domain may be simplified as:

$$\frac{\mathrm{y}}{\mathrm{r}} = \frac{\mathrm{C(s)*P(s)}}{\mathrm{C(s)*P(s)+1}} \quad \text{(Eq. 2.3)}$$

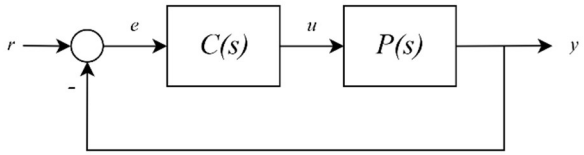

where C(s) is the controller, P(s) is the plant, r is the reference input, e is the error, u is the system input, and y is the output.

For closed-loop control, it is determined the system is controllable and observable. To achieve versatility, simplicity, and robustness, a PID controller was selected. During the transient state of the control, the digital controller of ADSA calculates the "error", i.e., the difference between the command state and the actual state, and thereafter actuates the motor and droplet to a value that is proportional to the current, the time integral, and the rate of change of the error. The continuous-time and discrete domain transfer function for PID control is:

$$u(t) = k_p * e(t) + \int_0^t k_i * e(\tau)\, d\tau + k_d \frac{de(t)}{dt} \rightarrow \quad \text{(Eq. 2.4)}$$

$$\mathrm{U(s)} = k_p * \mathrm{E(s)} + \left(\frac{k_i}{s}\right) * \mathrm{E(s)} + k_d * s * \mathrm{E(s)} \rightarrow \quad \text{(Eq. 2.5)}$$

$$\mathrm{U(z)} = k_p * \mathrm{E(z)} + \left(\frac{k_i}{1-\frac{1}{z}}\right) * \mathrm{E(z)} + k_d * (1 - \tfrac{1}{z}) * \mathrm{E(z)} \quad \text{(Eq. 2.6)}$$

where k_p is the proportional gain, k_i is the integral gain, k_d is the derivative gain, e is the value of the error, and u is the value of the command signal. Given the equation above for the transfer function for a closed-loop feedback system, the transfer function for the control system can henceforth be simplified as:

$$\frac{y}{r} = \left(\frac{k_m * k_s * (k_d * s^2 + k_p * s + k_i)}{(k_m * k_s * k_d + 1) * s^2 + k_m * k_s * k_p * s + k_m * k_s * k_i}\right) \quad \text{(Eq. 2.7)}$$

where k_m is the motor speed constant, k_s is the piston-syringe constant, r is the reference input and y is the output. To design for the k_p, k_i, and k_d parameters, and the constant k_m, the closed-loop zeros and poles are placed to meet the design specifications arrived based on the experimental setup. This is followed by appropriate tunings and simulations.

2.3.4 Discrete Time Model

In the digital feedback system, sensors, actuators, and ADSA incurs a latency in the system. The sensors, actuators, and ADSA, upon optimizations, can measure droplet properties at a rate of 10 Hz. Hence, controller must use data from the past, which incurs a sampling delay. Furthermore, this sampling delay may induce oscillations and instability. In the Laplace domain, a continuous delay can be modeled as,

$$f(t - \tau) \rightarrow e^{(-s*\tau)} * F(s) \quad \text{(Eq. 2.8)}$$

where τ is the continuous-time delay. For a digital controller, the delay can be modeled in the discretized z-domain. Through emulation, the controller can be designed for continuous-time domain specifications, and subsequently discretized to the z-domain, followed by appropriate tunings and simulations. A representation is shown in the figure below. Through bilinear transformation, the discrete-time controller can be approximately modeled as,

$$C(s)|\ s = \frac{2}{T}\frac{z-1}{z+1} \rightarrow D[z] \qquad \text{(Eq. 2.9)}$$

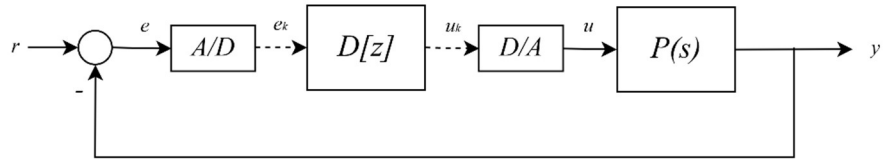

where T is the sampling time, C(s) is the continuous-time controller, and D[z] is the emulated discrete-time controller. P(s) is the continuous time plant, r is the reference input, e is the error, e_k is the discrete error, u_k is the discrete system input, u is the system input, and y is the output. A/D is an analog to digital converter and D/A is a digital to analog converter. The dashed lines represent discrete signals.

In addition, the continuous-time model of the system P(s) can be approximated and discretized to a model in the discrete-time domain. Subsequently, the discrete digital controller may be directly designed to meet continuous-time domain specifications. A representation is shown in the figure below. The closed-loop poles and zeros, based on continuous-time specifications, are selected in the s-domain and mapped to the z-domain, followed by appropriate tunings and simulations. The closed-loop transfer function of the model may be simplified as:

$$\frac{y_k}{r_k} = \frac{D[z]*G[z]}{D[z]*G[z]+1} \qquad \text{(Eq. 2.10)}$$

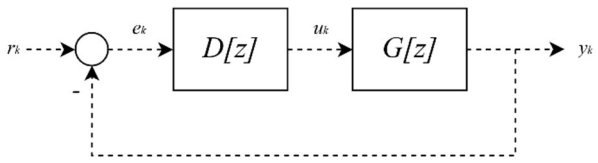

where D[z] is the digital discrete controller, G[z] is the discretized plant, r_k is the discrete reference input, e_k is the discrete error, u_k is the discrete system input, and y_k is the discrete output. The dashed lines represent discrete signals.

2.3.5 Model Simulations

The transient state of the droplet can be controlled by administering different controller gains. The integral component may be useful in overcoming small steady-state errors and increase the robustness of the controller. The derivative component may be useful in attenuating the transient state oscillations. Parallel with simulations, a series of loop tuning experiments were conducted to optimize the settling time, overshoot, and transient response. The settling time, the time where steady state is achieved, is observed to be 2-4 seconds. The overshoot, where the actual output exceeds the desired output prior to steady state, is largely non-existent. Furthermore, the transient response is largely that of linear one. The symmetry of PID control is susceptible to the differences between the dynamics of droplet formation and compression. However, observed through experiment, these phenomena are non-dominant.

To design for the sampling delay via emulation, the controller gain parameters are first determined in continuous-time specifications. Once the controller gains are determined, the controller may be discretized with Eq. 2.9, followed by appropriate loop tuning and simulation. To design for the sampling delay via direct design, the system model is discretized into the z-domain. For example, an integrator can be discretized as:

$$y[(k+1)T] = y(k+1) + T * u(k*T) \quad \text{(Eq. 2.11)}$$

$$y(s) = \frac{1}{s}u(s) \Rightarrow Y[z] = \frac{T}{z-1}U[z] \quad \text{(Eq. 2.12)}$$

Where T is the sample delay in seconds.

The closed loop poles, based on continuous-time specifications, are selected in the s-domain and mapped to the z-domain. Arriving at the desired transfer function, follow by appropriate loop tuning and simulation. To guarantee stability, in the s-domain, the closed loop pole exists in left right-hand plane, in the z-domain, the closed loop pole exists in open unit disk.

The resulting simplified model is modelled and simulated in MATLAB Simulink. **Figure 2.5** demonstrates this. Determined experimentally, the stiction of the interface between the piston and the glass of the syringe was inserted. Furthermore, to examine the robustness of the system, addictive and multiplicative noise was inserted. Moreover, the noise from the sensor of the industrial camera and the noise from the computational analysis of ADSA, are not significant, and are modeled as a Gaussian noise with a low variance in MATLAB Simulink.

2.4 Materials and Methods

2.4.1 Materials

The water used in this study was Milli-Q ultrapure water (Millipore, Billerica, MA). It has a resistivity greater than 18 MΩ·cm at room temperature. The pulmonary surfactant used in this study was Infasurf (Calfactant), which was a gift from ONY Inc. (Amherst, MA). Infasurf was purified from whole-lung bronchopulmonary lavage of newborn calves. Through an extraction process, Infasurf retained all of the hydrophobic components of bovine endogenous surfactant including phospholipids, cholesterol, and most hydrophobic surfactant proteins (SP-B and SP-C).[18-19] Infasurf has a total phospholipid concentration of 35 mg/mL and is stored frozen

in sterilized vials. On the day of experiments, it was thawed and diluted to a phospholipid concentration of 5 mg/mL with a saline buffer of 0.9% NaCl, 1.5 mM $CaCl_2$, and 2.5 mM HEPES, adjusted to pH 7.0. Dipalmitoyl phosphatidylcholine (DPPC) was purchased from Avanti Polar Lipids (Alabaster, AL) and used without further purification. DPPC was dissolved in chloroform to form a 1 mg/mL stock solution.

For biophysical simulations of pulmonary surfactant, detailed experimental protocols can be found elsewhere.[11, 20] Briefly, a droplet (~ 10 μL) of 5 mg/mL Infasurf was dispensed onto the CDS drop pedestal, maintained within an environmental chamber that controls the physiologically relevant conditions, *i.e.*, 37 °C and 100% relative humidity. After drop formation, the surface tension quickly decreased to an equilibrium value of approximately 22-25 mN/m,[21] indicating formation of an adsorbed surfactant film at the air-water interface. Once the equilibrium was established, the adsorbed surfactant film was compressed and expanded at a rate of 5 seconds per cycle by withdrawing and injecting water into the droplet using the motorized syringe. The compression ratio was controlled to be less than 20% of the initial surface area to simulate normal tidal breathing. A minimum of five continuous compression−expansion cycles were studied for each droplet. It was observed that the cycles became repeatable after the first cycle.

For the study of self-assembled phospholipid monolayers at room temperature, a tiny amount of 1 mg/mL DPPC stock solution was spread using a microsyringe onto a droplet of pure water of which the surface tension was recorded as γ_0.[22] The droplet was then slowly expanded to increase surface tension (γ) until the corresponding surface pressure ($\pi = \gamma_0 - \gamma$) was reduced to ~1 mN/m. The droplet was left undisturbed for an additional 1 min to allow evaporation of the solvent. The spread DPPC monolayer was subsequently compressed at a quasi-equilibrium rate

of 0.06 cm^2/min, corresponding to 0.17% initial surface area per second. Langmuir-Blodgett (LB) transfer from the droplet was implemented by lifting a small piece of freshly peeled mica sheet at a speed of 1 mm/min, under controlled surface pressure. Topographical images were obtained using an Innova AFM (Bruker, Santa Barbara, CA). Samples were scanned in air in contact mode with a silicon nitride cantilever of a spring constant of 0.12 N/m and a tip radius of 2 nm. Lateral structures were analyzed using Nanoscope Analysis (version 1.5).

2.4.2 Methods

Since its development, ADSA has been routinely used as an open-loop system for determining properties of drop/bubble (*i.e.*, surface tension, surface area, and volume) by analyzing its images.[1, 4] Here, we further developed ADSA into a closed-loop system in which droplet properties determined in real-time are used as feedback control parameters to actuate the droplet towards desired targets. A diagram of the feedback control loop is illustrated in **Figure 3.1**. A digital PID controller was directly integrated into ADSA. In the closed-loop feedback control system, ADSA continuously calculates the error, *i.e.*, the difference between the target values and the current values, and thereafter automatically actuates the droplet towards the target values using a motorized syringe (consisting of a high-precision servomotor and a piston-syringe system) with PID control. The transient state of the droplet can be controlled by administering proper PID gains. The feedback control system was modeled in the time domain, the Laplace domain (in which the time domain representation is transformed into a frequency domain representation), and the Z-domain (in which the digital discrete time representation is transformed into another frequency domain representation).[23]

There are several advantages and novelties of the closed-loop ADSA in comparison with previous droplet manipulation methods. 1. To the best of our knowledge, the closed-loop ADSA is the first method capable of controlling the volume, surface area, or surface tension of millimeter-sized single droplets. Previous methods can only control drop volume. However, knowledge about the surface area and surface tension of the droplet can be only obtained by post-experimental analysis of drop images acquired during the experiments. Hence, control parameters such as area compression ratios and targeting surface tension values cannot be set *a priori*. In comparison, the closed-loop ADSA analyzes the deformed drop shape in real time and hence eliminates the need of image acquisition for post-analysis. Consequently, the closed-loop ADSA allows live manipulation of a droplet. 2. Since the closed-loop ADSA manipulates the droplet by directly controlling properties of the target droplet, it is independent of the physical methods of fluid actuation, regardless of the fluid is driven by a motorized syringe or by a piezoelectric transducer. 3. Being a free-standing method, although the closed-loop ADSA is demonstrated here with a sessile drop setup, it can be readily applied to manipulate other drop or bubble shapes, such as pendant drop or captive bubble, provided that ADSA is applicable.

2.5 Results and Discussion

2.5.1 Control of Volume

In this study, we demonstrate direct control of drop volume with the closed-loop ADSA. **Figure 2.7** shows the manipulation of a 60 μL water droplet on the CDS platform at room temperature. The volume of the droplet (panel c) was decreased and increased stepwise with a step of every 10 μL, followed by steps of every 20 μL and 40 μL, respectively. Images of this

droplet at different volumes are shown as inserts in panel a. It is clear that the volume change was controlled to be largely linear with respect to time and without significant overshoot once reaching the target values within a 1% tolerance. Response to the control was fast. Regardless of the magnitude of volume change, the target values were reached within 1 second. It can be also seen that during the manipulation of drop volume, the surface tension (panel a) of pure water fluctuates at 71±2 mN/m, in agreement with the literature value.[22] The deviation mostly takes place upon reducing the drop volume. This is most likely due to traces of impurities (that cause surface tension decrease) and/or intrinsic artifacts of drop shape analysis at small volumes (that cause surface tension increase).[24-25]

We further demonstrate the usefulness of the ADSA-based volume control by solving a real-world problem, *i.e.*, droplet evaporation. Evaporation is an inevitable problem of any droplet-based apparatus in which the drop volume decreases with time due to evaporation at a rate affected by the surface area of the droplet, diffusivity of the liquid, and the environmental conditions.[25] For instance, protein adsorption may take several hours to complete, during which evaporation may cause significant artifact by contracting the air-water interface of the droplet.[26-27] Another example in which the compensation of droplet evaporation is essential is the study of gas adsorption at the air-water interface.[28] Volume loss is especially problematic for small droplets as the highly curved drop surface increases the chemical potential of evaporation.[29]

The rate of evaporation of the droplet has been investigated extensively. Birdi and Winter concluded evaporation rate remains constant when the contact line is pinned.[30] Shanahan and Bourges concluded there are several distinct stages of evaporation.[31] Hu and Larson employ an analytical theory and a computational method using the finite element method (FEM).[32] It can be

said that the evaporation rate of a sessile droplet is constant in time, given smaller contact angles. Hu and Larson present a simple approximate expression:

$$y(s) = \pi \, R \, D \, (1 - H) c_v (0.27\theta^2 + 1.30) \qquad \text{(Eq. 2.13)}$$

where R is the contact-line radius, D is the diffusivity, c_v saturated water vapor concentration, H is the relative humidity, and θ is the contact angle. Moreover, given the presence surfactants, the rate of evaporation lessens significantly.

Here, we demonstrate that the ADSA-based volume control maintains a constant drop volume over a prolonged time period by automatically compensating the effect of evaporation. As shown in **Figure 2.8**, without control, the volume of a 60 μL water droplet shrinks by 30% over 30

due to natural evaporation. In comparison, with the ADSA-based control, the drop volume was maintained at constant over the same time period with volume variations less than 0.5%.

It should be noted that it is also possible to control the volume of a droplet using a high-precision syringe pump, if only the linear displacement of the syringe pump is properly calibrated and converted to variations in the drop volume. However, our ADSA-based method represents a novel feedback control system that drives the motor to directly control the drop volume with the value determined in real-time by ADSA. Hence our method is more accurate, faster, and does not require calibration. The entire process is automatic without the need of any human intervention.

2.5.2 Control of Surface Area

Compared to the control of drop volume, the control of surface area and surface tension of the droplet is exceedingly complicated due to the nonlinearity of these two properties. To demonstrate the nonlinearity of surface area and surface tension with respect to the drop volume, we have conducted a comparative experiment of shrinking three droplets of the same initial volume. These are a pure water droplet, a DPPC-covered water droplet, and an Infasurf droplet. **Figure 2.9** shows the surface area (panel a) and surface tension (panel b) of these three droplets as a function of the reducing volume. It is clear that only the surface area of the pure water droplet is nearly linearly correlated with the drop volume. Nonlinearity in surface area exists for both DPPC-covered and Infasurf droplets, due to drop deformation upon reducing volume. Surface tensions of all three droplets are nonlinearly correlated with the drop volume, in which the surface tension of pure water remains unchanged while reducing volume, and the surface tensions of DPPC-covered and Infasurf droplets decrease quickly to near-zero value upon reducing volume (*i.e.*, the compression of lipid monolayer at the air-water interface).

Nonlinearity of the surface area and surface tension renders the control of these two droplet properties using a regular syringe pump impossible. However, being a feedback control system, our closed-loop ADSA can readily control the surface area or surface tension of the droplet without additional difficulties compared to the control of drop volume. In this study, we demonstrate the direct control of droplet surface area with closed-loop ADSA. We first demonstrate the ADSA-based area control with a similar experiment using water droplets as shown in **Figure 2.10**.

We further demonstrate the usefulness of the ADSA-based area control for solving a research problem, *i.e.*, *in vitro* biophysical simulations of pulmonary surfactant (PS). PS is a phospholipid-protein mixture that is synthesized by alveolar type II epithelial cells. The primary biophysical function of pulmonary surfactant is to reduce the alveolar surface tension, thus contributing to the elastic recoil of the lungs and increasing the pulmonary compliance.[18] A key requirement of *in vitro* biophysical simulations of PS is to mimic the intra-alveolar environment of the lungs. This requires not only rigorous control of experimental conditions to physiological relevance, such as the core body temperature of 37 ºC and 100% relative humidity, but also high-fidelity simulation of respiratory cycles during normal tidal breathing, such as the respiratory rate (*e.g.*, 5 seconds per cycle) and the control of surface area variations to be less than 20% per cycle.[33] Numerous studies have demonstrated that variations in alveolar surface area during respiration are small.[33-35] Surface area of the lungs does not change more than 30% during a deep breath between 40 and 100% total lung capacity (TLC). During normal tidal breathing between 40 and 50% TLC, the area variation is less than 10%.[33-35] All this physiological evidence suggests that natural PS films must have a very low compressibility contributing to lung recoil.[36] However, direct control of surface area during droplet oscillation was not possible in previous *in vitro* simulations.

Figure 2.11 demonstrates the advantages of closed-loop ADSA in biophysical simulations of a natural PS, Infasurf, under physiologically relevant conditions. It can be seen that with surface area control, the adsorbed surfactant film was compressed precisely by 15% area reduction (mimicking exhalation), and subsequently expanded back to its original area (mimicking inhalation). A minimum surface tension of ~2 mN/m was reached with the 15% compression, indicating a low film compressibility of approximately 0.5 $(mN/m)^{-1}$. The

compression and expansion curves coincide closely with each other without showing a significant hysteresis, which represents an ideal biophysical simulation of the respiratory cycle of natural PS.

In contrast, without surface area control, the actual compression ratio of surfactant films cannot be set *prior to* the dynamic cycling experiments. Consequently, the surfactant films are commonly overcompressed or undercompressed, thus failing to mimic the physiological conditions of respiration. As the example shown in Figure 2.11, the surfactant film without area control was compressed by 22% area reduction. It is found that as soon as the area was reduced beyond 15%, the surface tension did not decrease anymore. Rather, the compression curve leveled off at the minimum surface tension, indicating extensive film collapse. Collapse of the alveolar surfactant film is uncommon in mammalian lungs under normal conditions.[37] Hence, this extra area compression is considered to be "overcompression" that is an artifact introduced by the *in vitro* biophysical simulation.[38] Because of this overcompression, the compression-expansion cycle shows a significant hysteresis loop. The area enclosed in the hysteresis loop indicates the amount of mechanical energy loss per respiratory cycle, which is again an artifact for *in vitro* biophysical simulation of natural PS.[39]

2.5.3 Control of Surface Tension and Surface Pressure

To demonstrate the control of surface tension/pressure, we used the CDS as a miniaturized Langmuir balance to study the compression isotherm of a self-assembled DPPC monolayer at room temperature. **Figure 2.12** shows the surface pressure of the DPPC monolayer as functions of the relative surface area (π-A curve) and the compression time (π-t curve), respectively. It can be seen that the π-A curve is consistent with well-characterized DPPC

compression isotherms reported in literature.[18, 40-41] At large surface area and low surface pressure, the DPPC monolayer is in a fluid-like liquid-expended (LE) phase, while the surface pressure only increases slowly with area reduction. After passing a phase transition plateau at about 8.5 mN/m, the DPPC monolayer is transformed into a solid-like tilted-condensed (TC) phase at which the surface pressure increases rapidly with compression, indicating a very low film compressibility for the TC phase DPPC monolayer.[42]

As demonstrated by the π-t curve shown in Figure 2.12, with the ADSA-based surface tension/pressure control, we were able to compress the DPPC monolayer to a target surface pressure (*i.e.*, 8.5, 20, 30, 40, 50, and 60 mN/m) and maintain it over a 100 s period. It can be seen that when the controlled pressure reaches 30 mN/m, a small overshoot appears due to hysteresis incurred by stiction of the piston-syringe system. However, the controller is able to correct the overshoot and bring the steady-state surface pressure to the target value. The steady-state error of this control is <1.5%.

The precise control of surface tension/pressure over time allows extended investigation of self-assembled monolayers and thin-films fabricated at the droplet surface. One such application is *in situ* Langmuir-Blodgett (LB) transfer from the droplet surface. To date, LB transfer of films from the air-water interface to a solid substrate under controlled surface pressure is primarily implemented with a Langmuir trough.[42] After LB transfer, the film can be studied in detail by various microscopic and spectroscopic techniques for characterizing its lateral structure and molecular organization.[18, 39, 43] Here, taking advantage of the ADSA-based surface tension/pressure control, we have implemented the first *in situ* LB transfer of DPPC monolayer from the droplet surface. During the LB transfer, ADSA analysis was restricted to partial drop profiles that were not disturbed by the substrate passing the air-water interface. The insert in

Figure 2.12 shows an AFM topographic image of the DPPC monolayer transferred within the phase transition plateau region, *i.e.*, 8.5 mN/m. The AFM image shows clearly coexistence of the LE phase and the signature kidney-shaped TC domains well-documented in literature.[18, 44]

2.6 Conclusion

To demonstrate the feasibility and advantages of this droplet manipulation method, we have engaged it in three applications of importance in various surface science studies. In the first application, we maintained the volume of a water droplet over a prolonged time period by automatically compensating natural evaporation. In the second application, we demonstrated the feasibility of controlling the surface area of an oscillating droplet for *in vitro* biophysical simulations of natural pulmonary surfactant. By precisely controlling surface area variations during dynamic droplet oscillation, our method allows high-fidelity *in vitro* biophysical simulations of respiratory mechanics. In the third application, we demonstrated the effective control of surface pressure during compression of a self-assembled phospholipid monolayer. By controlling surface pressure over time, we implemented the first *in situ* Langmuir-Blodgett (LB) transfer from a monolayer-covered droplet. All these applications have demonstrated that closed-loop ADSA is highly practical in automating droplet manipulation in a variety of material and surface science applications, such as thin-film fabrication, self-assembly, and biophysical study of pulmonary surfactant.

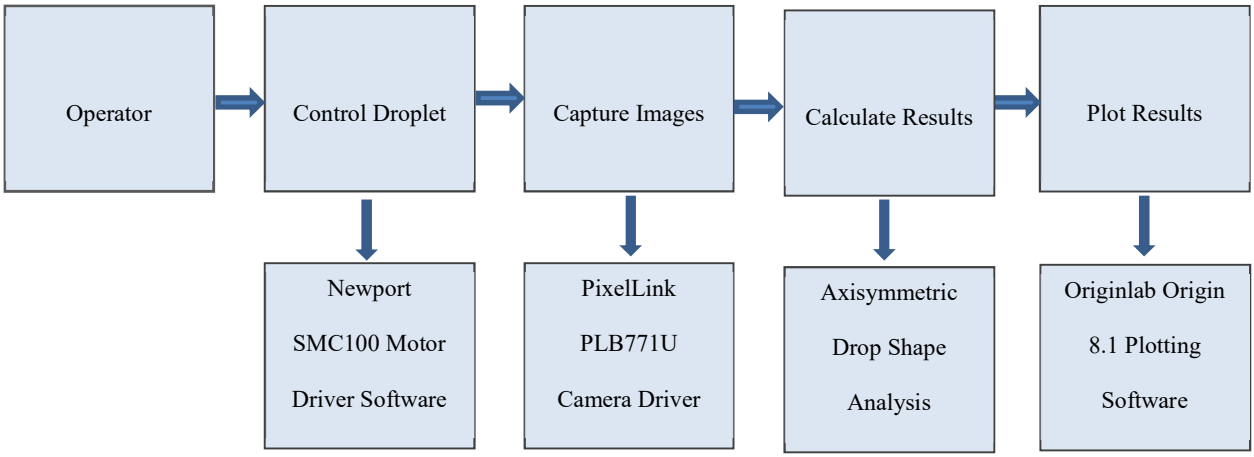

Figure 2.1 Original methodology of the experimental apparatus known as the CDS. First, the experiment takes place which revolves the manual control of the droplet; second, manual image acquisition takes place; third, images are manually fed into the Axisymmetric Drop Shape Analysis GUI for analysis and results; fourth, results are visualized through a plotting software. These steps are on top and the corresponding software are placed below.

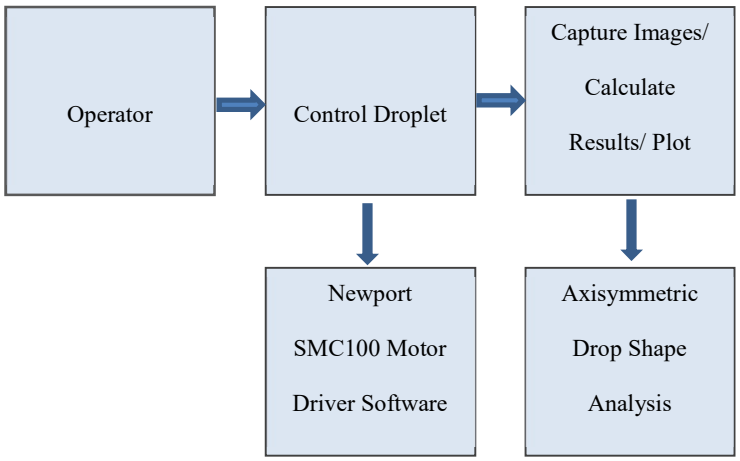

Figure 2.2 Methodology of the CDS, after real-time analysis integration. Real-time ADSA integrates the analysis process. First, the experiment takes place which revolves the manual control of the droplet; second, the Axisymmetric Drop Shape Analysis GUI captures, analyzes, and visualizes and results.

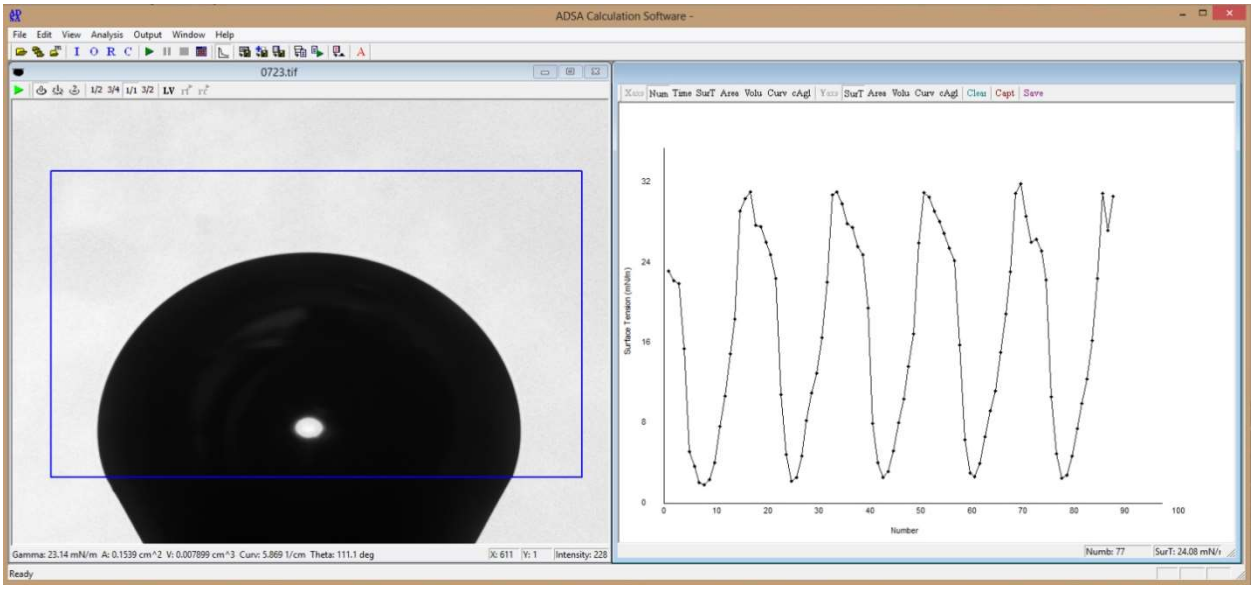

Figure 2.3 Sample screenshot of the ADSA GUI interface after real-time analysis integration. Note the left child class shows the real-time camera preview, and the right child shows the scatter-line plot for surface tension during an experiment involving droplet oscillation. There are several execution threads operating in parallel to facilitate this.

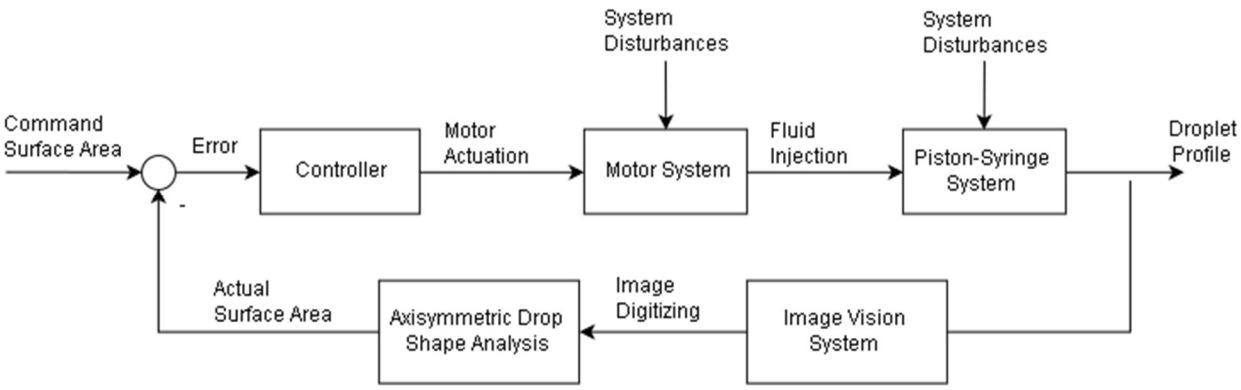

Figure 2.4 Proposed control system for ADSA and CDS based experiments. A command is set to the controller which actuates the motor to inject fluid for droplet based experiments. The droplet is captured by an image vision system which is sent to ADSA for analysis. Note the system disturbances incurring from the motor system and piston syringe system. Note the feedback component of this control diagram.

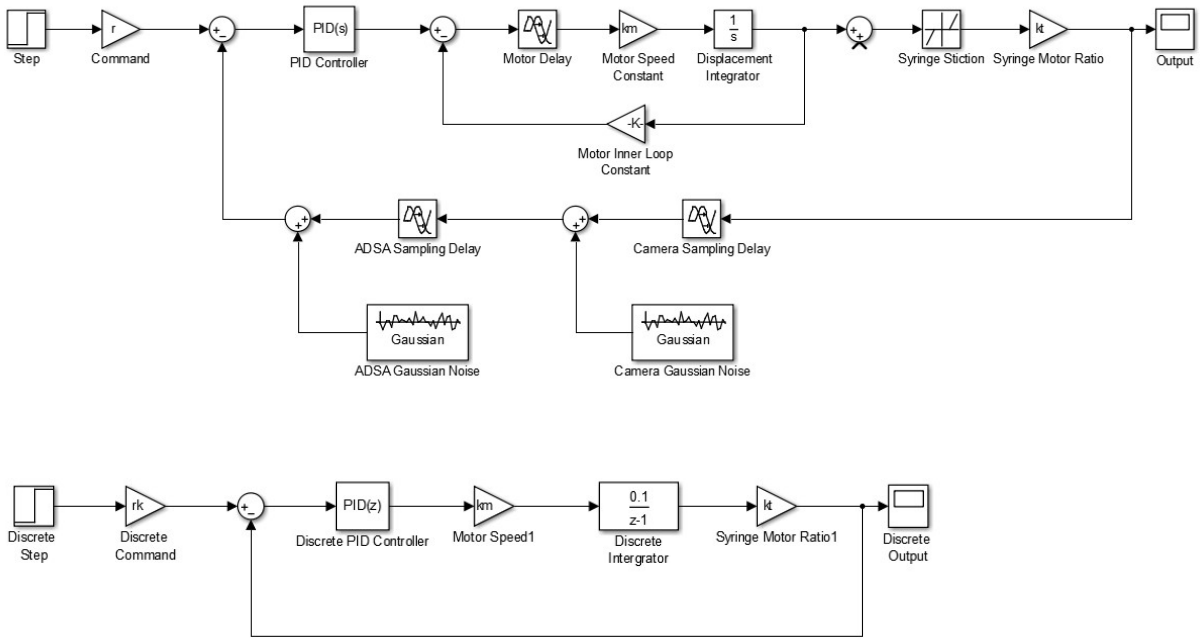

Figure 2.5 Simulation of feedback control system through MATLAB Simulink. Determined experimentally, the stiction of the interface between the piston and the glass of the syringe was inserted. Furthermore, to examine the robustness of the system, addictive and multiplicative noise was inserted. Moreover, the noise from the sensor of the industrial camera and the noise from the computational analysis of ADSA, are not significant, and are modeled as a Gaussian noise with a low variance. Some discrete domain simulation is included at the bottom.

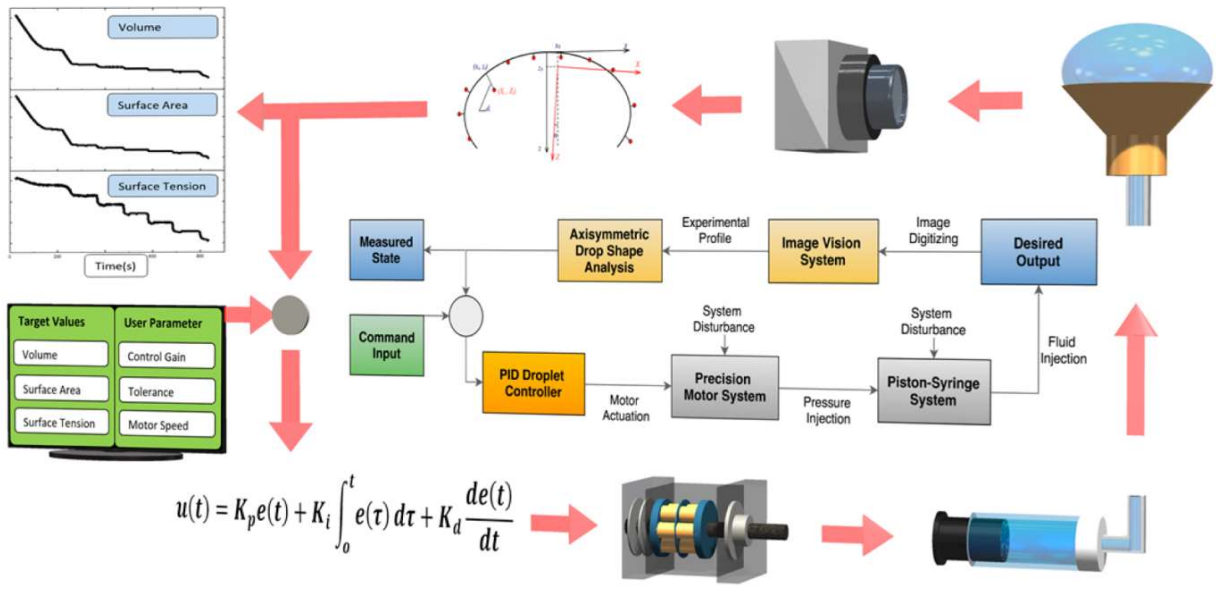

Figure 2.6 The axisymmetric drop shape analysis (ADSA) feedback control system, integrated into the constrained drop surfactometer (CDS). In the CDS, a liquid droplet is "constrained" on a 3-5 mm carefully machined pedestal with a knife-sharp edge. The droplet is continuously monitored by ADSA in real-time. Properties of the droplet, including its volume, surface area, and surface tension, are controlled with the closed-loop ADSA. An integrated PID controller continuously calculates the error, *i.e.*, the difference between the target values and the current values, and converts the error into a command signal with proper PID gains. The PID controller is modeled by $u(t) = k_p e(t) + \int_0^t k_i e(\tau) d\tau + k_d \frac{de(t)}{dt}$, where k_p is the proportional gain, k_i is the integral gain, k_d is the derivative gain, $e(t)$ is the value of the error, and $u(t)$ is the value of the command signal. The resultant command signal controls a motorized syringe, consisting of a high-precision servomotor and a piston-syringe system, to actuate the droplet towards the target values.

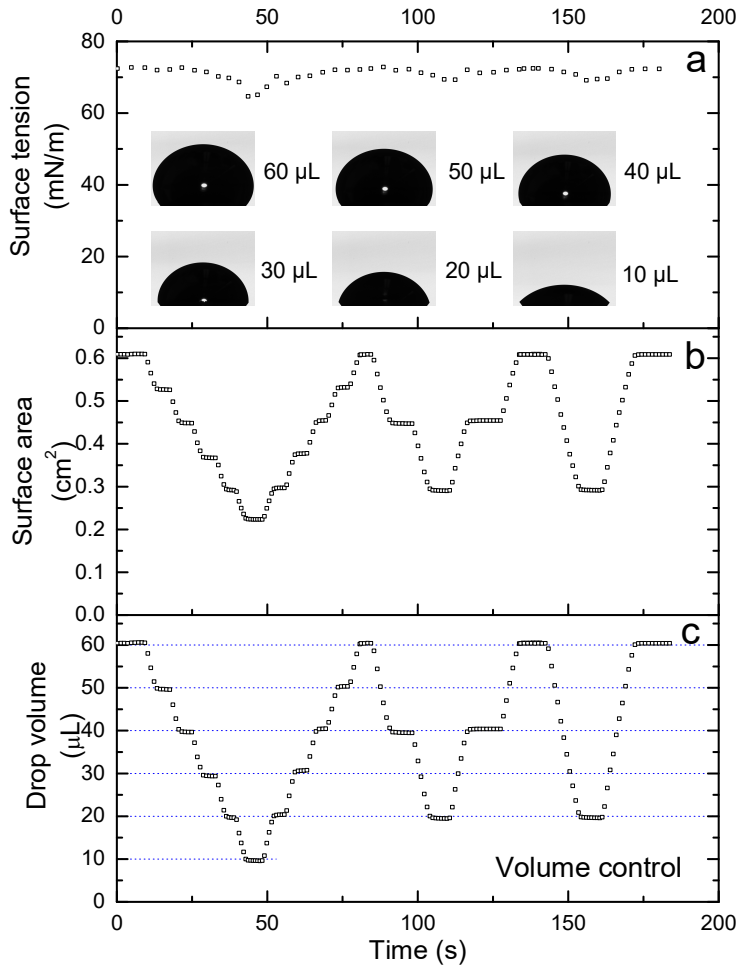

Figure 2.7 Demonstration of the closed-loop ADSA for controlling drop volume. The volume of a 60 μL water droplet (panel c) was decreased and increased stepwise with a step of every 10 μL, followed by steps of every 20 μL and 40 μL, respectively. Images of this droplet at different volumes are shown as inserts in panel a. It is clear that the change of volume was controlled to be largely linear without significant overshoot once reaching the target values within a 1% tolerance. During manipulation of drop volume, the surface tension (panel a) of pure water is largely unchanged, and the surface area (panel b) of the water droplet also varies largely linearly with respect to time.

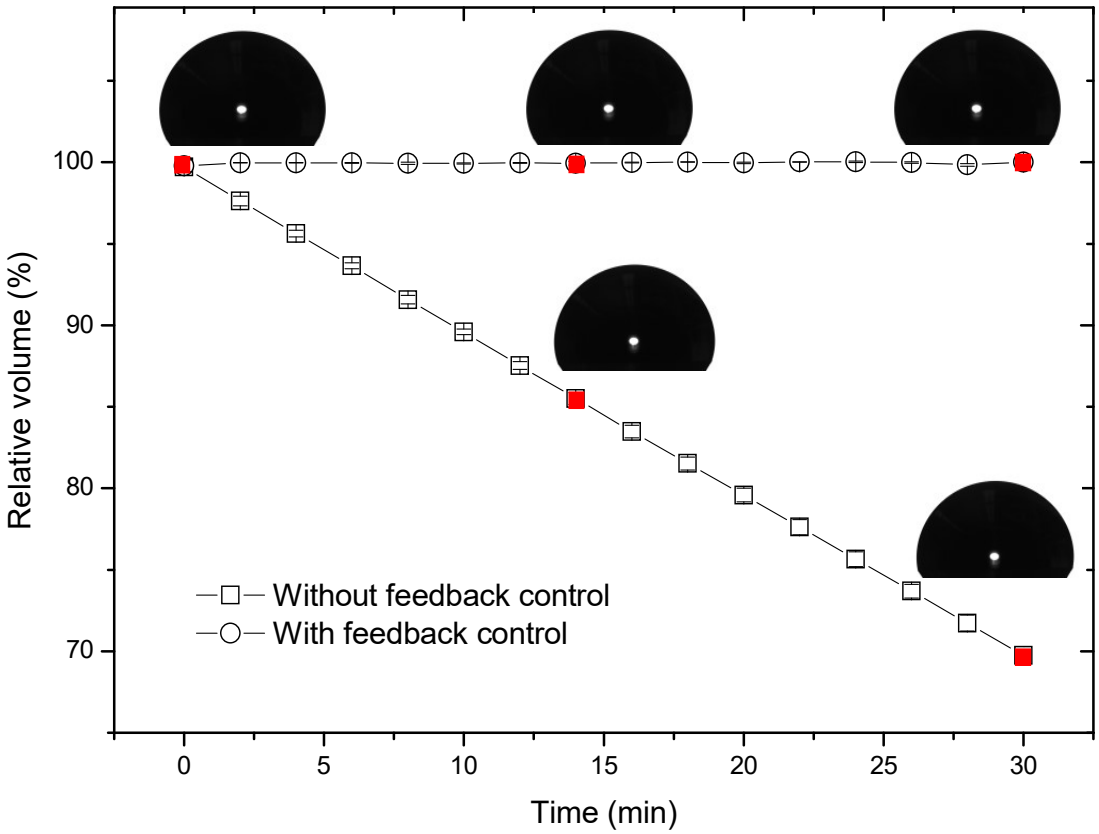

Figure 2.8 Demonstration of the closed-loop ADSA for maintaining constant drop volume by automatically compensating evaporation. Without the control, the volume of a 60 μL water droplet shrinks by 30% over 30 min due to natural evaporation. With the control, the drop volume was maintained at constant over the same time period with volume variations less than 0.5%. Results are shown as mean ± SD averaged from three repetitions. Inserts are drop images at different time points indicated by red solid symbols on the curves, showing changes in drop volume.

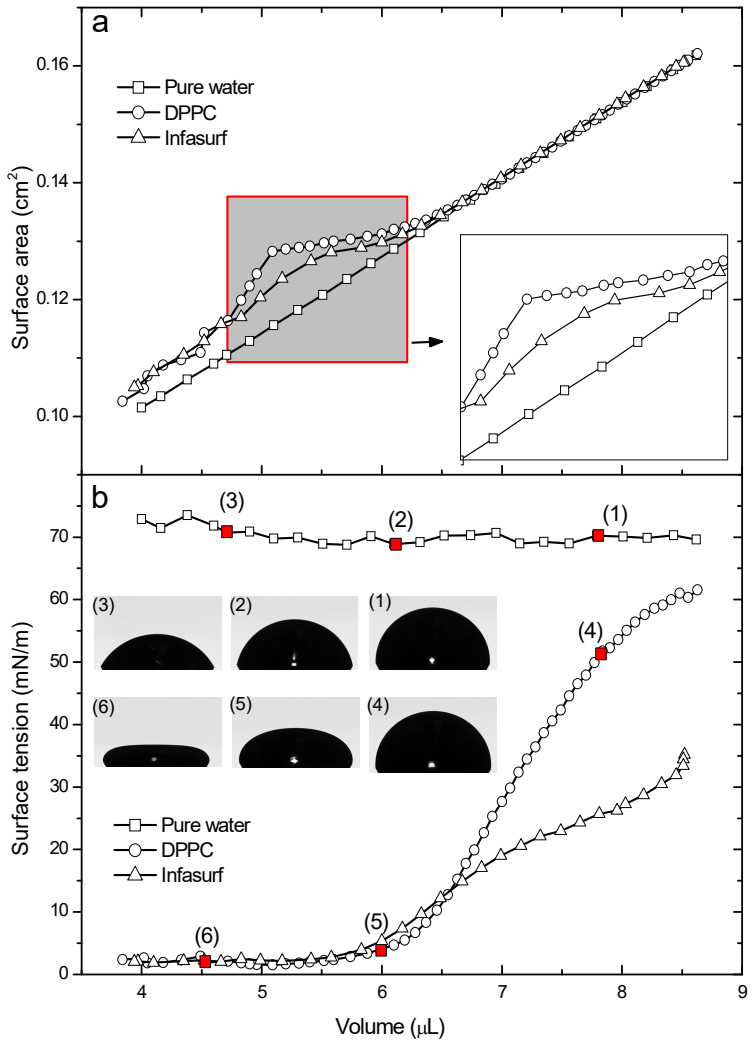

Figure 2.9 Nonlinearity of surface area and surface tension with respect to the drop volume. Three droplets, *i.e.*, a pure water droplet, a DPPC-covered droplet, and an Infasurf droplet, were shrunk linearly in volume. It is clear that only the surface area of the pure water droplet is nearly linearly correlated with the drop volume. Nonlinearity in surface area exists for both DPPC-covered and Infasurf droplets, due to drop deformation upon reducing volume. Surface tensions of all three droplets are nonlinearly correlated with the drop volume, in which the surface tension of pure water remains unchanged while reducing volume, and the surface tensions of DPPC-covered and Infasurf droplets decrease quickly to near-zero value upon reducing volume. Inserts are drop images at different volumes of the three droplets indicated by red solid symbols on the curves.

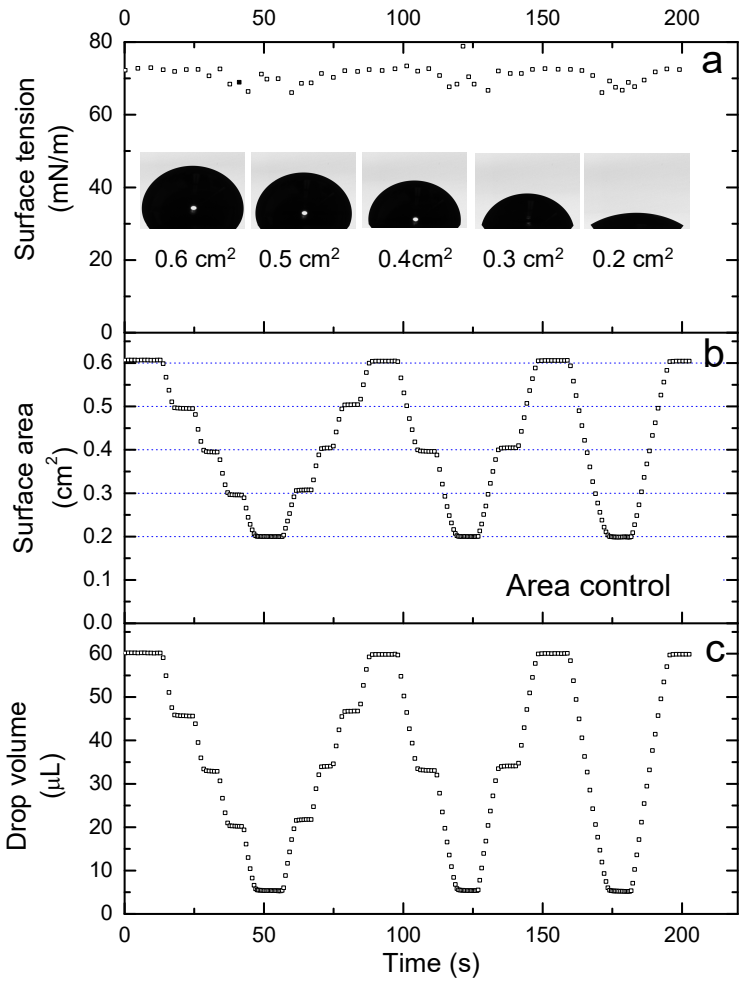

Figure 2.10 Demonstration of the closed-loop ADSA for controlling surface area. The surface area of a 0.6 cm^2 water droplet (panel b) was decreased and increased stepwise with a step of every 0.1 cm^2, followed by steps of every 0.2 cm^2 and 0.4 cm^2, respectively. Images of this droplet at different surface areas are shown as inserts in panel a. It can be found that the change of surface area was controlled largely linear with respect to time without significant overshoot once reaching the target values within a 1% tolerance, with the similar tendency of drop volume control. During the manipulation of surface area, the surface tension (panel a) of pure water is largely unchanged and drop volume follows the same tendency of surface area.

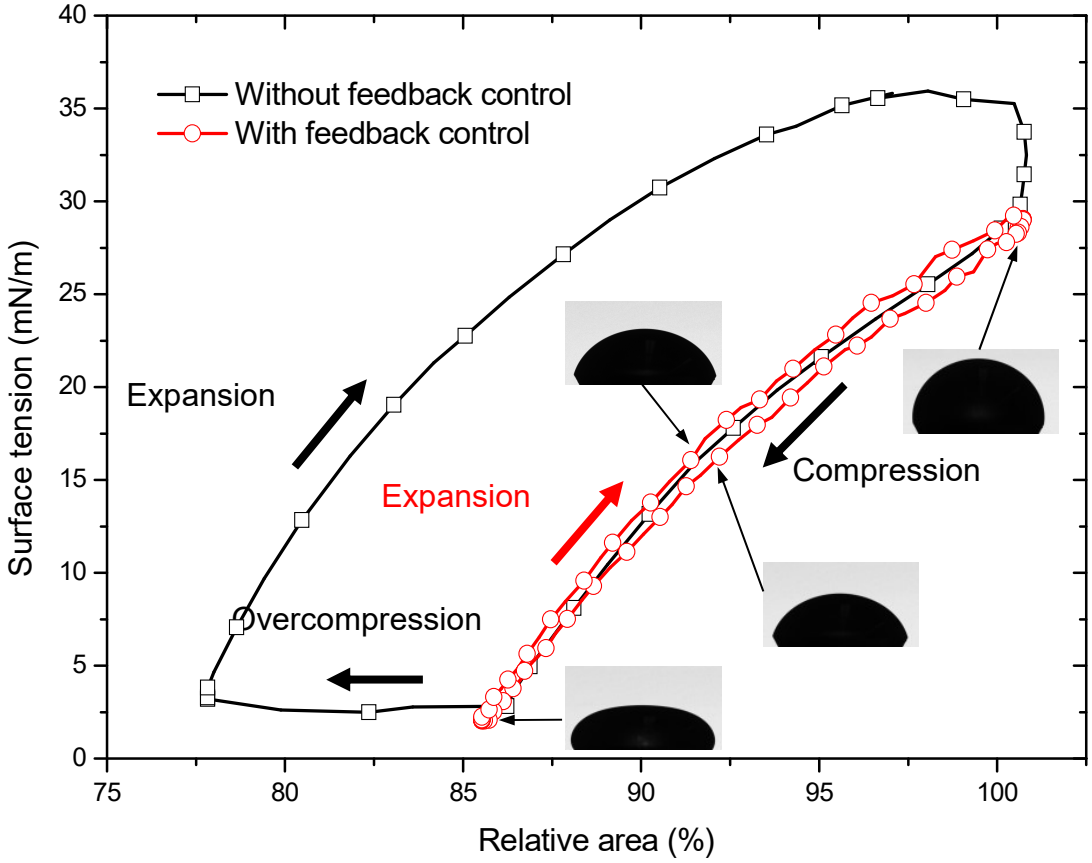

Figure 2.11 Demonstration of the closed-loop ADSA for controlling area variations in biophysical simulation of a natural pulmonary surfactant, Infasurf, under physiologically relevant conditions. With the area control, the surfactant film was compressed precisely by15% area reduction, and subsequently expanded back to its original area. A minimum surface tension of ~2 mN/m was reached with the 15% compression. The compression and expansion curves coincide closely with each other without showing a significant hysteresis. Without the area control, the surfactant film was compressed by 22% area reduction. When the area was reduced beyond 15%, the surface tension did not decrease but leveled off at the minimum value, indicating extensive film collapse, which is an artifact due to overcompression of the surfactant film. Images of the droplets along the cycle path are demonstrative of surface tension being a function of drop shape.

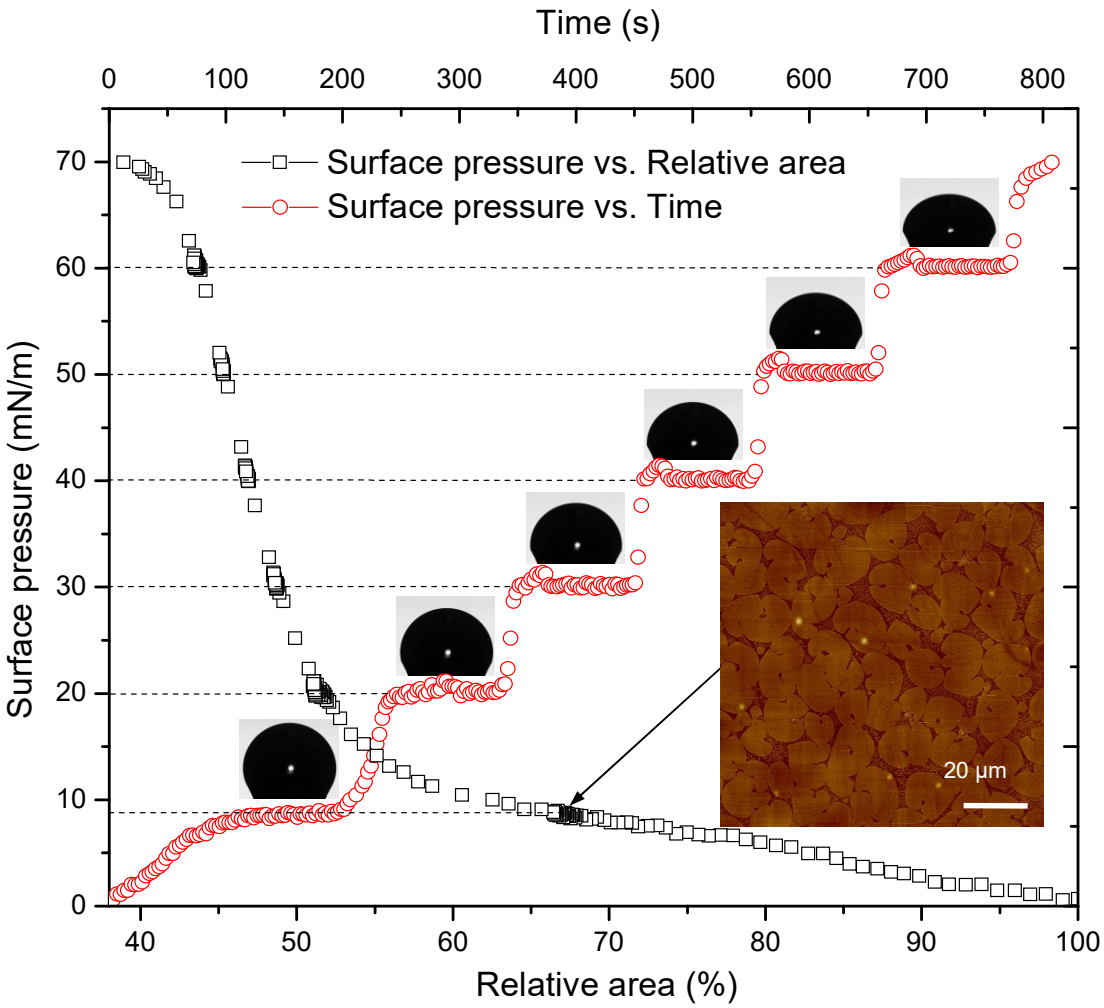

Figure 2.12 Demonstration of the closed-loop ADSA for controlling surface pressure for in situ Langmuir-Blodgett (LB) transfer of DPPC monolayers from the droplet. The obtained surface pressure-area curve is consistent with well-characterized DPPC compression isotherms reported in literature. The surface pressure-time curve shows the compression of the DPPC monolayer to a target surface pressure (*i.e.*, 8.5, 20, 30, 40, 50, and 60 mN/m) and maintained over a 100 s period. When the controlled pressure beyond 30 mN/m, a small overshoot appears due to the hysteresis incurred by stiction of the piston-syringe system. However, the controller is able to correct the overshoot and bring the steady-state surface pressure to the target value. The steady-state error of this control is <1.5%. The insert shows an AFM topographic image (100×100 μm; z-range 5 nm) of the DPPC monolayer transferred under a controlled surface pressure within the phase transition plateau region, *i.e.*, 8.5 mN/m. The image shows clearly coexistence of the LE phase and the signature kidney-shaped TC domains well-documented in literature.

Table 2.1 The benefit decision matrices of five plotting solutions. Usability, the elementary function of the plotting interface, earned a weight of 5 of 10, while other criteria earned lesser weight; and technical options yielded more benefit. The significance of each of the factors was distributed in accordance to the projected relative time over the course of the project.

	Usability (5)	Mathematic Potential (2)	Computing Speed (2)	Friendliness/ Cosmetics (1)	Sum (50)	Percent (100)
MathGL	4 ×5	5 ×2	4 ×2	4 ×1	43	86
GNU plot	4 ×5	4 ×2	4 ×2	3 ×1	39	78
PLplot	3 ×5	4 ×2	4 ×2	2 ×1	34	68
MS Chart Controls	4 ×5	3 ×2	3 ×2	2 ×1	33	66
MiniPlot	3 ×5	2 ×2	3 ×2	1 ×1	25	50
Build Anew	4 ×5	3 ×2	3 ×2	2 ×1	33	66

Table 2.2 The time cost decision matrices of five plotting solutions. For the time cost matrix, more technically challenging options required longer implementation and maintenance times. The significance of each of the factors was distributed in accordance to the projected relative time over the course of the project.

	Construction Costs (4)	Integration Costs (3)	Maintenance Costs (2)	Compilation Costs (1)	Sum (50)	Percent (100)
MathGL	3 ×4	5 ×3	4 ×2	5 ×1	40	80
GNU plot	3 ×4	4 ×3	4 ×2	5 ×1	36	72
PLplot	2 ×4	4 ×3	5 ×2	4 ×1	33	66
MS Chart Controls	2 ×4	3 ×3	3 ×2	3 ×1	26	52
MiniPlot	4 ×4	2 ×3	2 ×2	2 ×1	28	56
Build Anew	4 ×4	1 ×3	1 ×2	1 ×1	22	44

Chapter 3. Arbitrary Waveform Generation

3.1 Introduction

Droplet oscillation has an important role in a wide range of scientific and industrial applications, such as mass transfer,[45] thin films,[6] microfluidics,[46] biophysical simulations,[47] interfacial reactions,[7] and interfacial rheology.[48] In these applications. studying interfacial models through droplet oscillation offers a number of advantages.[49] First, recent advances in droplet tensiometric methodologies have increased the effectiveness of droplet oscillation.[50] Second, the droplet platform has a large surface-area-to-volume ratio which increases the rate of surface reactions and interfacial assemblies. Third, the small volume of droplets can facilitate the study of expensive chemicals, such as scarce biological fluids. Fourth, it is possible to enact a precise environmental control, including the control of temperature, atmosphere, and surface/interfacial composition, thereby avoiding contaminations and allowing versatile investigations across the droplet surface.[51] [2]

Droplet oscillation methods oscillate the droplet through preprogrammed fluid actuation movements, such as motorized syringe pumps. At sufficiently large Bond numbers, *e.g.,* at millimeter-sized diameters and/or at low surface tensions, the droplet deforms significantly from a spherical bead profile, such that the droplet volume and surface area largely deviate from a linear relationship.[15] [17] A number of techniques oscillate volume and surface area of micron-sized droplets with smaller Bond numbers.[12-14] However, when oscillating millimeter-sized droplets with larger Bond numbers, surface area is approximated through volume.[52] Moreover, volume oscillations are largely confined to preprogrammed ramp and sine waveforms. Hence, neither volume nor surface area can be directly and freely oscillated with current techniques.

In this paper, we developed a novel waveform generator for oscillating millimeter-sized droplets, based on axisymmetric drop shape analysis (ADSA). ADSA is a computational droplet measurement technique developed by Neumann et al.[1 4] ADSA determines the volume, surface area, and surface tension of a droplet numerically by fitting the experimental droplet profile to theoretical droplet profiles from the Laplace equation of capillarity. Recently, ADSA was coupled with real-time analysis and feedback control to manipulate droplet volume, surface area, and surface tension.[17] Extending upon this work, we developed, to the extent of our knowledge, the first waveform generator capable of directly controlling a droplet's volume or surface area to an arbitrary waveform. Through this waveform generator, we can oscillate millimeter-sized droplets with a high degree of freedom and accuracy, up to reported limiting frequencies and to an amplitude not previously possible.[53]

We demonstrate the strengths, applicability, and limitations of this droplet manipulation method in three ways. First, we demonstrated arbitrary waveform generation by controlling the volume and surface area of a pure water droplet to sine, triangle, square, and sawtooth waveforms. Second, we evaluated the accuracy of the arbitrary waveform generation through a coefficient of determination (R^2) analysis. Third, we apply arbitrary waveform generation to study the interfacial dilational rheology of adsorbed surfactant films.

3.2 Materials and Methods

3.2.1 Materials

Water used was Milli-Q water with resistivity greater than 18 MΩ·cm, filtrated by Millipore Corporation. (Millipore, Billerica, MA). C_{12}DMPO (MW=246.4 g/mol) used was from

Sigma-Aldrich Chemistry and used without further purification. A phosphate buffer solution of Na_2HPO_4 and NaH_2PO_4, from Sigma-Aldrich Chemistry, with ion strength of 0.03 (pH=7) and surface tension of 72.5mN/m, was used to dissolve the surfactant and proteins. On day of the experiment, a stock solution was prepared and diluted to desired concentrations. All measurements were at room temperature (20±1ºC).

3.2.2 Methods

The CDS is the experimental setup and the plant of the control system. The measurement in the control system is Axisymmetric Drop Shape Analysis, a computational technique written in C and C++. An image of the droplet is acquired by a machine vision camera (Model PLB-771U, PixeLink), and is fetched by an ADSA-based application. First, ADSA extracts the profile of the droplet through edge detection, to produce a 2D array of the edge pixel coordinates, known as the experimental profile. Second, a series of theoretical curves, with predefined physical properties, are generated through the Bashforth-Adams equation (Eq. 1.1), where axisymmetric interfaces can be expressed as a function of the arc length *s*:

$$\frac{d\theta}{ds} = \frac{2}{R_0} + \frac{\Delta\rho g}{\gamma} z - \frac{\sin\theta}{x} \quad \text{(Eq. 3.1)}$$

$$\frac{dx}{ds} = \cos\theta \quad \text{(Eq. 3.2)}$$

$$\frac{dz}{ds} = \sin\theta \quad \text{(Eq. 3.3)}$$

$$x(0) = 0, z(0) = 0, \theta(0) = 0 \quad \text{(Eq. 3.4)}$$

where θ is the tangential angle, *x* is the radius, and *z* is the height, R_0 is the curvature at the origin, and $\Delta\rho g / \gamma$ is the capillary constant of the system.[1] Third, a numerical fitting scheme fits and selects the theoretical drop profiles to the experimental profile, thereby outputting corresponding properties of the drop/bubble, including volume, surface area, and surface tension.

ADSA is capable of sampling up to a fast frequency of 10 Hz.[17] Recently, CDS based experiments was developed into a closed-loop control system where sampled droplet properties are fed back to control droplet/bubble toward a desired target.[17] A precise target volume, surface area, or surface tension can be reached through PID control:

$$u(t) = k_p * e(t) + \int_0^t k_i * e(\tau)\, d\tau + k_d \frac{de(t)}{dt} \quad \text{(Eq. 3.5)}$$

$$\mathrm{U(s)} = k_p * \mathrm{E(s)} + \left(\frac{k_i}{s}\right) * \mathrm{E(s)} + k_d * s * \mathrm{E(s)} \quad \text{(Eq. 3.6)}$$

$$\mathrm{U(z)} = k_p * \mathrm{E(z)} + \left(\frac{k_i}{1-\frac{1}{z}}\right) * \mathrm{E(z)} + k_d * (1 - \frac{1}{z}) * \mathrm{E(z)} \quad \text{(Eq. 3.7)}$$

Where k_p is the proportional gain, k_i is the integral gain, k_d is the derivative gain, e is the value of the error, and u is the value of the command signal, expressed as a function of t in the time domain, as a function of s in the Laplace domain, as a function of z in the Z domain. For most transients, the settling time is less than 5 seconds.[17]

3.3 Development of Waveform Generator.

Here, we extend the close-loop control to waveform generation. An arbitrary waveform is discretized to intervals up to 0.20s, bottlenecked by the motor's cycle between different movements. Through the discretize intervals, we control the volume or surface area to the arbitrary waveform. Prior to each interval, the error, *i.e.*, the difference between the current droplet value and the target value of the next interval, is calculated. Thereafter, the feedback control actuates the droplet through a motorized syringe. Parallel to PID control, to minimize oscillatory transients, a fuzzy control component is added. Moreover, through previous waveform periods, the PID gains and the fuzzy table can be fined tuned to minimize future error.

ADSA then feeds back and updated data for upcoming intervals and periods. A diagram of the flowchart of this waveform generation is illustrated in **Figure 1**.

There are a number of advantages and novelties of this waveform generation compared to previous drop/bubble oscillation methods:

1. This waveform generator is the first method capable of directly feedback controlling the volume and surface area of millimeter-sized droplets. In most oscillation methods, droplet surface area is approximated from its volume. However, given a sufficiently large Bond number, from droplet size and/or the presence of surfactants, the droplet deforms from a spherical bead profile, such that droplet surface area and volume are not linear with respect to each other.[17]

2. The waveforms demonstrated here are sine, triangle, square, and sawtooth waves. However, this waveform generator is not constrained to the waveforms shown here. Due to its principle of operation, this waveform generator can generate any arbitrarily defined waveform, similar to arbitrary waveform generators for electric signals.

3. Closed-loop ADSA is a free-standing method that can manipulate droplet in four different configurations. Although waveforms demonstrate here is through the sessile drop; pendant drop, pendant bubble, and sessile bubble are also applicable.

4. This waveform generator is independent of the physical method of fluid actuation, regardless driven through motorized syringes, piezoelectric transducers, or any other means. Faster fluid actuation methods are expected generate waveforms at even higher frequencies.

5. These waveforms can be generated at a frequency that coincides with the limiting frequency of other drop/bubble oscillation systems.[53] However, these waveform can be generated at significantly higher amplitudes.

3.4 Results and Discussion

3.4.1 Control of Droplet Volume and Surface Area

In this study, we demonstrate the generation of droplet volume and surface area waveforms of periodic functions of sine, triangle, square, and sawtooth. These four functions represent simple examples of periodic waveforms. a combination of these four or a part thereof can produce any arbitrary waveform. Volume and surface area are generated through the following equations:

$$\mathrm{Sine}(A_0,\ A,\ \omega,\ \varphi) = \mathrm{A}_0 + \mathrm{A} * \sin(\omega(t\ + \varphi)) \qquad \text{(Eq. 3.8)}$$

$$\mathrm{Triangle}(A_0,\ A,\ \omega,\ \varphi) = A_0 + 4\mathrm{A} * \omega((t + \varphi) - \frac{1}{2\omega}\left\lfloor 2\omega(t + \varphi\ ) + \frac{1}{2}\right\rfloor)(-1)^{\left\lfloor 2\omega(t+\varphi)+\frac{1}{2}\right\rfloor} \qquad \text{(Eq. 3.9)}$$

$$\mathrm{Square}(A_0,\ A,\ \omega,\ \varphi) = A_0 + \mathrm{A} * \mathrm{sgn}(\sin(\omega(t\ + \varphi)) \qquad \text{(Eq. 3.10)}$$

$$\mathrm{Sawtooth}(A_0,\ A,\ \omega,\ \varphi) = A_0 + \mathrm{A} * \omega((t + \varphi) - \frac{1}{\omega}\lfloor\omega(t + \varphi\ )\rfloor) \qquad \text{(Eq. 3.11)}$$

where A_0 is the offset, A is the amplitude, ω is the angular frequency, and φ is the phase shift. All four parameters of $A_0,\ A,\ \omega,$ and φ can be controlled. There are multiple equations to express some of these waveforms, and presented are general forms selected owning to lower computational costs. **Figure 3.2** shows the generation of periodic functions including, sine, triangle, square, and sawtooth of a water droplet on the CDS platform at room temperature.

In volume control, drops are controlled an offset of 15 μl, an amplitude of 20%, and a period of 20s. In surface area control, drops are controlled to an offset of 0.25cm2, an amplitude of 20%, and a period of 20s. **Figure 3.3** demonstrations surface tension control through sinusoidal waveform generation. **Figure 3.4** demonstrations of evaporation compensation through sinusoidal waveform generation. The ideal waveform is inserted as a red line. It is clear the volume and surface area follow the ideal waveforms very closely, except during the instantaneous jump of the square and sawtooth waves.

3.4.2 Evaluation of the Waveform Generation Accuracy and Limitations.

In this study, we demonstrate the accuracy of the waveform generation. **Figure 3.5.1** shows the coefficient of determination (R^2) analysis of periodic functions including, sine, triangle, square, and sawtooth of a water droplet on the CDS platform at room temperature. Three parameters of parameters of $A_0,\ A,$ and ω are controlled. Here, R^2 is calculated on a fixed $A_0,\ A,$ and ω through a Levenberg–Marquardt algorithm, such that this calculation encompasses both the relative error of $A_0,\ A,$ and ω and the closeness to the wave profile. Volume and surface area are controlled to an offset of 15 μl and 0.02 cm^2. Volume is controlled to an amplitude to 10% and 20%, 1.5 and 3 μl, respectively. Surface area is controlled to an amplitude to 10% and 20%, 0.02 and 0.04 cm^2, respectively. Volume and surface area are controlled to an oscillation frequency of 0.01Hz, 0.025Hz, 0.05Hz, 0.1Hz, 0.2Hz, and 0.5Hz.

The R^2 value is similar for both volume waves and surface area waves, and similar for both 10% and 20% amplitude variations. The R^2 value marginally deteriorates for triangle waveforms, due to the sharp peaks and crests with respect to a sine wave. The R^2 value deteriorates for square and sawtooth waveforms, due to the instantaneous jumps, and possible

ensuing oscillatory behaviors. The R^2 value deteriorates for waveforms frequencies above 0.1Hz. ADSA can sample at a frequency of ~10 Hz, and the limiting motor cycle is ~5 Hz, such that the motor cycle is assumed to be the bottleneck. For example, waveforms with a waveform with a frequency of 0.5Hz is allotted a maximum of 10 motor movements, incurring a sharper wave profile. Given a fluid actuation method with a faster turnaround time, this is expected to improve.

To quantify the limitations the waveform generation, a R^2 value of over 0.9 is defined and benchmarked as excellent waveform tracking. **Figure 3.5.2** illustrates this. It can be observed that the R^2 value is high and over 0.9 across the entire examined frequency spectrum for sine and triangle waveforms. For square and sawtooth waveforms, the R^2 value is over 0.9 for frequencies of 0.05Hz and 0.1Hz and below. From this, it can be concluded that frequencies below this benchmark can be administered acceptable tracking for various applications.[53]

3.4.3 Dilational Rheology Investigation

In this study, we engage the sinusoidal waveform generation to study dilational rheology. Dilational rheology is relevant in numerous technical and natural processes, including mass transfers, monolayers, foams, and emulsions.[54-55] In general, interface rheology studies mechanical modifications induced by elastic and viscous dilational and shear stress.[56] Dilational rheology can study the properties and composition of interfacial layers of proteins, lipids, polymers, particles, and surfactants.[54] The surface dilational rheology modulus, a complex number with a real part equal for surface elasticity and an imaginary part for surface viscosity, can be determined from surface area perturbations and resulting surface tension responses. A variety of methodologies have been developed for dilational rheology investigations, including oscillating barriers, [57-58], drop shape analysis.[59-61], capillary pressure,[62] and bubble pressure.[63-64]

A widely-used methodology for investigating dilational rheology is drop/bubble oscillation through surface tensiometry, where interfacial tension varies due to controlled surface area modifications. In modern drop/bubble profile tensiometry (DPT), surface area variation is possible through feedback control.[50] However, accurate droplet oscillation has many complications and limitations. Inaccurate surface area oscillation will lead to inaccurate surface tension oscillation, thereby resulting in inaccurate dilational rheology measurements. It is possible ensure greater accuracy in piezo-driven systems capable of nanometer step sizes,[65] however, this imposes inhibitions in the amplitude and frequency of the oscillation. In addition, the upper frequency limit may lead to artefacts in surface tension measurement.[53]

To demonstrate waveform generation in a dilational rheology study, a typical system of low molecular-weight surfactant is selected. The non-ionic surfactant dodecyldimethylphosphine oxide (C_{12}DMPO) was measured at different frequencies. The result was compared with experimental results in the literature. This application has demonstrated that the waveform generator is highly practical in studying the surface dilational rheology.

Surfactant can be considered as a thin film on a liquid surface such that the normal stress on any sectional area is the same. This is demonstrated in **Figure 3.6.** If we consider a small square region, there are normal stresses on each side of the square plate. This biaxial loading can be separated to the uniaxial loading along x and y directions. From stress along the *x* direction, the strain along *x* and *y* directions are defined as ε_x' and ε_y', and from stress along the *y* direction, the strain along *x* and *y* directions are defined as ε_x'' and ε_y'':

$$\varepsilon_x' = \frac{\sigma}{E},\ \varepsilon_y' = -\nu\frac{\sigma}{E} \qquad \text{(Eq. 3.12)}$$

$$\varepsilon_x'' = -\nu\frac{\sigma}{E},\ \varepsilon_y'' = \frac{\sigma}{E} \qquad \text{(Eq. 3.13)}$$

thus, from a biaxial perspective, the strain can be given as:

$$\varepsilon_x = \varepsilon_x' + \varepsilon_x'' = \frac{1-\nu}{E}\sigma,\ \varepsilon_y = \varepsilon_y' + \varepsilon_y'' = \frac{1-\nu}{E}\sigma \ \rightarrow\ \varepsilon_x = \varepsilon_y = \frac{1-\nu}{E}\sigma \qquad \text{(Eq. 3.14)}$$

where ε_x' and ε_y' are strains along the x direction, ε_x'' and ε_y'' are strains along the y direction, ε_x and ε_y are strains from a biaxial perspective, σ is the stress, E is the modulus, and ν is the Poisson's ratio.

The surface dilational modulus, a complex quantity with a real part expressing surface elasticity and an imaginary part expressing surface viscosity, can be determined from harmonic surface area perturbations and resulting surface tension responses.[48] For elastic behavior, the surface stress is proportional to the relative surface area perturbation. For viscous behavior, the surface stress is proportional to the rate of surface area perturbation.[66] A general expression for the surface dilational modulus is:

$$E = \frac{\Delta\gamma}{A/A_0} = E_0 + i2\pi\omega\eta = E_r + iE_i \qquad \text{(Eq. 3.15)}$$

where E is the dilational viscoelasticity modulus, $\Delta\gamma$ is amplitude of surface tension variations, A_0 is the reference surface area, A is the amplitude of the surface area oscillation, ω is the angular frequency of the harmonic surface area oscillations, E_0 is the dilational elasticity, η is the dilational viscosity, $E_0 = E_r$ is the real part of the dilational modulus, and $2\pi\nu\eta = E_i$ is the imaginary part of the dilational modulus.

When investigating the dynamics of interfacial layers, the dilational modulus is significant given its relation to the frequency of surface area perturbations.[54] Usually, in

experiments involving harmonic surface area perturbations, a frequency sweep of surface area occurs in the following form:

$$A = A_0 + \tilde{A}\sin(2\pi\omega t) \quad \text{(Eq. 3.16)}$$

where A is surface area, A_0 is the reference surface area, $\tilde{A}$ is the amplitude of surface area oscillations, and ω is the frequency. The harmonic response of surface tension γ is:

$$\gamma = \gamma_0 + \tilde{\gamma}\sin(2\pi\omega t + \varphi) \quad \text{(Eq. 3.17)}$$

where γ is the surface tension, γ_0 is the equilibrium reference surface tension, $\tilde{\gamma}$ is amplitude of surface tension variations, and φ is the phase shift between the surface area perturbations and surface tension response. Here, A_0, $\widetilde{A}$, and ω are controlled through the waveform generator, γ_0, $\tilde{\gamma}$ and φ are extracted through a Levenberg–Marquardt curve fit of the measured surface tension. The phase shift φ is the phase of the complex dilational modulus, and the elastic and viscous moduli can be determined experimentally:

$$|E| = A_0 \frac{\tilde{\gamma}}{\tilde{A}} \quad \text{(Eq. 3.18)}$$

$$|E_r| = A_0 \frac{\tilde{\gamma}}{\tilde{A}}\cos(\varphi) \quad \text{(Eq. 3.19)}$$

$$|E_i| = A_0 \frac{\tilde{\gamma}}{\tilde{A}}\sin(\varphi) \quad \text{(Eq. 3.20)}$$

To demonstrate dilational rheology measurement, the widely studied non-ionic surfactant dodecyldimethylphosphine oxide (C_{12}DMPO) is studied. A surface area frequency sweep is applied to measure the dilational rheology modulus of C_{12}DMPO at different frequencies. The result was compared with experimental results in literature. **Figure 3.7** demonstrates the

dilational rheology modulus measurement of C_{12}DMPO (c=0.22 mM) on the CDS platform at room temperature. (a) In this control, the droplet is controlled to an offset of 0.2cm^2 and an amplitude of 10%. The ideal waveform is inserted as a red line. It is clear the surface area follows the ideal waveform closely. The blue line is the Levenberg–Marquardt curve fit of the surface tension measurement. The amplitude and phase lead of the surface tension response is 1.9 mN/m and 20^o, respectively. (b) Real and imaginary parts of surface dilational modulus of C_{12}DMPO (c=0.22 mM), measured at frequencies of 0.01Hz, 0.025Hz, 0.05Hz, 0.1Hz, 0.2Hz, and 0.5Hz. Literature surface dilational modulus values at frequencies of 0.01Hz, 0.02Hz, 0.04Hz, 0.08Hz, 0.16Hz, 0.32Hz, and 0.5Hz are included in this figure.[6363] This study has demonstrated the waveform generator is highly applicable in studying surface dilational rheology.

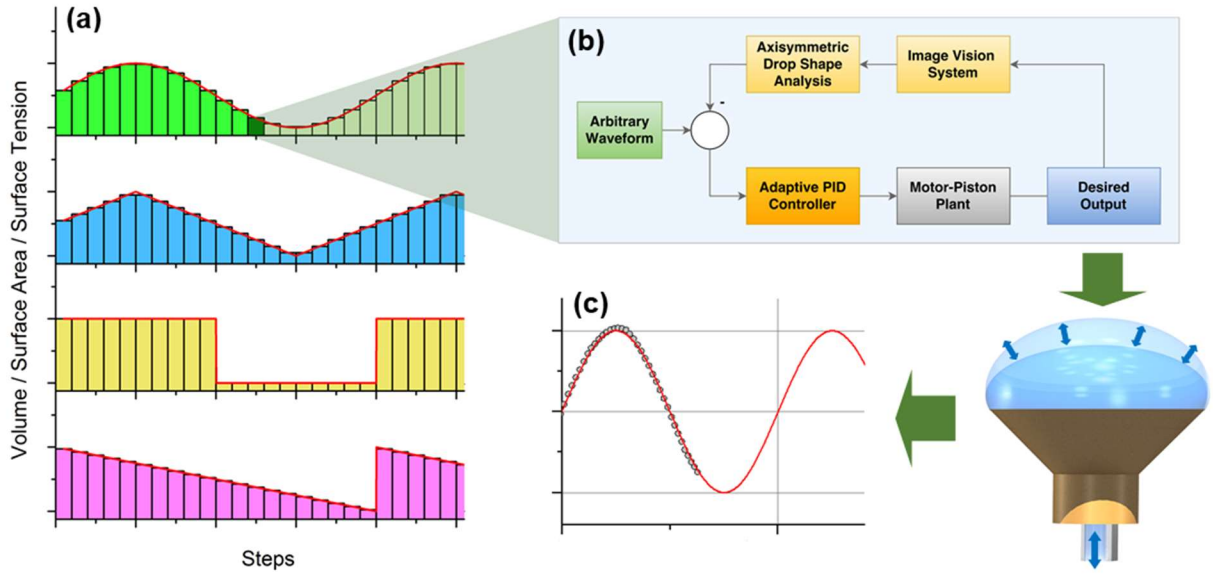

Figure 3.1. Schematic arbitrary waveform generation for droplet volume and surface area. (a) Four waveforms demonstrated are sine, triangle, square and sawtooth waves. To achieve tracking, the waveforms discretized to a series of intervals, each a control loop to actuate the droplet. (b) Schematic for the control loop of every interval. Through a modified proportional-integral-derivative (PID) control and servomotor piston-syringe plant, the droplet is controlled to the target of the interval, collectively generating waveforms. (c) The resulting image is fetched by an image processing algorithm and Axisymmetric drop shape analysis (ADSA) to produce experimental results.

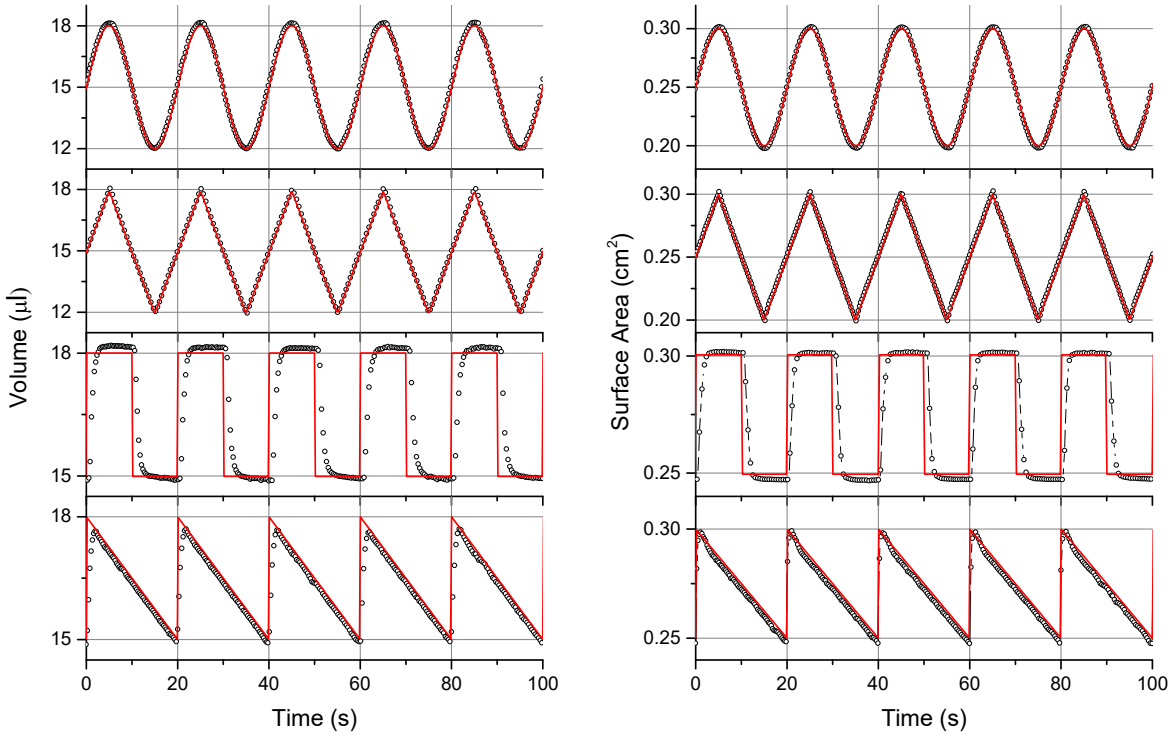

Figure 3.2. Demonstration of waveform generation for droplet volume and surface area of pure water on the CDS platform at room temperature. Four waveforms demonstrated are sine, triangle, square, and sawtooth waves. In volume control, drops are controlled an offset of 15µl, an amplitude of 20%, and a period of 20s. In surface area control, drops are controlled to an offset of 0.25cm^2, an amplitude of 20%, and a period of 20s. The ideal function is inserted as a red line. It is clear volume and surface area follows the ideal waveform closely.

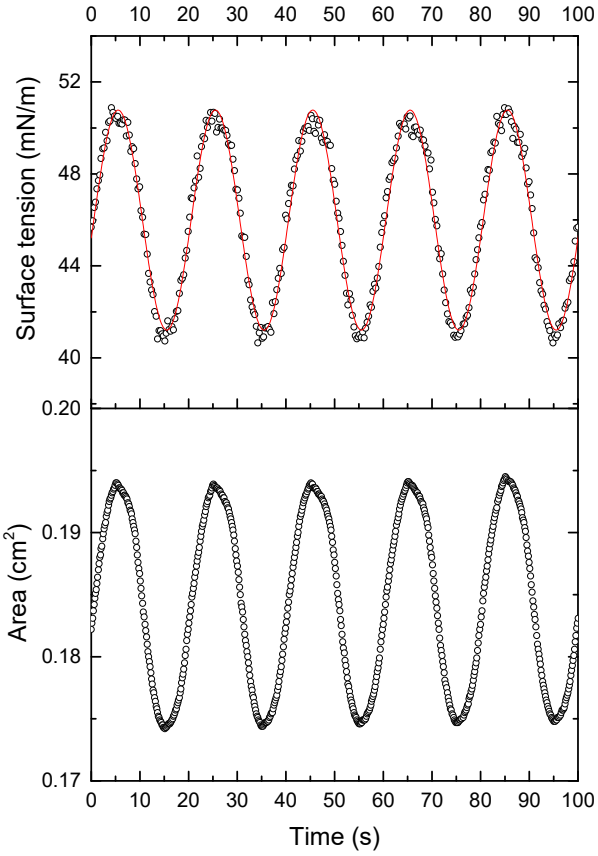

Figure 3.3. Demonstration of sinusoidal waveform generation of surface tension of DOPC on the CDS platform at room temperature. Drops are controlled an offset of 46 mN/m, an amplitude of 5 mN/m, and a period of 20s. The ideal function is inserted as a red line. While there is noise surface tension sampling, it is clear volume and surface tension wave follows the ideal waveform closely.

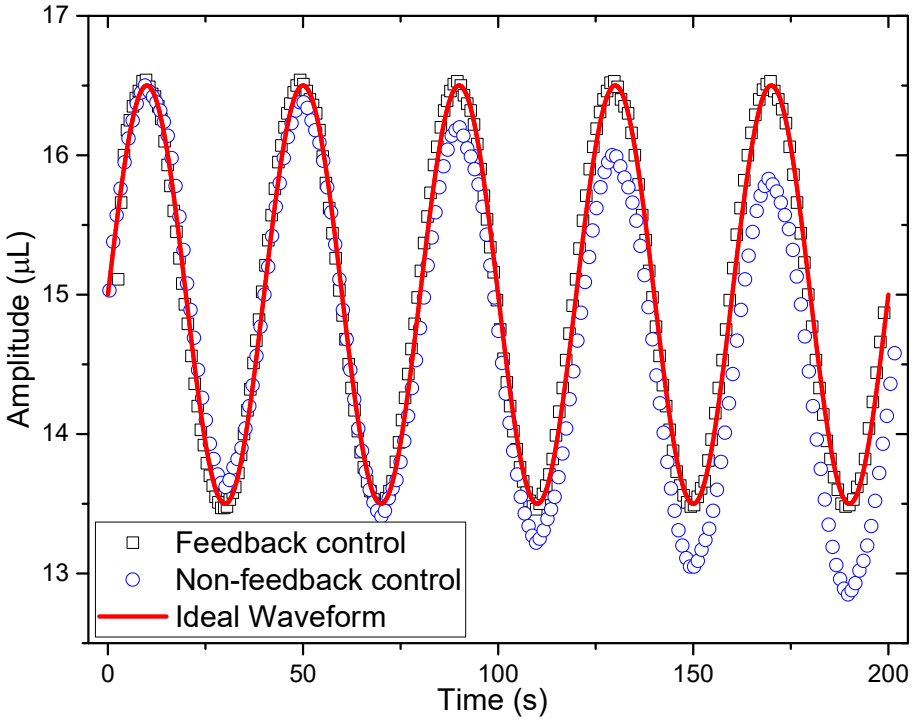

Figure 3.4. Demonstration of sinusoidal waveform generation volume by automatically compensating evaporation. Two waveforms of feedback waveform generation and non-feedback waveform generation are controlled an offset of 15µl, an amplitude of 10%, and a period of 40s. The ideal function is inserted as a red line. Without feedback control, droplet volume shrinks significantly over 200 seconds due to natural evaporation. With feedback control, droplet volume was controlled in the same time period, following the ideal waveform closely.

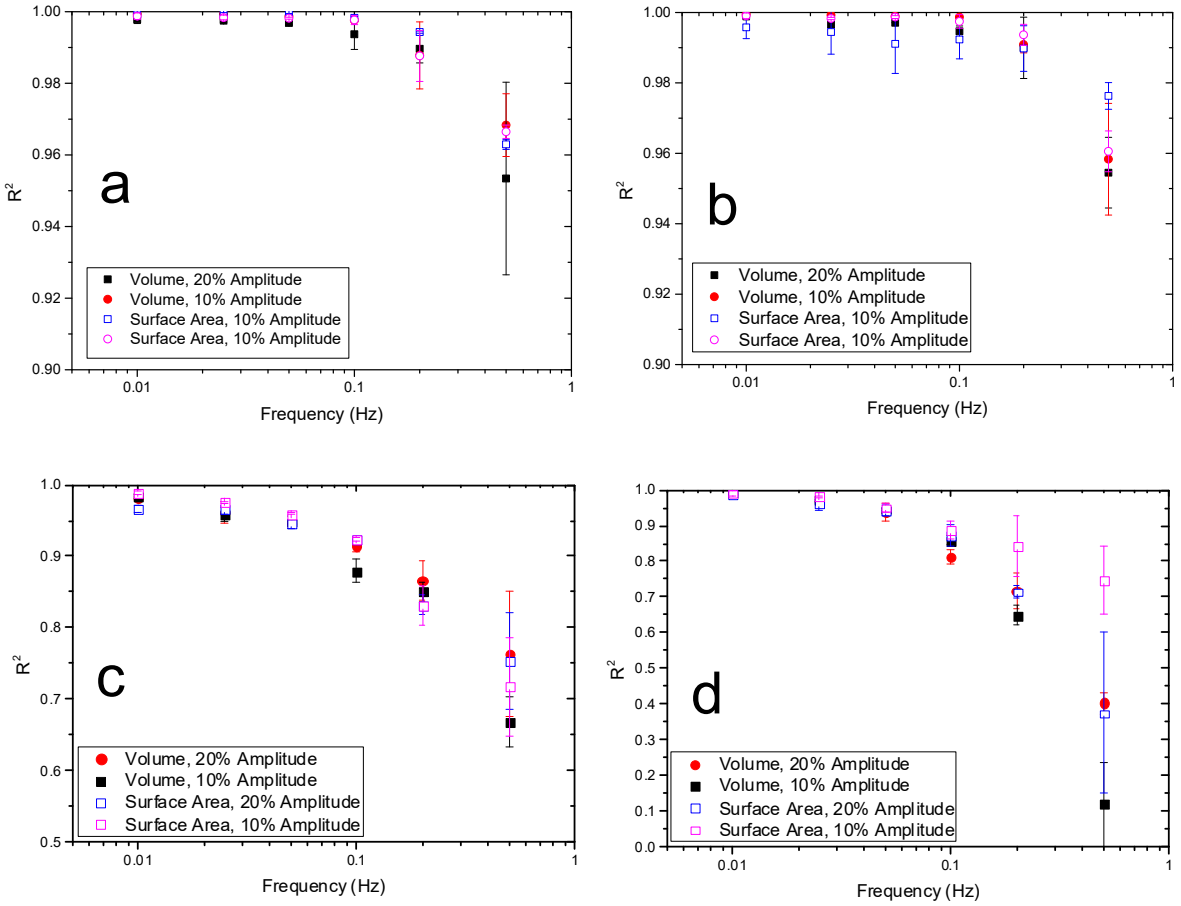

Figure 3.5.1 Accuracy evaluation of waveforms using the coefficient of determination or R^2 for (a) sine, (b) triangle, (c) square, and (d) sawtooth waveforms, for volume and surface area at two amplitudes (10% and 20%). Six frequencies are evaluated, 0.01Hz, 0.025Hz, 0.05Hz, 0.1Hz, 0.2Hz, and 0.5Hz. Four observations can be made. 1. The coefficient of determination is similar for both volume waves and surface area waves. 2. The coefficient of determination is similar for both volume control and area control for both 10% and 20% amplitude variations. 3. The coefficient of determination deteriorates at high frequencies of 0.2hz, and 0.5hz. 4. The coefficient of determination deteriorates for square and sawtooth waveforms.

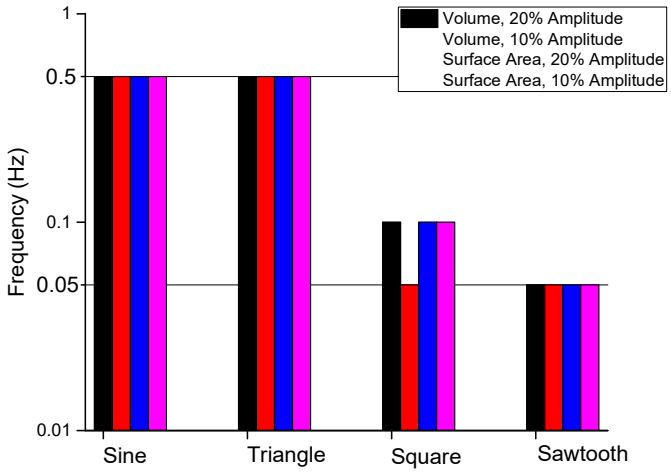

Figure 3.5.2 Evaluation of waveform generation based on the coefficient of determination. The coefficient of determination threshold of the waveforms is defined 0.9, beyond which, the experimental waveform is evaluated to track the ideal waveform with a high degree of accuracy. For higher frequencies above 0.2hz and 0.5hz, the accuracy decreases due to sampling limitations and motor limitations. For square and sawtooth waveforms, accuracy decreases due to the transience of the instantaneous jump. The accuracy decreases when frequency increases from 0.5 Hz or 0.1 Hz.

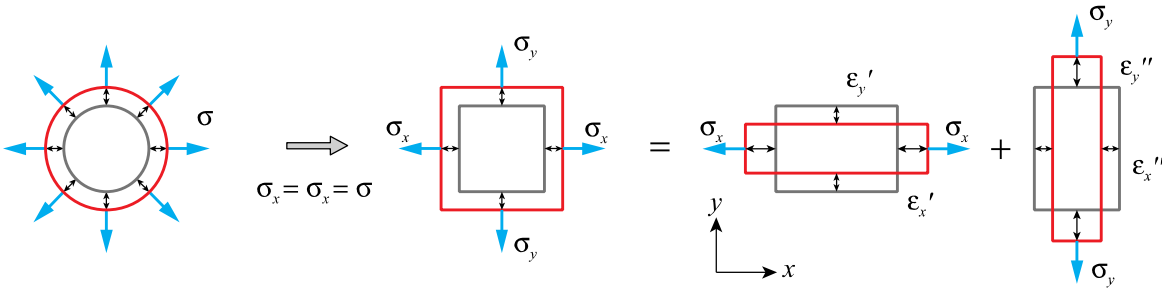

Figure 3.6 Diagram of biaxial loading and uniaxial loading. On the left, a surfactant film experiences normal stress on all directions. If we consider a small square region, there are normal stresses on each side of the square plate. This biaxial loading can be separated to the uniaxial loading along x and y directions. From stress along the *x* direction, the strain along *x* and *y* directions are defined as ε_x' and ε_y', and from stress along the *y* direction, the strain along *x* and *y* directions are defined as ε_x'' and ε_y'':

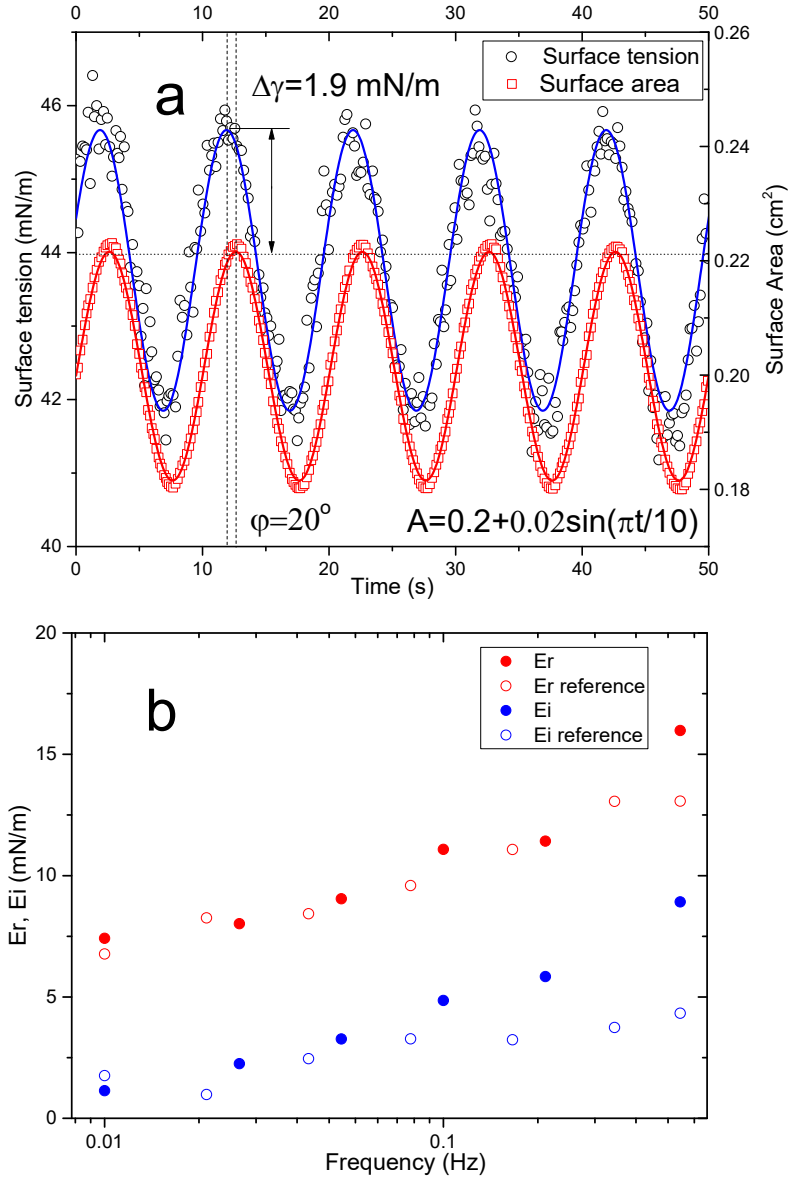

Figure 3.7 Demonstration of sinusoidal waveform generation of surface area of C12DMPO (c=0.22 mM) on the CDS platform at room temperature. (a) In this control, drops are controlled to an offset of 0.2cm^2, an amplitude of 10%, and a period of 10s. The ideal function is inserted as a red line. It is clear volume and surface area follows the ideal waveform closely. The dashed blue line is the best sinusoidal fitting of the surface tension, and the phase lead of surface tension is 20^o. The amplitude of the surface tension response is 1.9 mN/m. (b) Real and imaginary parts of surface dilational modulus of C_{12}DMPO (c=0.22 mM), calculated for frequencies of 0.01Hz, 0.025Hz, 0.05Hz, 0.1Hz, 0.2Hz, and 0.5Hz. Literature surface dilational modulus values at frequencies of 0.01Hz, 0.02Hz, 0.04Hz, 0.08Hz, 0.16Hz, 0.32Hz, and 0.5Hz are included in the figure.

Chapter 4. Conclusions and Recommendations

4.1 Summary of Contributions

1. I developed a unified droplet/bubble coordinate system, through C and C++. Combined with ADSA and the experimental setup CDS, we measure both surface and interfacial tensions for four configurations, *i.e.*, sessile drop, pendant drop, sessile bubble, and pendant bubble. The measurements of surface and interfacial tensions for a number of surface and interfaces demonstrated the accuracy and feasibility of the ADSA and the CDS.

2. I developed a feedback control system with ADSA, through C and C++. I interfaced the feedback control system with the CDS to manipulate droplets. Closed-loop ADSA extends the applications of the CDS from a surface tension measurement methodology to a sophisticated tool for automatically manipulating droplets in real-time. We have demonstrated the feasibility and advantages of closed-loop ADSA in three applications, including control of drop volume by automatically compensating natural evaporation, precise control of surface area variations for high-fidelity biophysical simulations of natural pulmonary surfactant, and steady control of surface pressure for *in situ* Langmuir-Blodgett transfer from droplets. The closed-loop ADSA holds great promise for advancing droplet manipulation in a variety of material and surface science applications, such as thin-film fabrication, self-assembly, and biophysical study of pulmonary surfactant.

3. I developed an arbitrary waveform generator for droplets and bubbles, through C and C++. To demonstrate this droplet manipulation method, we engaged in demonstration, evaluation, and application. First, we demonstrate arbitrary waveform generation through manipulating a pure water droplet's volume and surface area to sine, triangle, square, and

sawtooth waveforms. The amplitude and period of the waveform is precisely controlled. Second, we evaluate arbitrary waveform generation through a coefficient of determination (R^2) analysis. Third, we apply arbitrary waveform generation to dilational rheology measurement for layers of surfactants. The strengths, applicability, and limitations of our method will also be discussed.

4.2 Recommendations

4.2.1 Parallel Computing ADSA

Through the advances of multi-core processors. parallel computing has become the paradigm in computer architecture. Parallel computing allows for many calculations to executions simultaneously. Distributing the computation of ADSA can potentially increase its sampling speed by an order of magnitude. Parallel loops, parallel tasks, and parallel aggregation can be sequentially implemented. Parallelization issues including but not limited to deadlocking will need to be minimized. OpenMP API and the Microsoft developer network may be good places to start.

4.2.2 Image Processing Techniques

Image processing is applying algorithms on images for processing. A wide range of operations can be applied to the image. Superior image processing techniques will improve the sampling time of ADSA without the loss of quality, this includes but is not limited to fast canny analysis and SUSAN edge detection.

4.2.3 Machine Learning Feedback Control

Adaptive control is a control method where a controller adapts to a controlled system. Adaptive control does not operate upon previous information regarding the time-varying parameters. Given the error of the waveform changes with different control parameters, a machine learning control algorithm can be implemented to minimize error in future cycles or periods.

Vita

Kyle Yu received his Bachelors of Applied Science in Mechatronics Engineering from the University of Waterloo, Waterloo, Ontario, Canada, in 2016. He worked as a control system engineer for the Department of Mechanical Engineering in the University of Hawaii at Manoa, in 2013 and 2015. He is a candidate for a Master of Science in Mechanical Engineering degree from the University of Hawaii at Manoa, in 2017. The title of his thesis is "Feedback Control in Droplet Manipulation".

Papers of refereed journals for publication:

1. Yang, J., **Yu, K.,** and Zuo, Y. Y. (2017). Accuracy of axisymmetric drop shape analysis in determining surface and interfacial tensions. *Langmuir*, *33*(36), 8914-8923.

3. **Yu, K.*,** Yang, J.*, and Zuo, Y. Y. (2016). Automated droplet manipulation using closed-loop axisymmetric drop shape analysis. *Langmuir*, *32*(19), 4820-4826. (*co-first authors)

Papers in preparation:

1. **Yu, K.,** Yang, J., and Zuo, Y. Y., Arbitrary waveform generation through oscillating droplet. To be submitted to *Applied Physics Letters*.

2. Yang, J., **Yu, K.,** Tsuji, T., Jha, R., and Zuo, Y. Y., Surface dilational rheology measured by a droplet waveform generator. To be submitted to *ACS Applied Materials and Interfaces*.

3. Xu, L., Bosiljevac G, **Yu K.,** and Zuo, Y. Y., Melting of Dipalmitoylphosphatidylcholine Monolayers. To be submitted to *Langmuir.*

References

1. del Rıo, O.; Neumann, A. W., Axisymmetric drop shape analysis: computational methods for the measurement of interfacial properties from the shape and dimensions of pendant and sessile drops. *Journal of colloid and interface science* **1997,** *196* (2), 136-147.

2. Valle, R. P.; Wu, T.; Zuo, Y. Y., Biophysical Influence of Airborne Carbon Nanomaterials on Natural Pulmonary Surfactant. *ACS Nano* **2015,** *9* (5), 5413-5421.

3. Roberts, G., *Langmuir-Blodgett Films*. Springer: 1990.

4. Rotenberg, Y.; Boruvka, L.; Neumann, A., Determination of surface tension and contact angle from the shapes of axisymmetric fluid interfaces. *Journal of colloid and interface science* **1983,** *93* (1), 169-183.

5. Saad, S. M.; Neumann, A. W., Axisymmetric Drop Shape Analysis (ADSA): An Outline. *Adv Colloid Interface Sci* **2016,** *238*, 62-87.

6. He, Q.; Zhang, Y.; Lu, G.; Miller, R.; Mohwald, H.; Li, J., Dynamic adsorption and characterization of phospholipid and mixed phospholipid/protein layers at liquid/liquid interfaces. *Adv Colloid Interface Sci* **2008,** *140* (2), 67-76.

7. Cabrerizo-Vilchez, M. A.; Wege, H. A.; Holgado-Terriza, J. A.; Neumann, A. W., Axisymmetric drop shape analysis as penetration Langmuir balance. *Review of Scientific Instruments* **1999,** *70* (5), 2438-2444.

8. Russev, S. C.; Alexandrov, N.; Marinova, K. G.; Danov, K. D.; Denkov, N. D.; Lyutov, L.; Vulchev, V.; Bilke-Krause, C., Instrument and methods for surface dilatational rheology measurements. *The Review of scientific instruments* **2008,** *79* (10), 104102.

9. Teh, S.-Y.; Lin, R.; Hung, L.-H.; Lee, A. P., Droplet microfluidics. *Lab on a Chip* **2008,** *8* (2), 198-220.

10. Neumann, A. W.; David, R.; Zuo, Y., *Applied surface thermodynamics*. CRC press: 2010; Vol. 151.

11. Valle, R. P.; Wu, T.; Zuo, Y. Y., Biophysical influence of airborne carbon nanomaterials on natural pulmonary surfactant. *ACS Nano* **2015,** *9* (5), 5413-21.

12. Baratian, D.; Cavalli, A.; van den Ende, D.; Mugele, F., On the shape of a droplet in a wedge: new insight from electrowetting. *Soft matter* **2015,** *11* (39), 7717-7721.

13. Gong, J.; Kim, C.-J., All-electronic droplet generation on-chip with real-time feedback control for EWOD digital microfluidics. *Lab on a Chip* **2008,** *8* (6), 898-906.

14. Miller, E.; Rotea, M.; Rothstein, J. P., Microfluidic device incorporating closed loop feedback control for uniform and tunable production of micro-droplets. *Lab on a Chip* **2010,** *10* (10), 1293-1301.

15. Wege, H. A.; Holgado-Terriza, J. A.; Cabrerizo-Vilchez, M. A., Development of a constant surface pressure penetration langmuir balance based on axisymmetric drop shape analysis. *J Colloid Interface Sci* **2002,** *249* (2), 263-73.

16. Horch, A. e. a., Assessment of the sampling rate in control systems. *Control Engineering Practice* **2001,** *Volume 9* (Issue 5).

17. Yu, K.; Yang, J.; Zuo, Y. Y., Automated droplet manipulation using closed-loop axisymmetric drop shape analysis. *Langmuir* **2016,** *32* (19), 4820-4826.

18. Zhang, H.; Fan, Q.; Wang, Y. E.; Neal, C. R.; Zuo, Y. Y., Comparative study of clinical pulmonary surfactants using atomic force microscopy. *Biochim Biophys Acta* **2011,** *1808*, 1832-1842.

19. Zhang, H.; Wang, Y. E.; Fan, Q.; Zuo, Y. Y., On the low surface tension of lung surfactant. *Langmuir* **2011,** *27* (13), 8351-8358.

20. Valle, R. P.; Huang, C. L.; Loo, J. S. C.; Zuo, Y. Y., Increasing Hydrophobicity of Nanoparticles Intensifies Lung Surfactant Film Inhibition and Particle Retention. *ACS Sustainable Chemistry & Engineering* **2014,** *2* (7), 1574-1580.

21. Dagan, M. P.; Hall, S. B., The Equilibrium Spreading Tension of Pulmonary Surfactant. *Langmuir* **2015,** *31* (48), 13063-7.

22. Jasper, J. J., The surface tension of pure liquid compounds. *J. Phys. Chem. Ref. Data* **1972,** *1* (4), 841-1009.

23. Phillips, C. L.; Nagle, H. T.; Chakrabortty, A., *Digital control system analysis & design, global edition*. Pearson Education: 2014.

24. Saad, S. M.; Neumann, A. W., Total Gaussian curvature, drop shapes and the range of applicability of drop shape techniques. *Adv Colloid Interface Sci* **2014,** *204*, 1-14.

25. Berry, J. D.; Neeson, M. J.; Dagastine, R. R.; Chan, D. Y. C.; Tabor, R. F., Measurement of surface and interfacial tension using pendant drop tensiometry. *Journal of Colloid and Interface Science* **2015,** *454*, 226-237.

26. Miller, R.; Fainerman, V. B.; Makievski, A. V.; Kragel, J.; Grigoriev, D. O.; Kazakov, V. N.; Sinyachenko, O. V., Dynamics of protein and mixed protein/surfactant adsorption layers at the water/fluid interface. *Adv Colloid Interface Sci* **2000,** *86* (1-2), 39-82.

27. Mitropoulos, V.; Mütze, A.; Fischer, P., Mechanical properties of protein adsorption layers at the air/water and oil/water interface: A comparison in light of the thermodynamical stability of proteins. *Advances in Colloid and Interface Science* **2014,** *206*, 195-206.

28. Tankovsky, N.; Zografov, N.; Andreeva, A., Gas-adsorption dynamics at the water–air interface, revealed by resonant droplet tensiometry. *Chemical Engineering Science* **2016,** *144*, 283-287.

29. Bonaccurso, E.; Butt, H. J., Microdrops on atomic force microscope cantilevers: evaporation of water and spring constant calibration. *The journal of physical chemistry. B* **2005,** *109* (1), 253-63.

30. Birdi, K. S.; Vu, D. T.; Winter, A., A study of the evaporation rates of small water drops placed on a solid surface. *The Journal of Physical Chemistry* **1989,** *93* (9), 3702-3703.

31. Shanahan, M. E. R. B., C., Effects of evaporation on contact angles on polymer surfaces. *International Journal of Adhesion and Adhesives* **1994,** *14* (3), 201-205.

32. Hu, H.; Larson, R. G., Evaporation of a Sessile Droplet on a Substrate. *The Journal of Physical Chemistry B* **2002,** *106* (6), 1334-1344.

33. Bachofen, H.; Schurch, S.; Urbinelli, M.; Weibel, E. R., Relations among alveolar surface tension, surface area, volume, and recoil pressure. *J. Appl. Physiol.* **1987,** *62* (5), 1878-1887.

34. Bachofen, H.; Schürch, S., Alveolar surface forces and lung architecture. *Comparative Biochemistry and Physiology - A Molecular and Integrative Physiology* **2001,** *129* (1), 183-193.

35. Kharge, A. B.; Wu, Y.; Perlman, C. E., Surface tension in situ in flooded alveolus unaltered by albumin. *Journal of applied physiology* **2014,** *117* (5), 440-451.

36. Piknova, B.; Schram, V.; Hall, S. B., Pulmonary surfactant: phase behavior and function. *Current opinion in structural biology* **2002,** *12* (4), 487-94.

37. Possmayer, F.; Hall, S. B.; Haller, T.; Petersen, N. O.; Zuo, Y. Y.; Bernardino de la Serna, J.; Postle, A. D.; Veldhuizen, R. A. W.; Orgeig, S., Recent advances in alveolar biology: Some new looks at the alveolar interface. *Respiratory Physiology & Neurobiology* **2010,** *173* (Supplement 1), S55-S64.

38. Rugonyi, S.; Biswas, S. C.; Hall, S. B., The biophysical function of pulmonary surfactant. *Respir Physiol Neurobiol* **2008,** *163* (1-3), 244-55.

39. Zuo, Y. Y.; Veldhuizen, R. A.; Neumann, A. W.; Petersen, N. O.; Possmayer, F., Current perspectives in pulmonary surfactant--inhibition, enhancement and evaluation. *Biochim Biophys Acta* **2008,** *1778* (10), 1947-77.

40. Yan, W.; Biswas, S. C.; Laderas, T. G.; Hall, S. B., The melting of pulmonary surfactant monolayers. *J Appl Physiol* **2007,** *102* (5), 1739-45.

41. Saad, S. M.; Policova, Z.; Acosta, E. J.; Hair, M. L.; Neumann, A. W., Mixed DPPC/DPPG monolayers at very high film compression. *Langmuir* **2009,** *25* (18), 10907-12.

42. Kaganer, V. M.; Mohwald, H.; Dutta, P., Structure and phase transitions in Langmuir monolayers. *Rev Mod Phys* **1999,** *71* (3), 779-819.

43. Keating, E.; Zuo, Y. Y.; Tadayyon, S. M.; Petersen, N. O.; Possmayer, F.; Veldhuizen, R. A., A modified squeeze-out mechanism for generating high surface pressures with pulmonary surfactant. *Biochim Biophys Acta* **2012,** *1818* (5), 1225-34.

44. McConlogue, C. W.; Vanderlick, T. K., A close look at domain formation in DPPC monolayers. *Langmuir* **1997,** *13* (26), 7158-7164.

45. Haydon, D. A., An investigation of droplet oscillation during mass transfer I. The conditions necessary, and the source of the energy for the oscillations. *Proceedings of the Royal Society of London. Series A. Mathematical and Physical Sciences* **1958,** *243* (1235), 483-491.

46. Mugele, F.; Baret, J.-C.; Steinhauser, D., Microfluidic mixing through electrowetting-induced droplet oscillations. *Applied Physics Letters* **2006,** *88* (20), 204106.

47. Yu, L. M.; Lu, J. J.; Chan, Y. W.; Ng, A.; Zhang, L.; Hoorfar, M.; Policova, Z.; Grundke, K.; Neumann, A. W., Constrained sessile drop as a new configuration to measure low surface tension in lung surfactant systems. *Journal of applied physiology* **2004,** *97* (2), 704-15.

48. Miller, R.; Liggieri, L., *Interfacial rheology*. CRC Press: 2009; Vol. 1.

49. Neumann, A. W.; David, R.; Zuo, Y., *Applied Surface Thermodynamics, Second Edition*. Taylor & Francis: 2012; Vol. surfactant science series.

50. Ravera, F.; Loglio, G.; Kovalchuk, V. I., Interfacial dilational rheology by oscillating bubble/drop methods. *Current Opinion in Colloid & Interface Science* **2010,** *15* (4), 217-228.

51. Egry, I., Surface tension measurements of liquid metals by the oscillating drop technique. *Journal of Materials Science* **1991,** *26* (11), 2997-3003.

52. Milne, A. J. B.; Defez, B.; Cabrerizo-Vílchez, M.; Amirfazli, A., Understanding (sessile/constrained) bubble and drop oscillations. *Advances in Colloid and Interface Science* **2014,** *203* (Supplement C), 22-36.

53. Leser, M. E.; Acquistapace, S.; Cagna, A.; Makievski, A. V.; Miller, R., Limits of oscillation frequencies in drop and bubble shape tensiometry. *Colloids and Surfaces A: Physicochemical and Engineering Aspects* **2005,** *261* (1-3), 25-28.

54. Dukhin, S. K., G.; Miller, R., *Dynamics of adsorption at liquid interfaces*. Elsevier: 1995; Vol. 1.

55. Berg, J. C., *An Introduction to Interfaces and Colloids: The Bridge to Nanoscience*. World Scientific: Singapore, 2010.

56. Miller, R.; Ferri, J. K.; Javadi, A.; Krägel, J.; Mucic, N.; Wüstneck, R., Rheology of interfacial layers. *Colloid and Polymer Science* **2010,** *288* (9), 937-950.

57. Lucassen, J.; Van Den Tempel, M., Dynamic measurements of dilational properties of a liquid interface. *Chemical Engineering Science* **1972,** *27* (6), 1283-1291.

58. Benjamins, J.; Lucassen-Reynders, E., Surface dilational rheology of proteins adsorbed at air/water and oil/water interfaces. *Studies in Interface Science* **1998,** *7*, 341-384.

59. Loglio, G.; Pandolfini, P.; Miller, R.; Makievski, A.; Ravera, F.; Ferrari, M.; Liggieri, L., Drop and Bubble Shape Analysis As a Tool for Dilational Rheological Studies of Interfacial Layers. *Studies in Interface Science; Möbius, D.; Miller, R., Eds*, 439-483.

60. Stubenrauch, C.; Miller, R., Stability of foam films and surface rheology: an oscillating bubble study at low frequencies. *The Journal of Physical Chemistry B* **2004,** *108* (20), 6412-6421.

61. Kotsmar, C.; Kragel, J.; Kovalchuk, V. I.; Aksenenko, E. V.; Fainerman, V. B.; Miller, R., Dilation and shear rheology of mixed β-casein/surfactant adsorption layers. *The Journal of Physical Chemistry B* **2008,** *113* (1), 103-113.

62. Noskov, B. A.; Akentiev, A. V.; Bilibin, A. Y.; Zorin, I. M.; Miller, R., Dilational surface viscoelasticity of polymer solutions. *Advances in Colloid and Interface Science* **2003,** *104* (1), 245-271.

63. Kovalchuk, V. I.; Krägel, J.; Makievski, A. V.; Ravera, F.; Liggieri, L.; Loglio, G.; Fainerman, V. B.; Miller, R., Rheological surface properties of C12DMPO solution as obtained from amplitude- and phase-frequency characteristics of an oscillating bubble system. *Journal of Colloid and Interface Science* **2004,** *280* (2), 498-505.

64. Wantke, K.-D.; Fruhner, H., Determination of surface dilational viscosity using the oscillating bubble method. *Journal of colloid and interface science* **2001,** *237* (2), 185-199.

65. Russev, S. C.; Alexandrov, N.; Marinova, K. G.; Danov, K. D.; Denkov, N. D.; Lyutov, L.; Vulchev, V.; Bilke-Krause, C., Instrument and methods for surface dilatational rheology measurements. *Review of scientific instruments* **2008,** *79* (10), 104102.

66. Ivanov, I. B.; Danov, K. D.; Ananthapadmanabhan, K. P.; Lips, A., Interfacial rheology of adsorbed layers with surface reaction: on the origin of the dilatational surface viscosity. *Advances in colloid and interface science* **2005,** *114*, 61-92.